Bismuth-Based Halide Perovskite and Perovskite-Inspired Light Absorbing Materials for Photovoltaics

Feray Ünlü[1], Meenal Deo[2], Sanjay Mathur[1] *, Thomas Kirchartz[3, 4] *, Ashish Kulkarni[3] *

[1]Institute of Inorganic Chemistry, University of Cologne, Greinstr. 6, 50939 Cologne, Germany.

[2]Department of Physics and Nanotechnology, SRM Institute of Science and Technology, Kattankulathur 603203, Chennai, India.

[3]IEK5-Photovoltaics Forschungszentrum Jülich, 52425 Jülich, Germany.

[4]Faculty of Engineering and CENIDE, University of Duisburg-Essen, Carl-Benz-Str. 199, 47057 Duisburg, Germany.

Emails:

Dr. Ashish Kulkarni – a.kulkarni@fz-juelich.de

Prof. Dr. Thomas Kirchartz – t.kirchartz@fz-juelich.de

Prof. Dr. Sanjay Mathur – sanjay.mathur@uni-koeln.de

ABSTRACT

The efficiency of organic-inorganic hybrid lead halide perovskite solar cells (PSCs) has increased over 25% within a frame of ten years, which is phenomenal and indicative of the promising potential of perovskite materials in impacting the next generation solar cells. Despite high technology readiness of perovskite solar cells, the presence of lead has raised concerns about the adverse effect of lead on human health and the environment that may slow down or inhibit the commercialization of perovskite solar cells. Thus, there is a dire need to identify materials with lower toxicity profile and comparable optoelectronic properties in regard to lead-halide perovskites. In comparison to tin-, germanium-, and copper-based PSCs, which suffer from stability issues under ambient operation, bismuth-based perovskite and perovskite-inspired materials have gained attention because of their enhanced stability in ambient atmospheric conditions. In this topical review, we initially discuss the background of lead and various lead-free perovskite materials and further discuss the fundamental aspects of various bismuth-based perovskite and perovskite-inspired materials having a chemical formula of $A_3\mathbf{Bi}_2X_9$, $A_2B'\mathbf{Bi}X_6$, $B'_a\mathbf{Bi}_bX_{a+3b}$ (A = Cs^+, MA^+ and bulky organic ligands; B' = Ag^+, Cu^+; X = I^-, Cl^-, Br^-) and bismuth triiodide (BiI_3) semiconducting material particularly focusing on their structure, optoelectronic properties and the influence of compositional variation on the photovoltaic device performance and stability.

Graphical abstract

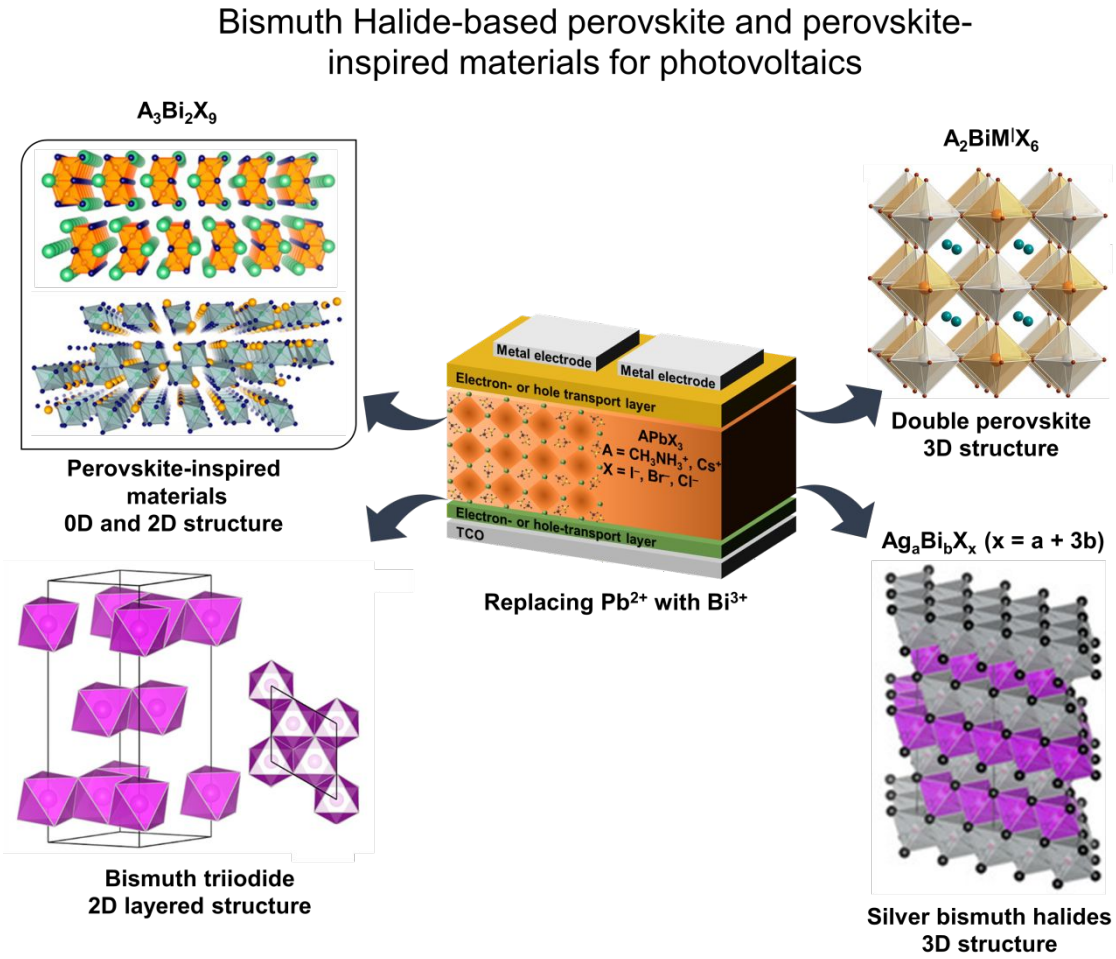

1. Introduction

Organic-inorganic hybrid lead halide perovskite solar cells (PSCs) have demonstrated notable progress in the field of photovoltaics.[1–6] The interdisciplinary nature of perovskite research, in conjunction with outstanding photophysical properties of perovskite such as tunable band gaps[7], long charge carrier diffusion lengths and lifetimes,[8–12] ambipolar charge mobility,[13] and low exciton binding energy (~ 2 meV to 50 meV)[14–16] have resulted in their excellent photovoltaic performance. Since the seminal work by Miyasaka and co-workers,[1] the power conversion efficiency (PCE) of PSCs has rapidly increased to overcome 25%,[5,17] to approach the maturity level of best crystalline silicon solar cells (26.7% record).[18,19] Halide perovskites are defined by a general formula of ABX_3, where A is a monovalent cation e.g. organic methylammonium (MA^+) or formamidinium (FA^+) or inorganic cesium (Cs^+), B is a divalent metal cation (e.g. lead (Pb^{2+}), tin (Sn^{2+})), and X is a halide anion (e.g. I^-, Br^-, Cl^-).[20] The optoelectronic properties of these perovskite materials can be effectively tuned by facile intermixing of suitable anion or cation combinations at A-site ($A^1_{1-x}A^2_xBX_3$), B-site ($AB^1_{1-x}B^2_xX_3$), X-site ($ABX^1_{3-x}X^2_x$) or even all three possible sites at once ($A^1_{1-x}A^2_xB^1_{1-y}B^2_yX^1_{3-z}X^2_z$). The tolerance factor t,[21] defined as the ratio of the distance A−X to the distance B−X in a solid-sphere model with ionic radii R by $t = (R_A + R_x)/(\sqrt{2}R_B + R_X)$ and the octahedral factor μ[22], defined as $\mu = R_B/R_x$ determines the possible crystal structure and its crystallographic stability. In addition, the inorganic metal halide framework of the octahedral network strongly influences optoelectronic properties of the perovskite materials. Methylammonium lead iodide ($CH_3NH_3PbI_3$), a widely explored perovskite absorber in photovoltaic cell is characterized as an intrinsic semiconductor[23] that exhibits excellent mobilities for both photogenerated electrons and holes. **Figure 1** shows the crystal lattice structure of $CH_3NH_3PbX_3$ (X = I^-, Cl^-, Br^-) perovskite and band structures of $CH_3NH_3PbI_3$ based on studies of Tanaka et al.[24] and Brivio et al.[25] The Pb 6p orbitals and I 5p orbitals

contributes to the conduction band (CB) and 25% of Pb $6s^2$ lone-pair orbitals contributes to valence band (VB) of $CH_3NH_3PbI_3$. The VB orbitals show strong coupling between I 5p and Pb lone pair $6s^2$ orbitals. The p–p electronic transitions from VB to CB and the high symmetry of $CH_3NH_3PbI_3$, enabled by the lone pair orbital of Pb, contribute to exceptionally high optical absorption coefficients.[26] The strong s-p antibonding coupling (between Pb and I), weak p-p coupling (between Pb and I) and inherent ionic characteristics effectively contribute to the unique defect tolerant nature of hybrid lead halide perovskite semiconductor.[27] This is reflected by the large charge carrier diffusion length which ranges from 1 μm[8] to over 100 μm.[28] Because of the defect tolerant nature of perovskite materials, optimized solar cells made from lead-halide perovskites typically generates open-circuit voltages (V_{OC}) that are within 100 mV of the radiative limit to V_{OC}.[29–33] Thus, the best halide perovskite solar cells approach the radiative limit[34] of V_{OC} more closely than any other solar cell technology except GaAs.[35] To date, perovskite compositions using methylammonium (MA^+), and/or formamidinium (FA^+) as A-site cations (in ABX_3 crystal structure) are employed in top performing cells with efficiency >20%.[6,36,37]

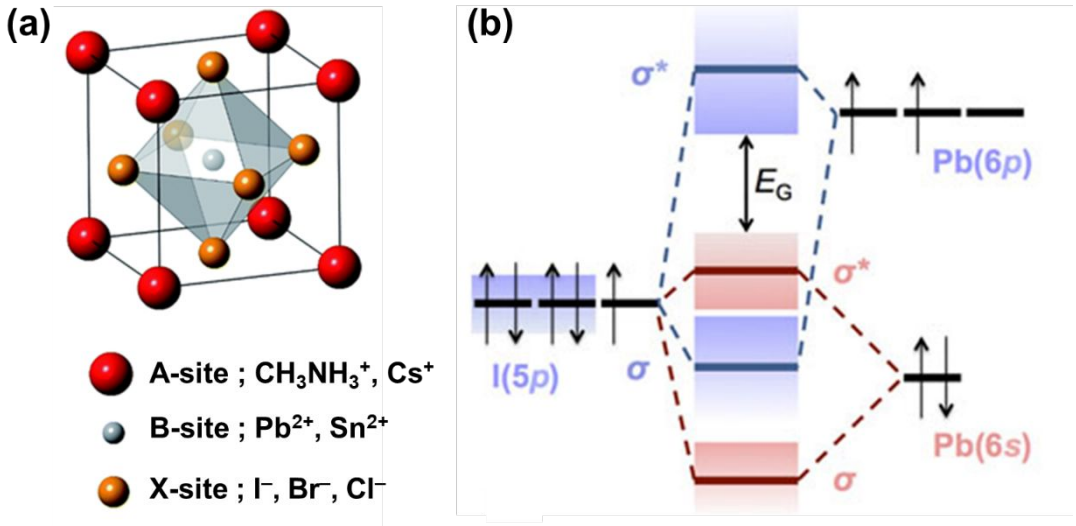

Figure 1: (a) Crystal structure of hybrid metal halide perovskite.[38] *Reprinted with permission.*[38] *Copyright 2014, RSC.* and (b) Orbital diagram of $CH_3NH_3PbI_3$ showing that

the valence band maximum is made up of antibonding (σ*) orbitals (Pb(6s) and I(5p)) colored in red and the conduction band minimum is also made up of antibonding orbitals (Pb(6p) and I(5p)) colored in blue.[39] The antibonding valence band is central to the defect tolerance[40] of $CH_3NH_3PbI_3$ because the atomic orbitals lie outside the band gap, thereby increasing the likelihood that intrinsic defects are shallow or in the bands.[41,42] *Reprinted with permission.*[39] *Copyright 2015, Springer.*

Because of high device performance and interesting optoelectronic properties, perovskites have also triggered fundamental studies on the carrier dynamics, defect tolerance and ion-migration.[43] While some of the properties are valuable for high performance, others are not suitable and impair practical applications of this new technology. For instance, while the defect tolerance of the perovskite material contributes to high device efficiency,[4] the ion-migration phenomenon stands as a potential threat against its intrinsic stability.[44][45] In addition to the intrinsic instability of the material, perovskite stability is also affected by external stimuli. The hygroscopic A-site organic cations such as MA^+ or FA^+ are eliminated when exposed to moisture, heat, light and oxygen.[46–52] **Figure 2a** shows the degradation of $CH_3NH_3PbI_3$ in the presence of moisture. Towards this end, the perovskite reportedly forms a monohydrated phase, that is, $CH_3NH_3PbI_3{\cdot}H_2O$ consisting of $[PbI_3]^-$ double chains. This monohydrated phase can be reversibly converted to perovskite; however, further hydration of this phase results in degradation of the perovskite to PbI_2 and aqueous CH_3NH_3I solution.[51,52] **Figure 2b** shows the heat-induced decomposition of $CH_3NH_3PbI_3$ which varies depending on temperature. At temperature < 200 ˚C, $CH_3NH_3PbI_3$ induces movement of ionic species and distortion of crystal lattice, releasing PbI_2, CH_3NH_2 and HI as byproducts. For temperature > 200 ˚C, $CH_3NH_3PbI_3$ degrades to PbI_2, CH_3I and NH_2.[49][53] This instability issue of the hybrid perovskites makes it incompatible with a desired device lifetime of decades.[53][54] As a

result of degradation, the photoactive perovskite transforms into non-photoactive constituents, thereby releasing lead iodide into the environment which is inherently toxic.[55–57]

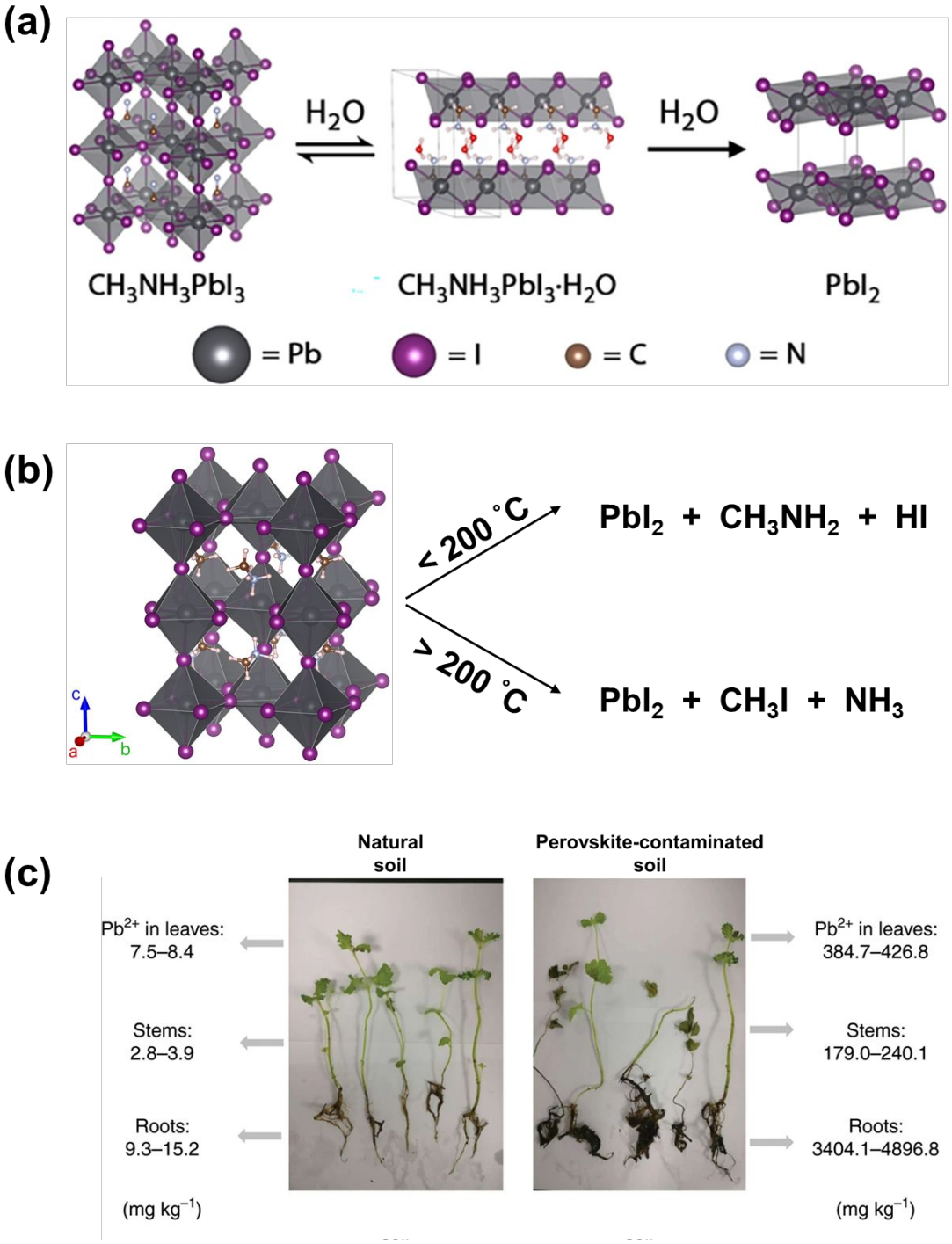

Figure 2: $CH_3NH_3PbI_3$ perovskite degradation in the presence of (a) moisture (*Reprinted with permission. Copyright 2020, Wiley-VCH*),[53] and (b) heat. (c) Concentration of lead measured in mint plants measured in roots, stem and leaves after 20 days of growth in natural soil and perovskite contaminated soil. *Reprinted with permission.*[55] *Copyright 2020, Nature publisher.*

Lead has a long history of affecting human environment. Although, we have been surrounded by metallic lead in our day-to-day life, for instance, lead is still used in batteries, silicon (Si) solar panels, coins, and household paints. It is the presence of lead (Pb^{2+}) in perovskite in ionic form that makes lead perovskites potentially more hazardous as compared to environmental damage caused by metallic lead.[3,56] The presence of Pb^{2+} in human body remains undetected by the immune system as it can mimic other biological important ions such as calcium (Ca^{2+}), iron (Fe^{2+}) and zinc (Zn^{2+}).[56] This can cause severe damage to the nervous and reproductive systems and to hematopoietic and renal organs.[56] In addition to this, lead poisoning can also result in hypertension, anemia, neurological disorder and kidney damage.[58] According to the U.S. Department of Health and Human Service, children and pregnant women are more vulnerable to an exposure to lead, while lead absorption has found to be lower in adults.[56] In addition to this, the exposure of ionic lead to soil and water can result in long-term damage to environment and human health.[56,59,60] Considering 1 m^2 solar panel having a 300 nm $CH_3NH_3PbI_3$ perovskite layer, Hailegnaw et al.[61] performed calculations to determine the concentration of lead (Pb^{2+}) in the soil after its degradation. With the mixing of degraded perovskite in soil, containing 0.42 g of lead, the concentration of lead increases to 70 ppm (assuming soil density to 1.95×10^5 g/m^2). The local concentration would eventually decrease with the effect of rain leading to dispersion of lead in further depth of soil, which would make lead available for uptake by plants. Recently, Li et al. reported that lead originating from perovskite contamination of the water and soil can enter plants and subsequently into the human food cycle.[55] This is more effective compared to other lead contaminants such as lead acid batteries attributing to the presence of hygroscopic organic A-site cations. As discussed above, the degradation of $CH_3NH_3PbI_3$ perovskite releases PbI_2, CH_3NH_2 and HI as side products.[53] The dissolution of HI in the soil decreases its pH, thus

making it more acidic. This increases the solubility of ionic lead in soil and thus increases the availability of lead to plants. A recent study comparing the concentration of lead in leaves, stem and roots of a mint plant revealed the eco-toxicity aspect showing that the mint plant grown in lead perovskite contaminated soil showed blackening and rotting, eventually causing death of the plants (**Figure 2c**).[55] For this purpose, the mint plants were grown in natural soil and in lead perovskite contaminated soil. It can be noted that natural soil also has Pb contamination from electronic waste, mining etc. It was found that natural soil has a Pb concentration of 36.3 mg/kg and with the contamination of soil with perovskite this concentration increased to 250 mg/kg. Due to the release of HI (from perovskite) into the soil, the lead uptake in plants increased by 366 times.

An important question arises here: Is lead absolutely essential for high performing solar cells or is it possible to fully replace lead with less toxic metals without sacrificing optoelectronic properties and simultaneously improve the stability? In this regard, significant efforts have been made to replace lead with less toxic metals and investigate their photovoltaic performance. In this topical review, we initially give a brief summary of various alternative low-toxic metals that have been employed to replace toxic lead and discuss the main issues in preparing the stable photovoltaic cell. Further, we discuss efforts made to develop bismuth (Bi^{3+}) based materials mainly focusing on double perovskites and perovskite-inspired lower and higher dimensional semiconducting materials and their potential applications in photovoltaic devices. Accordingly, we discuss critical future challenges encountered by bismuth-based lower and higher dimensional materials in becoming protagonists in research on eco-friendly and low-cost photovoltaics.

2. Alternative Elements for Lead Substitution – A Short Summary

Since the toxicity and the bioaccumulation in the ecosystem of the lead content has increased concerns, it is one of the most important aims to develop lead-free perovskites and

perovskite-inspired light absorbing materials, while sustaining some important features. The outstanding features of lead halide perovskites include i) excellent optoelectronic properties such as suitable band gap and high photoactivity ii) solution processability and earth-abundance for economical device fabrication iii) increasing long-term stability and iv) easy scalability for large-area production and commercialization.[4] As described in the previous section, lead (Pb) is the bivalent metal cation in the ABX_3 structure having an s^2 electron lone pair, which contributes to the formation of the valence band in the perovskite.[62] Homovalent substitution of lead by same group elements tin (Sn) and germanium (Ge) has been investigated thoroughly in the past years.[63,64] The initial approach was to replace Pb^{2+} with Sn^{2+} that is chemical homologue having similar ionic radius, oxidation states and reactivity.[65,66] Tin-based perovskites exhibit strong PL emission at 950 nm with an absorption onset at 1000 nm and band gap of 1.3 eV, which could be tuned by varying the I/Br ratio.[67] Despite its isoelectronic character of Sn^{2+} and exceptional optoelectronic properties, the low redox potential (-0.15 V) of Sn^{2+}/Sn^{4+} is responsible for the rapid oxidation of Sn^{2+} to Sn^{4+} when exposed to ambient atmosphere. This oxidation is further accelerated by aqueous environments leading to the release of hydroiodic acid (HI) as a by-product.[56] This oxidation leads to the self-doping in the tin-based perovskite materials with Sn^{4+},[68,69] thus impairing the solar cell performance due to bulk recombination of the generated excitons at the defect centres. Secondly, the increase in Sn^{4+} is detrimental for the materials stability due to loss of the perovskite structure.[70]

The efficiency and stability of Sn^{2+} perovskite solar cells have been improved by suppressing the self-doping effect with various additives such as SnF_2[71,72], $EDAI_2$[73], $SnCl_2$[74,75] , SnI_2[75], pyrazine[76], Sn[77], MACl/FACl[78], and NH_2GACl[79] leading to the suppression of Sn^{4+} formation, improved thin film morphology and thus reduced trap-state density. The incorporation of reducing additives such as hydrazine[80] (N_2H_4) and

hypophosphorous acid[81] (H_3PO_2) in the presence of excessive SnF_2 have been observed to inhibit its adverse effect on the perovskite layer contributing to an improved stability. Tai *et al.* developed another method to suppress the oxidation of Sn^{2+} by means of employing hydroxybenzene sulfonic acid or its salt as an additive in the precursor solution along with excess $SnCl_2$.[74] Small amounts of this reducing agent (1.5 mol.%) enabled an almost oxygen-resistant perovskite film yielding a PCE of 6.76% in an inverted PSC. Beside the *in-situ* encapsulation the presence of the additives in the perovskite film eliminated phase separation which is approved by maintaining 80% of its initial efficiency over 500 h upon air exposure.[74] Recently, a mixture of SnF_2 additive with dihydropyrazine derivative was used to produce Sn(0) nanoparticles in the precursor solution to reduce the Sn^{4+} impurities.[82] Additionally, A-site cation engineering was employed as a useful strategy to further enhance the stability, Zhao *et al.* fabricated the double-cation $FA_{0.75}MA_{0.25}SnI_3$ perovskites with 10 mol% SnF_2 integrated in a p-i-n device architecture which achieved a PCE of 8.12%.[71] Furthermore, combinations of formamidinium (FA) with bulkier A-site cations like phenyl ethylammonium (PEA)[72], guanidinium (GA)[73] or 4-(aminomethyl)piperidinium (4AMP)[83] leading to 2D/3D perovskites manifested increased stability. Surface treatments with organic ligands such as ethylene diamine[84] or 2-fluoro-phenethylammonium iodide[85] improved the photovoltaic device performance up to 10%, owing to surface passivation and decrease of self-oxidation. Despite the above mentioned improvements, tin-perovskite devices were fabricated and stored in nitrogen atmosphere, and to best of our knowledge there are no reports on long-term stability under ambient atmosphere.[86] Apart from $CsSnI_3$ thin-film-based devices showing PCEs up to 5%[87], $CsSnX_3$ ($X = I^-, Cl^-, Br^-$) quantum rods have also been explored demonstrating high efficiency up to 13% and better thermal and air stability compared to $MAPbI_3$ reference devices.[88] Alternatively, Sn^{4+}-based Cs_2SnI_6 was investigated as possible solar absorbers. The band gap of Cs_2SnI_6 was found to strongly depend on the thin-film fabrication condition and different values have been reported ranging from 1.3 eV to

1.6 eV.[89,90] Moreover, halide mixing between iodide and bromide resulted in better band alignment with neighbouring transport layers and the resultant device showed enhancement in the PCE up to 2%.[91]

Being directly above Sn in the periodic system, Germanium (Ge^{2+}) was also investigated as a suitable candidate for replacement of lead. For instance, Krishnamoorthy et al. investigated $CsGeI_3$, $MAGeI_3$ and $FAGeI_3$, which showed tuneable band gaps from 1.63 to 2.0 to 2.35 eV, respectively. To date, $CsGeI_3$ and $MAGeI_3$ based photovoltaic devices were fabricated with PCEs of 0.11 % and 0.2 % respectively.[92] Similar to Sn^{2+}, Ge^{2+} is also more stable in the +4 oxidation state leading to the same self-oxidation tendency like in tin perovskites. By replacing widely used spiro-OMeTAD with poly(3-hexylthiophene) (P3HT), Huang et al. reported improvement in the $CsGeI_3$ device performance up to 3.2% which is to date the highest efficiency reported in Ge-based PSCs.[93] Binary perovskite compounds of tin and germanium showed better PV performances in comparison to pure Ge-based PSCs. The implementation of such a binary Sn-Ge perovskite structure in a PSC was firstly reported by Ito et al. with $FA_{0.75}MA_{0.25}Sn_{1-x}Ge_xI_3$ perovskite composition containing 0.05% of Ge. The resultant device showed improved device performance of 4.48% compared to the pure tin PSC with 3.31%.[94] Lifetime measurements demonstrated an increased efficiency of 6.90% after 72 h storage in nitrogen atmosphere which indicated an improved stability compared to the reference device. A higher efficiency of 7.11% has been obtained with a conventional planar $CsSn_{0.5}Ge_{0.5}I_3$ based PSC. Chen et al. observed that the formation of an ultrathin (>5 nm) germanium oxide layer with a self-encapsulation function contributes to an improved device stability against air and moisture.[95] Further, compositional and thin-film engineering strategies were employed by Hayase and co-workers, and the device incorporating Ge-doped $(FA_{0.9}EA_{0.1})_{0.98}EDA_{0.01}SnI_3$ perovskite (EA = ethylammonium and EDA = ethylenediamine) showed PCE of 13%. The incorporation of the EA cation lead to an increase of the open-

circuit voltage (V_{OC}) due to better alignment of the energy band levels of the perovskite with the charge transport layers. Further post-treatment with the Lewis base EDA passivated the surface defects through interaction with undercoordinated Sn sites, resulting in an increase of the V_{OC} to 0.84 V, which is the highest reported for tin based perovskite solar cells.[96] Further, in search of stable perovskite materials, Filip and Giustino performed a computational screening of homovalent metal cations delivering stable perovskite crystal structures and adequate band gap, leading to a number of possible compounds (25 out of 248), where they highlighted magnesium (Mg) compounds e.g. in $CsMgI_3$, $MAMgI_3$ and $FAMgI_3$ as potentially promising candidates.[97] However, these perovskites are highly sensitive towards humidity, which impedes their application in solar cells so far. Moreover, rare earth metals like europium (Eu^{2+}), thulium (Tm^{2+}) and ytterbium (Yb^{2+}) were used as potential dopants in earth-alkali metal perovskites (AMX_3 with A = Cs/K, M = Mg/Ca/Sr, X = Cl/Br/I) leading to efficient photoluminescence emission.[98–100] Furthermore, the perovskite $MAEuI_3$ with an intense blue photoluminescence (PL) emission at 448 nm was patented by Kangning and Mitzi[101], making the rare-earth based perovskites interesting materials for light emitting diodes (LED). Divalent, environment-friendly, earth-abundant and cost-effective transition metals, e.g. Fe^{2+}, Cu^{2+}, Zn^{2+} have also been considered as suitable alternatives to Pb^{2+}. However, in these materials, due to their smaller radii, the 3D perovskite structure is sterically hindered and a layered 2D perovskite structure with the general formula $(R\text{-}NH_3)_2A_{n-1}M_nX_{3n+1}$ is favoured, thereby limiting the photovoltaic efficiency due to wider band gaps and inefficient charge transport. Cortecchia et al. reported copper based 2D perovskites with the formula $(CH_3NH_3)_2CuCl_xBr_{4-x}$. It was observed that $(CH_3NH_3)_2CuBr_4$ was highly air sensitive and halide mixing with Cl^- improved its stability against ambient atmosphere. Moreover, it was observed that optical properties strongly depend on the Br/Cl ratio, exhibiting band gaps between 2.48 eV to 1.8 eV for increasing bromide content. However, the achieved PCEs were below 0.1%.[102] Further, solution processed (p-F-C_6H_5-

$C_2H_4NH_3)_2CuBr_4$ and $(CH_3(CH_2)_3NH_3)_2CuBr_4$ were employed as potential photoabsorbers due to a band gap of 1.75 eV achieving PCE of 0.51% and 0.63%, respectively.[103] Elseman et al. highlighted the role of halides in the MA_2CuX_4, where chlorine (Cl^-) was found to stabilize the perovskite compounds and MA_2CuCl_4 yielded the highest PCE of 2.41%.[104] Another interesting substitutent for lead is titanium (Ti^{+4}) as shown in the Cs_2TiBr_6 antifluorite structure, which is a vacancy-ordered double perovskite having a 3D framework with band gap of ~1.8 eV. First solar cell application of Cs_2TiBr_6 thin films synthesized via vapor deposition from $TiBr_4$ and CsBr was reported by Padture and co-workers, with a PCE of 3.3%.[105] Further, it was reported that halide substitution in $Cs_2Ti_xBr_{6-x}$ can modulate the band gap between 1.0 – 1.8 eV making this material interesting for single-junction and tandem solar cell applications.[106] In contrast to this, Mitzi et al. and Mendes et al. independently reported that both Cs_2TiBr_6 powder and thin films are not stable in air.[107,108]

Similar to Pb^{2+} and Sn^{2+}, bismuth (Bi^{3+}) and antimony (Sb^{3+}), have similar stereochemical inactive s^2 lone pair yielding big ionic radius and contribution to the valence band. This results in high density of states, high dielectric constant, strong absorption coefficients and high defect-tolerance.[39,109] The heterovalent substitution of lead in perovskites was experimentally realized with Bi^{3+} or Sb^{3+} due to above mentioned electronic properties and the affinity of these cations to form metal halide octahedra. Capitalizing on their excellent chemical stability in trivalent form and low-toxicity, research on photovoltaics based on Bi^{3+} and Sb^{3+}-based perovskites and perovskite-inspired materials have emerged as a new, largely explored sector for solar cells leading to several for bismuth-containing potential light absorbers. Both Bi^{3+} and Sb^{3+} based perovskite derived materials form lower dimensional $A_3M_2X_9$ structures that show superior stability against air and moisture.[110,111] Hebig et al. reported on $MA_3Sb_2I_9$ as a zero-dimensional dimer perovskite structure constituted by face-sharing bioctahedral $(Sb_2I_9)^{3-}$ units surrounded by three MA^+ cations. The

$MA_3Sb_2I_9$ thin film with a band gap of 2.14 eV was employed in the inverted structure of solar cells (ITO/PEDOT:PSS (25 nm)/absorber/PC61BM (60 nm)/ZnO-NP (60 nm)/Al (150 nm)) to obtain a device showing PCE of 0.5%.[112] By employing hydroiodic acid (HI) as additive to control the thin film growth, Boopathi et al. obtained high-quality thin films of $MA_3Sb_2I_9$ leading to a PCE of 2.04%.[113] Doping Sn^{4+} in $MA_3Sb_2I_9$ with was found to be beneficial for band gap tuning with band gap decreasing with increasing amount of Sn^4 in$MA_3(Sb_{1-x}Sn_x)_2I_9^+$. The p-i-n structure with device stacks of ITO/Cu:NiO/ $MA_3(Sb_{1-x}Sn_x)_2I_9$/ZnO/Al with x = 0.40 having a band gap of 1.53 eV showed a PCE of 2.69%.[114] Recently, Nazeeruddin and co-workers presented a controlled growth of two-dimensional $MA_3Sb_2I_{9-x}Cl_x$ with Li-TFSI additive. The 2D structure was obtained over a controlled $SbCl_3$-LiTFSI intermediate combined with n-butyl acetate as anti-solvent to remove Li-TFSI from the thin film. This combined strategy lead to an improved PCE of 3.34% which is to date highest for low-dimensional Sb-based perovskite-inspired materials.[115] Moreover, among all mentioned alternative metal cation for lead substitution bismuth-based perovskite and perovskite-inspired material showed leading efficiency, after tin-based perovskites. **Figure 3** shows the summary of potential A-site cations, metals and halides employed to develop lead-free perovskite and perovskite-inspired absorbing materials and record efficiency of representative solar cells compared with $Cs_x(MA_{0.17}FA_{0.83})_{(100-x)}Pb(I_{0.83}Br_{0.17})_3$ lead halide perovskite solar cells.[116] Apart from this, the major studies on the toxicity of bismuth showed that it is not toxic to humans which is in contrast to other alternative metals, where especially SnI_2 was showed to be even more toxic than PbI_2 (LC_{50} for SnI_2 0.09 vs. PbI_2 0.83 mM).[117] The following section provides an overview of recent developments on bismuth halide perovskite and perovskite-inspired materials. Moreover, we discuss and highlight the interrelation between structural, optoelectronic and photovoltaic characteristics in evaluating each class of Bi-halide based materials.

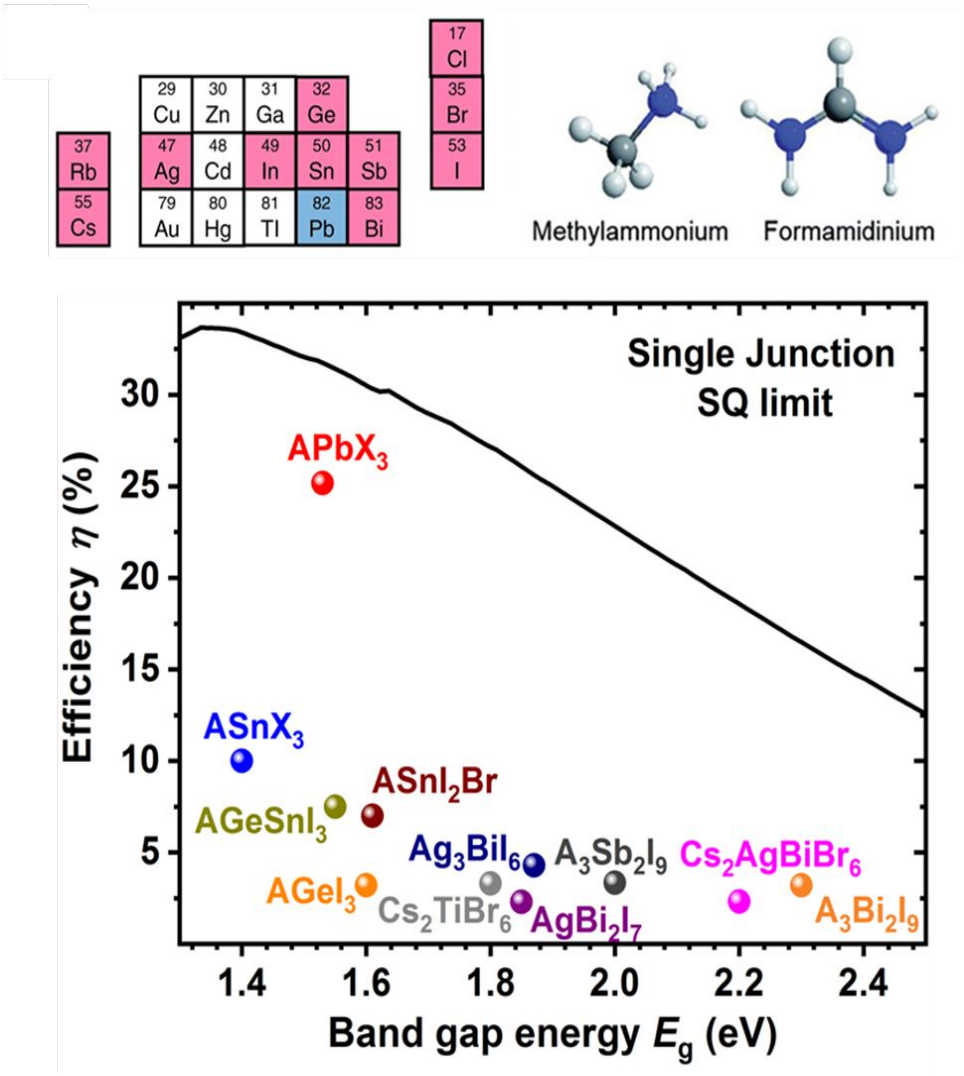

Figure 3: Potential A-site, central metal atom and halide anions employed to develop lead-free perovskite and perovskite-inspired materials (above) and band gap vs. record device efficiencies of their representative solar cells (below).

3. Bismuth-based semiconductors for photovoltaic applications

The classic perovskite structure ABX_3 consists of an inorganic framework, which is built up by a 3D arrangement of corner-connected metal halide octahedra BX_6 as observed in the parent organic-inorganic lead perovskite e.g. $CH_3NH_3PbI_3$ or the α-phase of $CsPbI_3$. The size of the A-site cation influences the inorganic framework by tilting the metal halide octahedra, contraction or expansion of the perovskite lattice or destroying the 3D network and thus the real perovskite structure. It should be noted that from a crystallographic point of view, the

perovskite structure is clearly defined with a stoichiometry of ABX_3 (or also A: B: X with ratio 1: 1: 3) with octahedra forming a 3D network.[118] However, in search of lead-free halide materials, researchers have developed alternating compositions, for instance $Cs_3Bi_2I_9$, $AgBi_2I_7$, 2D layered structures, that are also mostly incorrectly grouped as perovskites. For the sake of "chemical correctness", all other structures not having the classical ABX_3 perovskite structure will be named as perovskite-inspired materials such as $MA_3Bi_2I_9$. The so-called 2D perovskites with a layered structure consisting of octahedra connected along two octahedral axes. In crystallographic terms the 2D perovskite-type structure can be obtained by slicing the 3D structure along specific crystallographic planes. If these are further sliced perpendicular to the inorganic sheets, an octahedral chain remains yielding 1D perovskite-inspired material. If the octahedra are isolated, the structure is named 0D perovskite-inspired material.[119] Bi^{3+} form similar octahedral structures with halides and as a heavy metal, having a distinct spin-orbit coupling, it is expected to show similar band structure as Pb perovskites. Moreover, bismuth based materials show high dielectric constants (ε_r ~38 at ~10^4-10^6 Hz at 300K)[120] and high stability.[121] There are a number of bismuth-based materials that have been tested for solar cell application and will be presented in the following sections starting from perovskite and perovskite-inspired structures such as low-dimensional $A_3Bi_2I_9$ structure, 3D double perovskites $A_2B'BiX_6$, perovskite-inspired 3D rudorffite materials $B'_aBi_bX_{a+3b}$ (A = MA^+, Cs^+; B' = Ag^+, Cu^+; X = I^-, Cl^-, Br^-) and non-perovskite 2D BiI_3.

3.1.Low dimensional $A_3Bi_2X_9$ bismuth perovskite-inspired materials

3.1.1. Structure

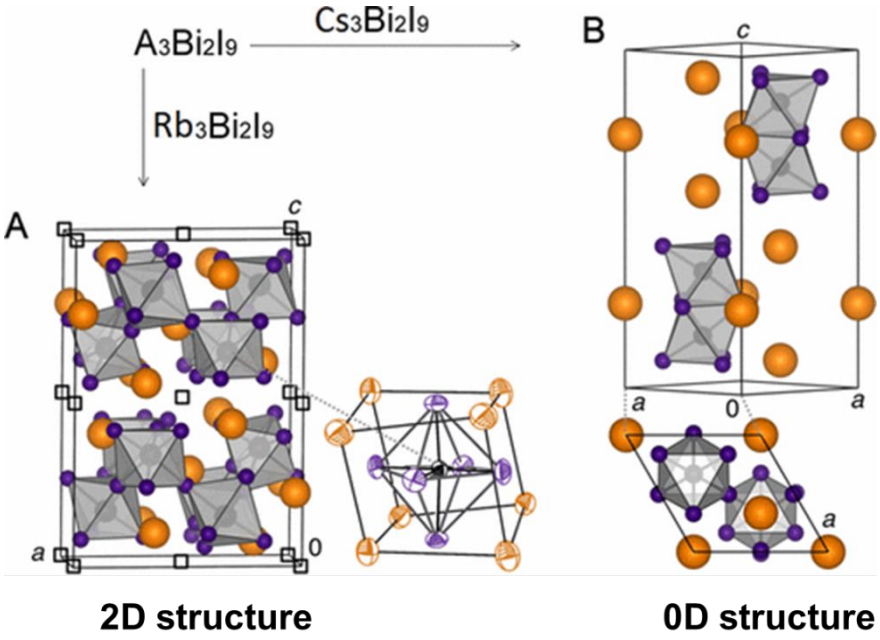

Figure 1: (a) $A_3Bi_2I_9$ structure with a 2D vacancy-ordered perovskite structure and (b) 0D non-perovskite structure with isolated dimeric face-shared octahedra. *Reprinted with the permission of American Chemical Society, Copyright 2017.*[119]

There are two structure types in $A_3Bi_2I_9$ stoichiometry (**Figure 4**) exhibiting a 0D and 2D structural arrangements. In vacancy-ordered Bi-based perovskite-inspired materials such as in $K_3Bi_2I_9$ or $Rb_3Bi_2I_9$, bismuth cations occupy 2/3 of the B-sites, and the vacancies are ordered along the [111] planes leading to a 2D layer of bismuth iodide octahedra. For larger A-site cations such as Cs^+, MA^+ or FA^+ the structure adopts a hexagonal 0D structure in a space group of $P6_3/mmc$, where $[Bi_2I_9]^{3-}$ dimers are isolated and surrounded by the monovalent A-site cations.[110,122] Although this structure is often called a 0D perovskite, it does not comply ABX_3 perovskite structure, thus we term these class of materials as perovskite-inspired material. It was found that there is a phase transition from the hexagonal to the monoclinic phase with the space group C2/c at low 160 K[120] and 130 K[123] for $MA_3Bi_2I_9$ and $Cs_3Bi_2I_9$,

respectively. In case of $MA_3Bi_2I_9$ the disordered dipolar MA cations oriented along the *b* axis inducing a distortion of the BiI_6 octahedra result in the reduced symmetry from hexagonal to monoclinic. Further cooling to 140 K causes a phase transition to the polar monoclinic structure with the space group $P2_1$. Here, the Bi^{3+} ions get displaced more due to the in-plane ordering of the s^2 lone pairs leading to the polarity and thus the large dielectric constant.[120] Zhang et al. showed that this polar monoclinic phase in $MA_3Bi_2I_9$ was also achieved under high pressure at 5.0 GPa.[124]

3.2. Optoelectronic properties

The first investigation on the optical absorption of $MA_3Bi_2I_9$ single crystals was conducted by Kawai et al., exhibiting an excitonic peak at 2.51 eV at 78 K, which showed a red shift (2.49 eV) upon temperature increase to 301 K. The excitonic state near the band-edge was attributed to the transition from $^1S_0$ to $^3P_1$ state localized at the Bi^{3+} in the $(Bi_2I_9)^{3-}$ dimers and an exciton binding energy over 300 meV was estimated.[125] Öz et al. reported the similar excitonic peak at 2.45 eV and determined a band gap value of 2.9 eV for $MA_3Bi_2I_9$ thin film with a PL emission at 751 nm (excitation at 488 nm).[126] In contrast, Abulikemu et al. showed an unchanged PL emission at 637 nm (excitation at 473 nm) for $MA_3Bi_2I_9$ single crystal, powder and thin film and a lower band gap of 1.9 eV, where the excitonic state was not considered.[127] Generally, for $MA_3Bi_2I_9$, the PL show lower peak intensity compared to $MAPbI_3$ and is attributed to the radiative recombination in $(Bi_2I_9)^{3-}$ clusters. An absorption coefficient of $\sim 1.1 \times 10^5$ cm^{-1} was reported for $MA_3Bi_2I_9$, which is comparable to $MAPbI_3$.[128]

Band gap values $E_g = 1.8 – 2.2$ eV were reported for the indirect and $E_g = 2.1 – 2.9$ eV for the direct band gap.[121] The discrepancy of band gap values might be caused by various approaches to their estimation and is dependent on the consideration of the excitation state. Furthermore, thin film properties can lead to these deviations due to different fabrication

methods e.g. one-step coated thin films showed E_g = 2.1 eV[129] whereas thin films grown via atmospheric pressure chemical vapor deposition showed E_g of 1.8 eV.[130] These various fabrication methods such as one-step spin-coating, solvent assisted vapor annealing[127], anti-solvent quenching[131], solvent-engineering[132] or vapor-assisted methods[133] were used to control structural properties such as grain sizes, orientation and crystallinity which impact the optoelectronic properties of the material in general. For example, Zou and coworkers reported band gap narrowing and PL enhancement in $MA_3Bi_2I_9$[124]and $Cs_3Bi_2I_9$[134] under high pressure due to the compression of the inorganic Bi_2I_9 unit and thus increased cation-anion orbital overlap between the Bi 6s and I 5p and Bi 6p and I 5p orbitals as shown in **Figure 5**.

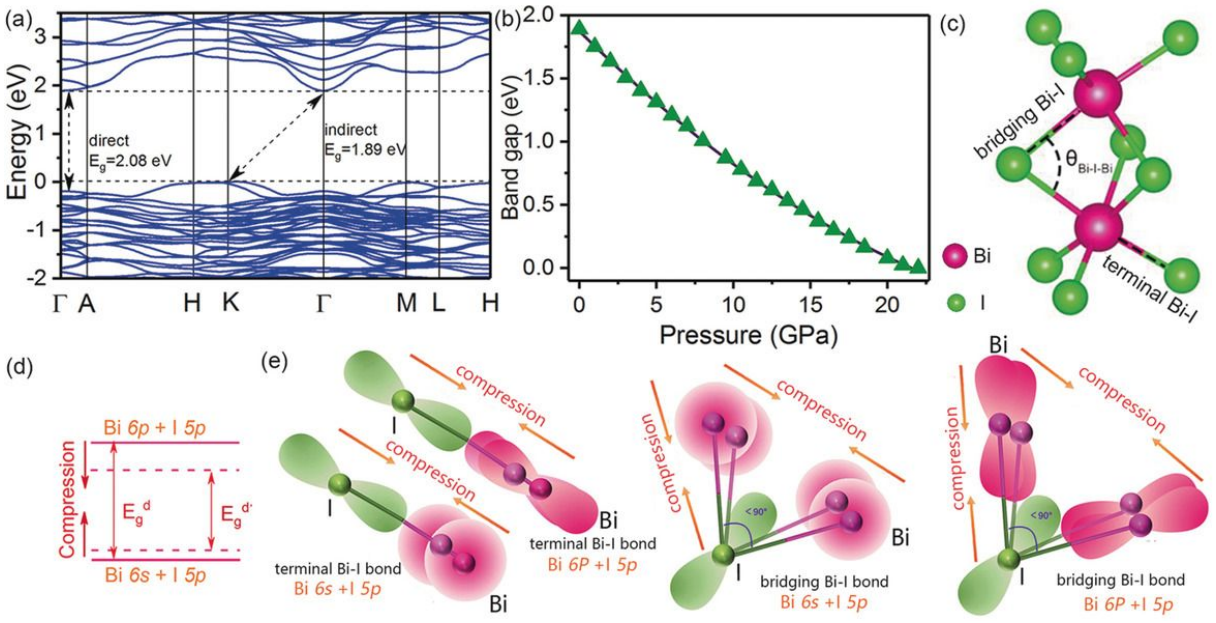

Figure 2: Band gap narrowing through compression of $Cs_3Bi_2I_9$, a) Band structure at ambient conditions; b) Band gap as function of pressure (in GPa); c) Inorganic dimer Bi_2I_9 unit; d) schematic band level diagram showing the band gap narrowing upon compression; e) Schematic orbital models of compression leading to decrease of Bi-I bond contraction and Bi-I-Bi angle and increased orbital overlaps. *Reprinted with permission.*[134] *Copyright 2018, Wiley-VCH.*

Furthermore, Hoye et al. investigated the optoelectronic properties of solution-assisted and vapor-assisted $MA_3Bi_2I_9$ thin films, where the vapor assisted thin films showed enhanced PL decay times compared to the solution-assisted ones.[135] Generally, the band structure of $MA_3Bi_2I_9$ is very similar to lead based perovskites with a partial antibonding character in valence band (VB) and disperse conduction band (CB) leading to higher defect-tolerance (**Figure 6a**).[39] In comparison to Pb 6s orbitals, the Bi 6s orbitals have a smaller contribution to the VB, leading to less cation-anion orbital overlap and thus less dispersion of the VBM. This leads to lower hole mobilities in bismuth based materials and coupled with their low dimensional structure with localized charge carriers at the isolated bioctahedrons causing limited charge transport.[136]

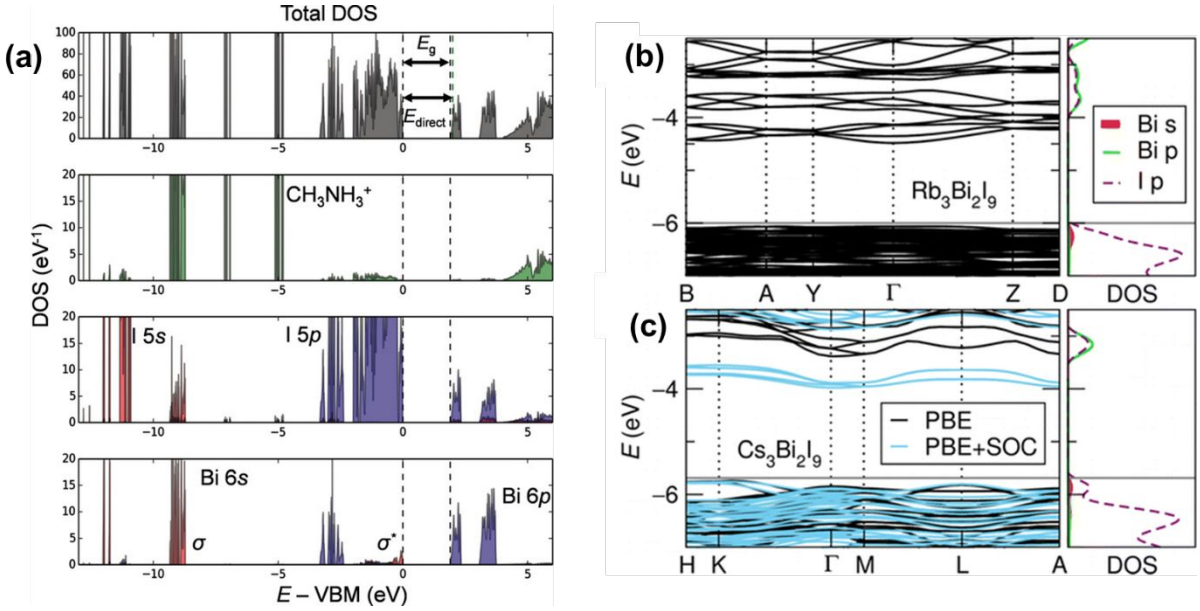

Figure 3: Band structures of $A_3Bi_2I_9$ type materials: a) calculated density of states (DOS) of $MA_3Bi_2I_9$. *Reprinted with the permission of Hoye et al.*[135] *Copyright 2016, Wiley;* b) Band structure and related DOS of $Rb_3Bi_2I_9$ and c) of $Cs_3Bi_2I_9$. *Reprinted with permission of American Chemical Society, Copyright 2015.* [110]

For the all-inorganic $Cs_3Bi_2I_9$, band gaps between 2.16 – 2.2 eV for thin films, 1.9 eV for powder, 1.87 – 1.95 eV for single crystals and 2.86 eV for nanocrystals were reported.[121]

The material showed exciton binding energies between 270 – 300 meV,[129,137] which is higher than lead based perovskites (25 – 50 meV).[129] Lehner et al. calculated a VBM level of – 5.7 eV for $Cs_3Bi_2I_9$, whereas the layered $K_3Bi_2I_9$ and $Rb_3Bi_2I_9$ showed deeper VBM levels at – 6.0 eV with a band gap of 2.1 eV. Furthermore, the VB of the layered perovskites showed a flat curvature and a less dispersed CB compared to the 0D $Cs_3Bi_2I_9$ as can be seen in **Figure 6b** and **Figure 6c**. Compared to the $MAPbI_3$, the overall smaller band dispersion and flat bands lead to lower charge carrier mobilities in the Bi-based semiconductors.[110] The compositional flexibility of organic-inorganic hybrid perovskites and all-inorganic perovskites lead to tunability of optoelectronic properties such as band gap. This was also observed for the bismuth-based perovskite-type materials e.g., variation in the precursor stoichiometry of $Cs_3Bi_2I_9$ and $MA_3Bi_2I_9$ lead to band gap perturbation. In $Cs_3Bi_2I_9$ a band gap decrease was observed from 2.01 eV to 1.77 eV for BiI_3-rich stoichiometry ($CsI/BiI_3 < 1$). This band gap reduction was related to the formation of defects leading to gap states above the VB and a stronger Bi 6p – I 5p overlap moving the band toward the Fermi energy and thus to band gap reduction.[138,139] Another well-established strategy for band gap tuning is the compositional engineering in the A-, B- or X-sites of the perovskite structure, which was also applied in bismuth-based materials. Recently, we reported the variation of different A-site cations in the $A_3Bi_2I_9$ structure with monovalent organic or inorganic A-site cations (Figure 7) leading to change in the band gap (**Table 1**) mainly due to the formation of 0D perovskite-type or 2D layered perovskite structures. Also, A-site cation alloying with Cs and MA cation to obtain double cation bismuth iodide lead to a band gap reduction from 2.9 eV to 2.2 eV.[20]

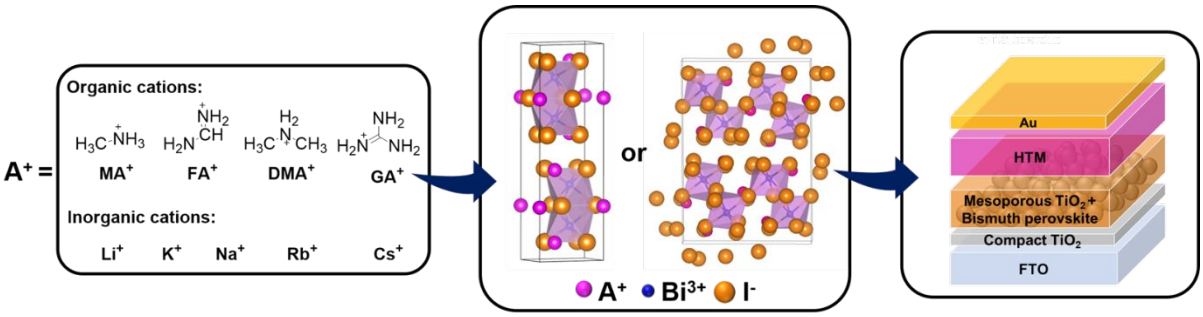

Figure 7: A-site cation engineering in $A_3Bi_2I_9$ perovskite with organic and inorganic monovalent cations for solar cell application. *Reprinted with permission[20] Copyright 2021.*

Table 1: Calculated band gaps from Tauc Plots (assuming a direct band gap) for all-inorganic and organic-inorganic bismuth materials (excitonic band gap refers to the excitonic peak as band edge). Values adapted from Ünlü et al.[20]

	Direct band gap (eV)	
	excitonic	optical
$Cs_3Bi_2I_9$	1.9	2.3
$Rb_3Bi_2I_9$	2.2	2.5
$K_3Bi_2I_9$	2.0	2.3
$Na_3Bi_2I_9$	2.3	2.5
$Li_3Bi_2I_9$	2.3	2.5
$MA_3Bi_2I_9$	2.5	2.9
$FA_3Bi_2I_9$	--	2.6
$GA_3Bi_2I_9$	2.3	2.7
$DMA_3Bi_2I_9$	2.2	2.4

Furthermore, B-site cation engineering was shown theoretically to be a possible method for band gap tuning as reported by Hong et al., showing that trivalent metal cations such as indium (In) or gallium (Ga) can be mixed with Bi to obtain $Cs_3BiM^{1}I_9$ to reduce the band gap. Additionally, these materials exhibited the space group $P\bar{3}m1$ leading to direct and

lower band gaps compared to the space group $P6_3/mmc$.[140] In a different study, Ru^{3+}-doping up to 4.3% was demonstrated as an efficient way to reduce the band gap of $Cs_3Bi_2I_9$ *via* a hydrothermal synthesis method along with shallow defects states and higher work function.[141] The mixing of B-site alloys e.g. in $APb_{1-x}Sn_xX_3$ also allows to tune the bandgap. Similar to Sn-Pb perovskites, where the band gap deviates from the linear interpolation between the band gaps of the pure $APbI_3$ and $ASnI_3$ compounds, also known as band gap bowing,[142] mixture of Sb^{3+} and Bi^{3+} in $MA_3(Sb_{1-x}Bi_x)_2I_9$ reduced the band gap up to 1.9 eV (**Figure 8a**). The band gap bowing was attributed to spin-orbit coupling and lattice strain due to the use of the heavy element Bi.[143]

Halide mixing in $Cs_3Bi_2I_9$ with chloride (Cl^-) was demonstrated by Kanatzidis and coworkers leading to a structural change from 0D to 2D layered structure (similar to $Cs_3Bi_2Br_9$) with the space group $P\bar{3}m1$ achieving a direct band gap (**Figure 8b-c**). The mixed halide $Cs_3Bi_2I_6Cl_3$ showed an excitonic absorption rather than an excitonic peak above the absorption edge as normally observed in $Cs_3Bi_2I_9$, leading to reduced exciton binding energy. However, broad PL emission revealed phonon-assisted recombination of self-trapped excitons with enhanced electron-phonon coupling with Huang-Rhys factor of S_{HR} = 212 which is increased compared to $A_3M_2I_9$ materials (S = 21.2-79.5).[144] Investigation on incorporation of Br^- ions into $Cs_3Bi_2I_9$ was also demonstrated and by comparing the crystal structure, absorbance of $Cs_3Bi_2I_{9-x}Br_x$ and the band structure, it was found that $Cs_3Bi_2I_6Br_3$ has the lowest band gap (2.03 eV vs. 2.20 eV for $Cs_3Bi_2I_9$). This further lead to transition from space group $P6_3/mmc$ to $P3m$ due to alloying of three bromide atoms.[145] Besides the incorporation of halide ions, Li et al. employed low pressure vapour assisted solution process method to obtain $MA_3Bi_2I_{9-x}S_x$. The incorporation of sulfur leads to reduction of band gap to 1.67 eV.[146] Beside from halide mixing, split-anion approach with chalcogenide elements such as tellurium (Te), selenium (Se) and sulfur (S) was theoretically discovered for lower

band gap materials i.e. MA_3BiSeI_2, MA_3BiTeI_2 and MA_3BiSI_2 (**Figure 8d**).[147,148] In addition to halide mixing, to address the band gap issue, Vigneshwaran et al.[149] attempted doping of sulfur into $MA_3Bi_2I_9$ perovskites at relatively lower temperature (120 °C) and observed band gap reduction to 1.45 eV (lower than $MAPbI_3$). Moreover, Hall effect measurements suggested that the resultant perovskite behaves as a p-type semiconductor with higher carrier concentration and mobility compared to undoped $MA_3Bi_2I_9$. However, investigation of the effect of doping and lower band gap on the photovoltaic device performance remains unexplored.

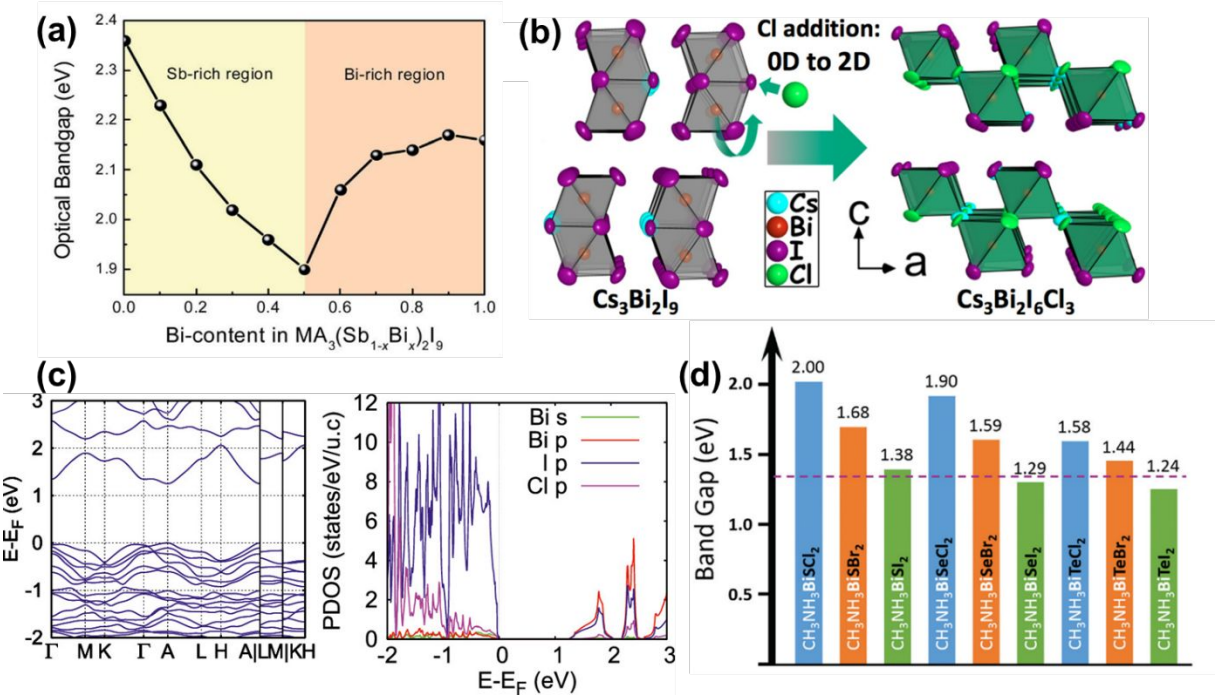

Figure 4: Band gap tuning in 0D perovskite-type materials; a) The optical band gap as function of composition of Sb-Bi-alloys showing band gap bowing; *Reprinted with permission* [143] *Copyright 2020, Royal Society of Chemistry*; b) Halide mixing in $Cs_3Bi_2I_9$ leading to increased structural dimensionality form 0D to 2D layered structure; c) calculated electronic band structure showing a direct band gap and DOS of $Cs_3Bi_2I_6Cl_3$. *Reprinted with permission.*[144] *Copyright 2019, American Chemical Society;* d) Calculated band gaps of the

$MABiXY_2$ compounds obtained via the split-anion approach. *Reprinted with permission.*[148] *Copyright 2016, Royal Society of Chemistry.*

The drawbacks of the low dimensional $A_3Bi_2I_9$ perovskites are i) the 0D electronic structure with localized charge carriers as described above, thus high exciton binding energies which hinder an efficient charge separation resulting in low J_{SC}; ii) wide band gaps leading to lower absorption and iii) broad Urbach tails as shown in **Figure 9a** with Urbach energies E_U being substantially higher than kT representing high energetic disorder that is likely responsible for substantial nonradiative recombination losses.[112] **Figure 9d** shows the influence of Urbach tails (represented as Urbach parameter γ which is identical to the Urbach energy E_U introduced above) in combination with band gap values on solar cell parameters in the radiative (detailed balance) limit (V_{OC}, J_{SC}, PCE and FF). High Urbach parameter combined with higher than optimal band gap energies can lead to drop down of V_{OC}, FF and overall PCE, which can be a problem in lead-free Bi-based materials.[150]

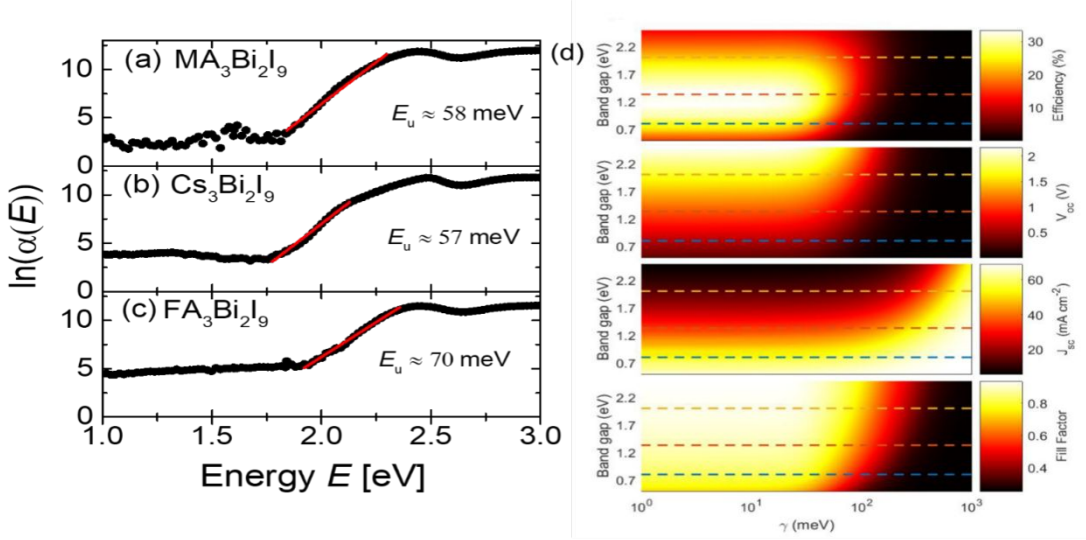

Figure 9: Fitted Urbach energies obtained from PDS measurements using $\exp(E/E_U)$ for a) $MA_3Bi_2I_9$, b) $Cs_3Bi_2I_9$ and c) $FA_3Bi_2I_9$. Adapted from Hebig et al. [112] d) Dependence of solar

cell parameters (PCE, J_{SC}, V_{OC} and FF) on the Urbach parameter $\gamma = E_U$ and band gap according to detailed balance limit calculations. *Reprinted with permission.* [150] *Copyright 2021, American Chemical Society.*

3.2.1. $A_3Bi_2I_9$ perovskite-inspired solar cells

In 2015, Park et al. reported on solution-processed mesoscopic heterojunction solar cells with $Cs_3Bi_2I_9$, $MA_3Bi_2I_9$ and $MA_3Bi_2I_9Cl_x$ yielding PCEs of 1.09%, 0.2% and 0.003%, respectively. The solar cells were fabricated in the commonly used FTO/c-TiO_2/m-TiO_2/absorber/spiro-OMeTAD/Ag architecture, coating the perovskite material *via* one-step spin-coating method (**Figure 10**). The three investigated compositions exhibited different morphologies, while $Cs_3Bi_2I_9$ indicated thin hexagonal sheets with preferred growth along the c-axis, $MA_3Bi_2I_9$ has interconnected platelets and $MA_3Bi_2I_9Cl_x$ showed heterostructures with particles, attributed to phase segregation of $BiCl_3$.[129]

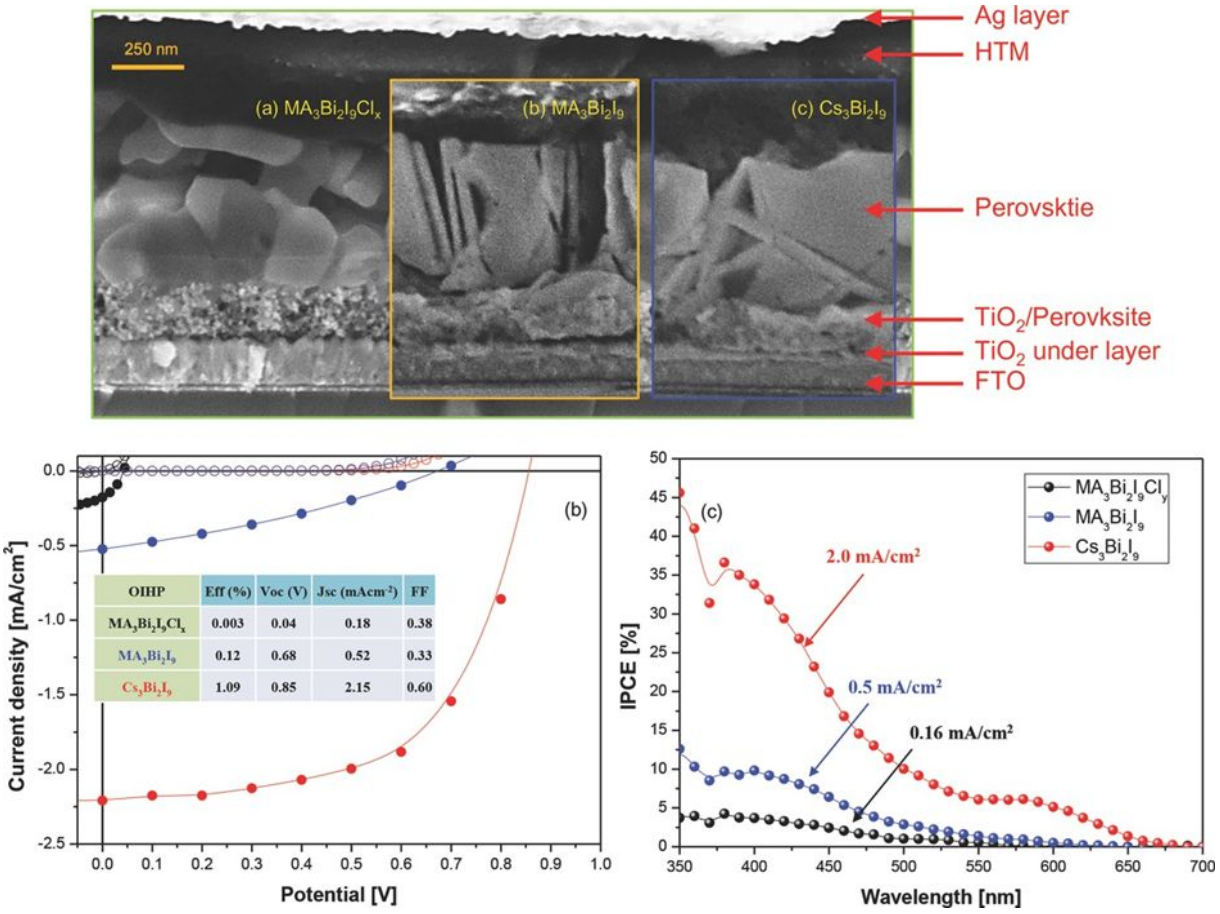

Figure 10: (a) Cross-section SEM of the solar cells based on $MA_3Bi_2I_9Cl_x$, $MA_3Bi_2I_9$ and $Cs_3Bi_2I_9$. (b) Related J-V curves and (c) Incident photo-to-current (IPCE) spectra. *Reprinted with permission.*[129] *Copyright 2015, Wiley.*

In general, further research has shown that Bi-based perovskite-inspired material could easily be made from solution at mild temperatures. However, device PCE showed deviations between reports which have been attributed to the different thin film morphology of the $A_3Bi_2I_9$ structures. For instance, Lyu et al. fabricated solar cells with $MA_3Bi_2I_9$, where the material formed hexagonal shaped crystallites which were randomly oriented on rough FTO/c-TiO_2 substrates while being regular on glass surface. The best performing device with efficiency of 0.19% showed improved stability in air for 21 days.[151] We sandwiched $MA_3Bi_2I_9$ in planar device architecture with device stacks of ITO/PEDOT:PSS/$MA_3Bi_2I_9$/PCBM and showed an initial PCE of 0.1%. The thin film morphology consisted of hexagonal shaped crystallites with an average size of 1-2 μm on

surface of PEDOT:PSS hole transport layer as shown in **Figure 11a**. The low J_{SC} = 0.22 mA/cm^2 was attributed to the calculated high exciton binding energy of 400 meV, which was estimated from the band gap of 2.9 eV. Additionally, the HOMO level of PEDOT:PSS was not well aligned with the VB of $MA_3Bi_2I_9$ leading to the poor performance (**Figure 11b**).[126] We investigated the influence of the TiO_2 structure on the thin film morphology of $MA_3Bi_2I_9$, revealing that on planar compact TiO_2 the $MA_3Bi_2I_9$ thin film growth was non-uniform and had a low surface coverage compared to the mesoporous anatase or brookite TiO_2 underlayers (**Figure 10c-e**). The best performing solar cell with the structure FTO/c-TiO_2/anatase m-TiO_2/absorber/spiro-OMeTAD/Au yielded a PCE of 0.2% maintaining 75% of its initial PCE after 10 weeks in ambient atmosphere.[152]

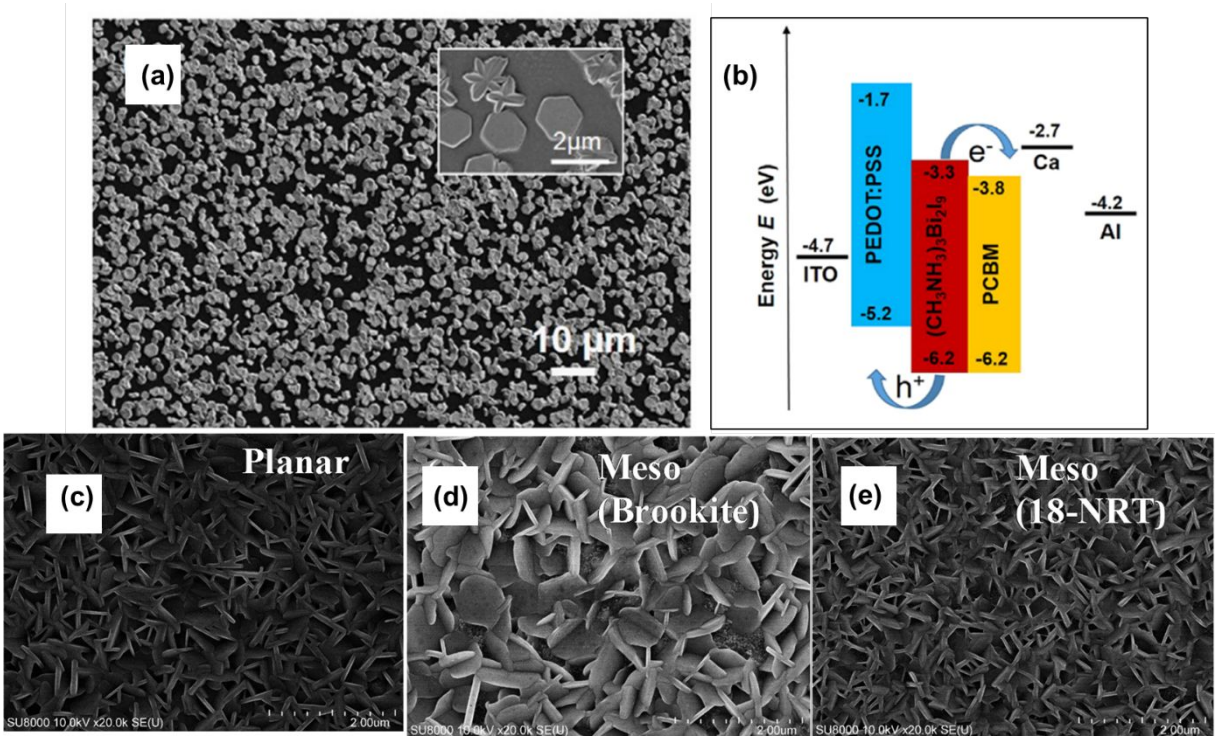

Figure 11: (a) $MA_3Bi_2I_9$ thin film growth from spin-coated solution on PEDOT:PSS layer and (b) the related band energy level diagram of solar cell device with inverted p-i-n structure. *Reprinted with the permission of Öz et al.*[126] *Copyright 2016, Elsevier.* (c) $MA_3Bi_2I_9$ thin film growth from spin-coated solution on planar , (d) mesporous brookite and (e) mesoporous

anatase TiO_2 layers. *Reprinted with the permission of Singh et al.*[152] *Copyright 2016, American Chemical Society.*

Beside the underlayer structure, it was shown that the concentration of the precursor solution and spin-coating speed is also crucial for thin film growth.[153] Zhang et al. demonstrated that 0.45 M precursor solution form the most efficient thin film on m-TiO_2 in the concentration series in the range from 0.1 M to 0.7 M. The solar cell device with ITO/c-TiO_2/m-TiO_2/$MA_3Bi_2I_9$/spiro-OMETAD/MoO_3/Ag structure showed enhanced PCE of 0.42% with J_{SC} = 1.0 mA/cm^2, V_{OC} = 0.67 V and FF = 62.48%.[154] Generally, these bismuth halide based materials crystallize directly and rapidly into a textured polycrystalline microstructure from a precursor solution without going through intermediate crystalline solvated phases, as determined by multi-probe in-situ characterization methods.[155] For good performance of the resulting solar cells, the maintenance of continuous polycrystallinity within $MA_3Bi_2I_9$ films is crucial. A lot of work has been done to optimize the morphology of $MA_3Bi_2I_9$. A strategy to influence the thin film morphology is the use of additives in the precursor solution; we introduced N-methyl-2-pyrolidone (NMP) as a solution additive leading to uniform and high surface coverage of $MA_3Bi_2I_9$ thin films. Solar cell devices with the FTO/c-TiO_2/m-TiO_2/$MA_3Bi_2I_9$/spiro-OMETAD/Au structure were tested with different amounts of the additive, where 2.5 vol% NMP yielded a higher PCE compared to the solar cell without NMP (0.31% with 2.5% NMP vs. 0.19% without any additive).[132] Although significant improvement in the morphology was observed, it was concluded that tuning the intrinsic optoelectronic properties are crucial (rather than morphology) to further improve the performance of $MA_3Bi_2I_9$ solar cells.[132] Further, incorporation of thiourea additive was reported to enhance the grain morphology owing to the formation of a Lewis acid-base adduct with Bi^{3+} and thus slowing down the crystallization to form large grains with high surface coverage and crystallinity (**Figure 12a**). The solar cells with FTO/c-TiO_2/m-TiO_2/$Cs_3Bi_2I_9$/spiro-OMETAD/Au structure obtained a PCE of 1.69% with enhanced

J_{SC} = 4.61 mA/cm^2 (**Figure 12c**).[156] Solvent- and anti-solvent engineering was also employed in the fabrication of 0D perovskite-inspired materials such as $MA_3Bi_2I_9$, $FA_3Bi_2I_9$ and $Cs_3Bi_2I_9$.[131,157] Both methods enable a controlled growth and nucleation process in order to tune the grain morphology. For instance, Shin et al. developed a growth and nucleation mechanism which is directed first by the solvent choice such as a mixture of DMF and DMSO or DMF and tert-butyl pyridine (tBP) to form highly soluble Bi-complexes and thereby retarding the nucleation process during spin-coating and increasing the supersaturation level (**Figure 12d**). Second, anti-solvent dripping during spin-coating initiates the grain nucleation by decreasing the solubility to form uniform and pin-hole free thin films. The supersaturation level can be controlled by the solvent ratios and thus directs the nucleation and growth as shown in **Figure 12e**. Finally, the solvent-engineered $MA_3Bi_2I_9$ thin film (**Figure 12f**) coupled with a more suitable HTL such as polyindenofluoren-8-triarylamine (PIF8-TAA) yielded a PCE of 0.71% and a comparably high V_{OC} = 0.85 V and FF = 0.73.[157] To address the low efficiency issue, Jain et al. developed $MA_3Bi_2I_9$ by vapor assisted solution process in which CH_3NH_3I (methylammonium iodide) vapors were exposed onto solution processed BiI_3 thin-film. Interestingly, concentration of Bi^0 in BiI_3 was substantially reduced and at particular exposure time of 25 min, the device showed record efficiency of 3.17% with V_{OC} of 1.01 V. This was mainly attributed to mitigation of metal defect sights induced by MAI vapors.[158] To make the fabrication of $MA_3Bi_2I_9$ more green/eco-friendly, the same group further demonstrated the fabrication of $MA_3Bi_2I_9$ solar cells by employing non-toxic methyl acetate as solvent and carbon as low-cost electrode, leading to a decent PCE of 1.64%.[159]

In comparison to widely explored $MA_3Bi_2I_9$, $Cs_3Bi_2I_9$ material based solar cells have been less explored. Despite demonstrating initial PCE 1.09%,[129] subsequent reports have shown PCE below 0.1%.[160,161] Ghosh et al. reported that the low performance of $Cs_3Bi_2I_9$ is mainly caused by its wide band gap coupled with the presence of deep level defects. Density

functional theory calculations unveiled that the defects types such as iodine vacancies (V_I) and cation substitution (Cs_{Bi}) have low formation energy and create deep level states hence acting as possible recombination centers.[160] On the other hand, Bai et al. demonstrated that in a dissolution-recrystallization process which includes an additional spin-coating step after crystallization of the material with DMF/MeOH solvent dripping, ultrathin nanosheets of $Cs_3Bi_2I_9$ can be obtained leading to superior PCE of 3.2% with CuI as suitable HTL. This method resulted in pin-hole free and uniform surface coverage along with high crystallinity which is crucial for efficient charge transport.[162] In addition to this, the solar cell performance of $Cs_3Bi_2I_9$ was shown to be sensitive to the precursor stoichiometry due to the effects on the optoelectronic properties (**see section 3.2.**). BiI_3-rich stoichiometries can lead to an enhancement of the PCE compared to the neutral stoichiometry due to defect passivation and the co-existence of 0D $Cs_3Bi_2I_9$ and 2D BiI_3.[82, 99] Hu et al. constructed bulk heterojunction based on $Cs_3Bi_2I_9$ and $Ag_3Bi_2I_9$ bismuth halide materials and the device showed record PCE of 3.6% with unprecedented high V_{OC} of 0.9 V owing to increased crystal size of $Cs_3Bi_2I_9$ and optimized grain orientation of $Ag_3Bi_2I_9$. The resultant device maintains 90% of its initial efficiency after 450 h against thermal stress.[163]

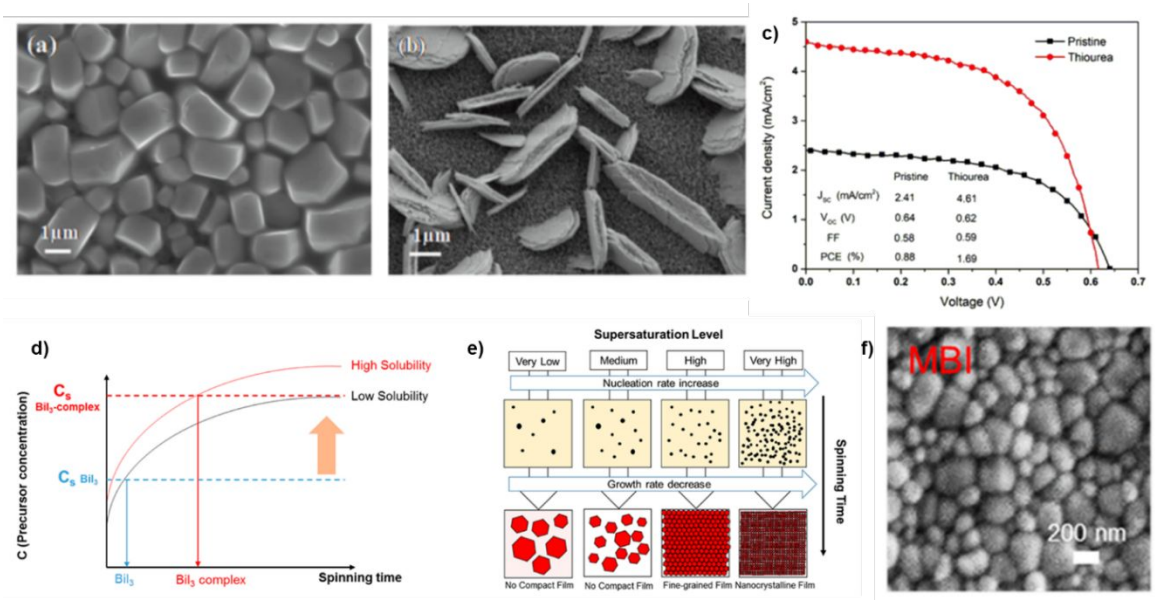

Figure 12: Additive- and solvent-engineering for morphology enhancement; $Cs_3Bi_2I_9$ thin films with (a) thiourea and (b) without additive and (c) related J-V curves. *Reprinted with permission* [156] *Copyright 2020, American Chemical Society.* (d-e) The mechanism of growth and nucleation of thin films depending as a function of supersaturation level and spinning time and (f) obtained $MA_3Bi_2I_9$ thin film using the solvent-engineering method. *Reprinted with permission* [157] *Copyright 2018, American Chemical Society.*

Although not widely explored, A-site cation engineering has been used to discover new bismuth-based compositions for solar cell application.[20,164,165] Recently, we demonstrated bismuth halide materials based on various organic and inorganic A-site cations and their photovoltaic performance from compositions with organic A-site cations $FA_3Bi_2I_9$ (0.02% PCE), $GA_3Bi_2I_9$ (0.011% PCE), $DMA_3Bi_2I_9$ (0.017% PCE) and inorganic $K_3Bi_2I_9$ (0.1% PCE), $Rb_3Bi_2I_9$ (0.1% PCE) and $Na_3Bi_2I_9$ (0.15% PCE). Moreover, we also showed dual A-site cations based bismuth halide materials and observed better reproducibility and higher PCE up to 1.5% for a particular composition of $(Cs_{0.1}MA_{0.9})_3Bi_2I_9$ attributing to band gap reduction and better morphology.[20] Such kind of compositional engineering of A-site cation needs further attention in terms of understanding their structural, optoelectronic properties and improve the device performance and stability. In addition to the less-explored

A-site cation engineering, very few papers have demonstrated B-site cation engineering. For instance, Chatterjee et al.[143] demonstrated band gap bowing effect in $MA_3(Sb_{1-x}Bi_x)_2I_9$ alloys, showing band gaps less than their mono-cation based counterparts. Because of this, photovoltaic device showed PCE of 1% for equimolar substitution.[143] Besides this, anion-engineering with sulfur incorporation into $MA_3Bi_2I_{9-2x}S_x$ resulted in reduced band gap up to 1.67 eV. Bismuth ethyl xanthate was used as precursor along with MAI achieving a sulfur incorporation which effected a uniform grain morphology yielding a PCE of 0.152%.[146] In addition to the above mentioned methods, several other methods were shown to control the thin film growth and morphology targeting smooth and uniform thin films such as gas-quenching (PCE 0.082%)[166], two-step spin-coating method (PCE 0.27%)[167], two-step combined method, in which first BiI_3 was thermally evaporated and then MAI/IPA solution was spin-coated leading to a high V_{OC} = 0.83 V for $MA_3Bi_2I_9$ (**Figure 13**).[168] In another two-step method, where first BiI_3 was deposited under high vacuum and then MAI was evaporated, Zhang et al. reported comparably high PCE of 1.64% due to highly uniform film morphology with large grains of $MA_3Bi_2I_9$ thin film.[169] Chemical vapor deposition of $MA_3Bi_2I_9$ was shown to be effective for high quality thin films, but the PCE is still below 1% for these evaporation based techniques.[133,170,171] In an electric-field assisted spray coating method, Mohammad et al. presented that the thin film morphology of $MA_3Bi_2I_9$ was strongly influenced by the applied electric field leading to big grains under high voltage and thus an enhancement of the PCE (0.17%) compared to the absence of an electric-field (0.08%).[172] The electric-field assisted growth of $MA_3Bi_2I_9$ was also employed by Wang et al. in electrochemical deposition technique, however the reported PCE are still low (0.042%).[173]

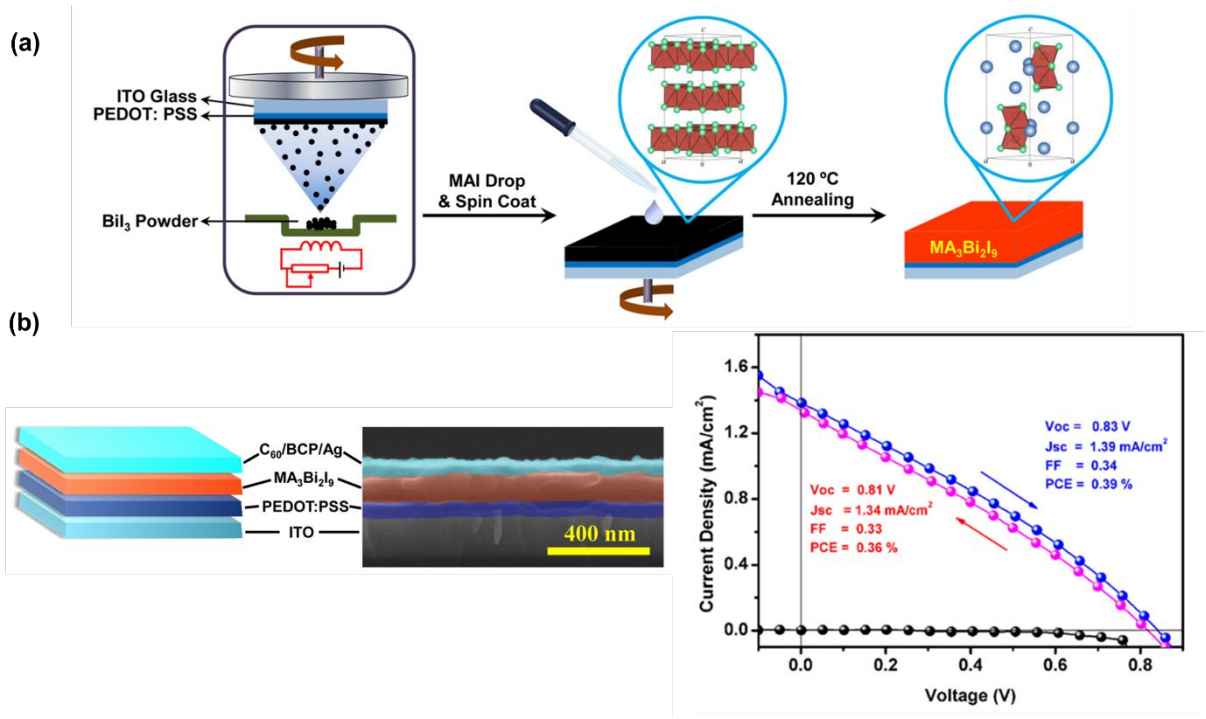

Figure 13: (a) Thermal evaporation and spin-coating combined fabrication of $MA_3Bi_2I_9$ thin films (b) implemented in inverted p-i-n solar cell device structure showing cross-section SEM image with uniform absorber layer and related J-V curves. *Reprinted with permission* .[168] *Copyright 2017, American Chemical Society.*

Although, various techniques were established to engineer the materials properties such as band gap and morphology, the solar cell performance is still far below the lead-based and tin-based perovskites. As metioned in the previous section, the main drawbacks of the $A_3Bi_2I_9$ structure materials beside from wide band gap and problematic morphology are the high exciton binding energy and the formation of possible deep level defects. The 0D structure causes a localization of charge carriers within the isolated dimeric structures being detrimental for efficient charge separation and transport. The need to find more suitable structures is therefore essential and will be discussed in the following sections.

3.3. Other low-dimensional perovskite derived materials

3.3.1. Structure

Since the structural flexibility of perovskites or organic-inorganic metal halides, allows the compositional engineering of each component of the classic ABX_3, any change thereof can lead to a wide variety of new compounds, which deviate from the classic perovskite structure. Bigger A-site cations for instance direct the structural dimensionality of the inorganic framework. As discussed in the previous section the use of the classic small monovalent A-site cations leads to mainly 0D structures with isolated dimeric octahedra (see **3.1.1**). Layered perovskite structures are known in lead based perovskites for larger A-site cations such as aliphatic ammonium cations R-NH_3^+ with preferred <100> orientation of perovskite sheets also known as Ruddlesden-Popper phases.[174] Similar oriented layered lead-free perovskites were discovered by Mitzi using 5,5‴-bis-(aminoethyl)-2,2′:5′,2″:5″,2‴-quaterthiophene (H_2AEQT) in the A-site, where the $(H_2AEQT)Bi_{2/3}I_4$ is built up by $Bi_{2/3}I_4^{2-}$ vacancy ordered perovskite sheets separated by the organic cations (**Figure 14a**).[175]

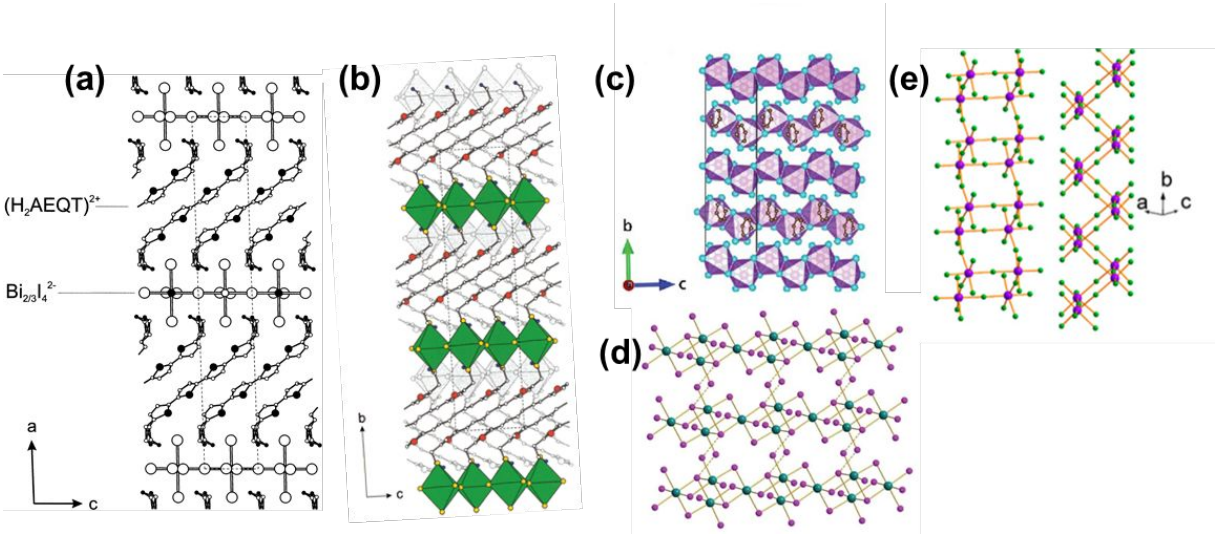

Figure 14: Low dimensional bismuth perovskite-type materials (a) layered vacancy-ordered $(H_2AEQT)Bi_{2/3}I_4$ with $Bi_{2/3}I_4$ chains separated by large organic cation. *Reprinted with permission* [175] *Copyright 2000, American Chemical Society;* (b) $(H_2AETH)BiI_5$ with corner-connecting octahedra chains of the $[BiI_5]^-$ structure motif separated by the organic cation; *Reprinted with permission* [176] *Copyright 2001, American Chemical Society;* (c) BiI_4 anionic chains in $PyrBiI_4$ leading to a pseudo-3D framework. *Reprinted with permission from* [177]

Copyright 2017, The Royal Society of Chemistry; (d) trimeric Bi_3I_{10} polymeric chains in $C_6H_8NBi_3I_{10}$ building up a pseudo-2D framework trough I-I interactions. *Reprinted with permission* [178] *Copyright 2019, The Royal Society of Chemistry;* (e) 1D chains in $(MA_3Bi_2I_9)_n$ polymeric iodobismuthate. *Reprinted with permission* [175] *Copyright 2018, American Chemical Society.*

The $[BiI_4]$ vacancy-free chains of edge-sharing BiI_6 octahedra were found in iminium cation based $(Me_2C{=}NMe_2)Bi_2I_7$ material with similar 2D layered structure.[179] The use of various A-site cations leads to different crystal structures among the bismuth iodide materials e.g. 1,6-bis[5′- (2′′-aminoethyl)-2′-thienyl]hexane to yield $(H_2AETH)BiI_5$ with $[BiI_5^{2-}]$ chains separated by the organic cation via. Van der Waals interactions and H-bonding (**Figure 14b**).[176] Changing the structure of the organic cations from chains to N-containing rings such as pyridinium in $[py][BiI_4]$ (**Figure 14c**) yielded a pseudo-3D structure with the space group $P2_1/c$ caused by H-bonding and anionic BiI_4^- chains with strong I–I and I–C bonding.[177] Moreover, Usoltev et al. reported on polymeric iodobismuthates with $[Bi_3I_{10}]^{4-}$ polymeric chains building up a pseudo-2D framework through strong I–I interactions (**Figure 14d**) and $[BiI_4]^-$ chains for N-methylpyridinium and N-etyhlpyridinium cations, respectively.[178] 1D polymeric chains were also observed in $(MA_3Bi_2Cl_9)_n$ usually obtained by using an excess of HCl or through diffusion reaction in MeOH. The polymeric structure crystallizes in the orthorhombic Pmma space group, in which bridging Cl atoms connect to 1D chains (**Figure 14e**).[180] The dimensionality of the inorganic framework is directed by the choice of A-site cations, the synthesis methods and also the molar ratios of the precursors. Compositions with various other A-site cations were shown to consist of different type of structure motifs including Bi_2I_{10}, Bi_2I_9 or isolated BiI_6 and many more. [181–184]

3.3.2. Optoelectronic properties

The dimensionality of the inorganic framework has an important effect on the optoelectronic properties, which was, for instance, shown by Mitzi et al. for the materials with structural motif of [BiI_5] chains. For example, the exciton peak in the 1,6 diammonium hexane bismuth iodide ($H_2DAHBiI_5$) is red shifted to 554 nm compared to the $MA_3Bi_2I_9$ (494 nm).[176] An indirect optical band gap of 2.05 eV and direct band gap of 2.15 eV was reported for the $H_2DAHBiI_5$ making it attractive for PV applications.[185] Larger band energy dispersions was observed in the $PyBiI_4$ compounds consisting of [BiI_4^-] chains which interact through I–I bonds leading to pseudo-3D framework. The valence band dispersion is mainly caused by σ-bonding between I 5p and Bi 6p resulting in the chain-like structures. H-bonding and van der Waals interactions between the organic cation and the inorganic framework advances the conduction band (CB) dispersion and therefore better charge transport ability with a direct band gap of 1.78 eV. The lack of strong interactions with organic cation e.g., in methyl pyridinium bismuth iodide, showed less effective band dispersion and flat bands .[177] Especially, the I–I interactions between the anionic structures was shown to influence the band gap strongly, where 0D structures exhibited wider band gap than 1D structures (**Figure 15**).[186]

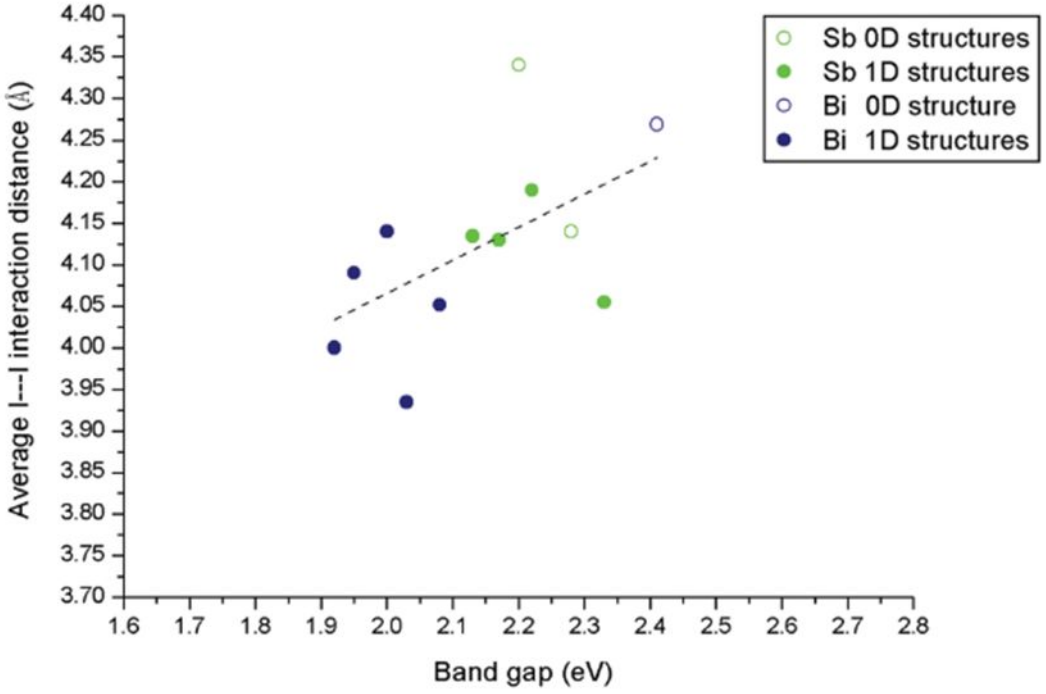

Figure 15: Influence of the connectivity among the inorganic framework in Bi and Sb based materials on the band gap. *Reprinted with permission* [186] *Copyright 2018, The Royal Society of Chemistry.*

3.3.3. Solar cells

The solar cell application of the iodo bismuthates based on the polymeric and chain like structures are limited. The 1,6-hexanediammonium bismuth iodide was investigated as potential solar absorber by several groups manifesting enhanced PL lifetimes[187] compared to 0D $MA_3Bi_2I_9$ and a PCE of 0.027% was reported for solar cells with FTO/c-TiO_2/m-TiO_2/$HDABiI_5$/spiro-OMeTAD/Au device structure.[185] The pseudo-3D $PyrBiI_4$ with a band gap of 1.78 eV implemented in a printable mesoscopic FTO/TiO_2/ZrO_2/C/perovskite solar cell structure achieving a PCE of 0.9% and J_{SC} = 2.71 mA/cm^2. Further, iodo bismuthates based on N-heterocyclic cations with 1D Bi–I chains showed poor efficiencies (~ 0.1%) owing to their anisotropic charge transport, which requires appropriate surface orientation of the 1D chains, as shown in **Figure 16**, and is essential for efficient charge transport. In order to

reduce the band gap and obtain the layered perovskite structure, Johansson et al. investigated new type of cesium bismuth iodide material, $CsBi_3I_{10}$. The $CsBi_3I_{10}$ material thin film showed band gap of 1.7 eV compared to that of $Cs_3Bi_2I_9$. The absorption coefficient for $CsBi_3I_{10}$ also increased by an order of magnitude compared to $Cs_3Bi_2I_9$. The resultant device showed PCE of 0.4% higher than that of $Cs_3Bi_2I_9$.[188] Further Khadka et al. employed solvent vapour annealing to fabricate $Cs_3Bi_2I_9$ and $CsBi_3I_{10}$ thin films and found that $Cs_3Bi_2I_9$ is more stable under annealing conditions and the resultant device based on $Cs_3Bi_2I_9$ showed PCE of 1.26% with NiOx as HTM.[189] While Khadka et al.[189] raised concern on $CsBi_3I_{10}$ material stability, some other reports showed improved device efficiency. For instance, Liang et al. showed that the efficiency of $CsBi_3I_{10}$ can be improved by employing solvent vapor atmosphere and they reported a highest PCE of 1.03%[182] for solution processed solar cells. Efforts were also carried out to deposit $CsBi_3I_{10}$ by thermal evaporation and the resultant device demonstrated PCE of 0.84%.[190]

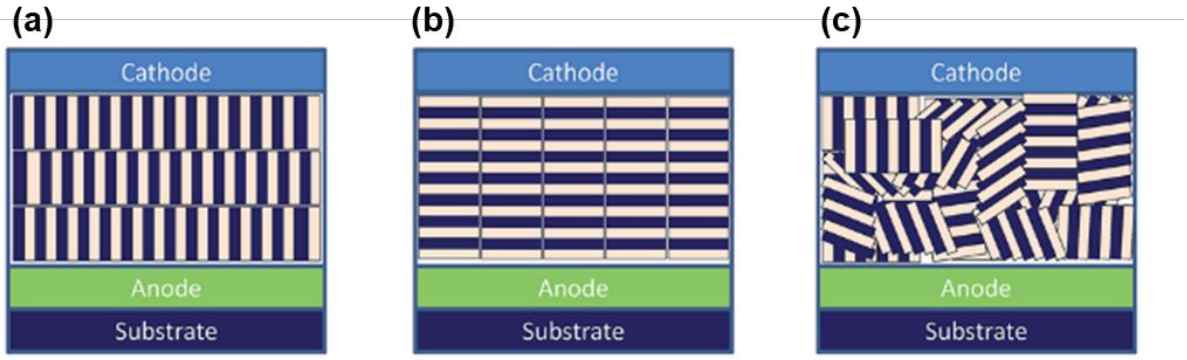

Figure 16: Surface orientation of 1D Bi – I chains (blue sticks); (a) vertical orientation essential for charge transport to the electrodes in the solar cell; (b) horizontal orientation leading to blocking and (c) disordered orientation. *Reprinted with permission* [178] *Copyright 2019, The Royal Society of Chemistry.*

3.4. Three-dimensional double perovskites

3.4.1. Structure and optoelectronic properties

Three-dimensional (3D) lead halide perovskite solar cells have shown remarkable rise in PCE; however, lead perovskite constitutes only a small section of the vast and diverse family of halide perovskite which date back to 1800 – 1900.[191,192] In search of lead-free perovskite materials, researchers have sought to cast a wider net in search of new perovskite compositions that mimic the optoelectronic properties of its lead halide counterparts. This topical review will not address nano-structuring of double perovskites and only discuss on optoelectronic properties and photovoltaic device performance of Bi^{3+} based double perovskites. It is well known that 3D ABX_3 perovskite structures work better as light harvesting material compared to lower dimensional structures because of their exceptional optoelectronic properties. Thus, attempts were made to form a 3D perovskite structure using Bi^{3+} trivalent metal ions. This led to explore the possibilities of heterovalent substitution of Pb^{2+} by combining trivalent Bi^{3+} and monovalent metals such as silver (Ag^+), copper (Cu^+), gold (Au^+) and potassium (K^+) resulting in formation of double perovskite structure possessing a molecular structure of $A_2BB'X_6$ where A is an organic or inorganic cation such as MA^+, Cs^+, B is trivalent metal such as Bi^{3+}, B' is monovalent metal cation such as Ag^+, Cu^+ and X is halide anion. In other words, double perovskites possess a similar structural framework compared to that of a single ABX_3 perovskite while permitting a wider variety of cations to be incorporated into the octahedrally coordinated B/B' site.[193] In this, the double perovskite structure contains cations or vacancies surrounded by six halides ($[BX_6]^{n-}$; B = cation or vacancy and X = halide) and these $[BX_6]^{n-}$ units are corner-sharing octahedral units in a 3D pattern. In this structure, there are exactly two structurally distinguishable $[BX_6]^{n-}$ motifs in the unit cell which together makes chemical formula of $A_2BB'X_6$.[193] The presence of two distinct $[BX_6]^{n-}$ units distinguishes double perovskite from single perovskites as shown

in **Figure 17**. Similar to lead halide perovskites, the band structure of double halide perovskites is mainly determined by B^+, B^{3+} and X-site atoms. As wider variety of cations can be incorporated into the octahedrally coordinated B/B' site, the nature of band gap can be effectively tuned. For instance, the combination of thallium (Tl^+) and Bi^{3+} in $MA_2TlBiBr_6$ exhibits direct nature of band gap whereas replacing Tl^+ with Ag^+ to form $MA_2AgBiBr_6$ makes it indirect in nature.[194,195]

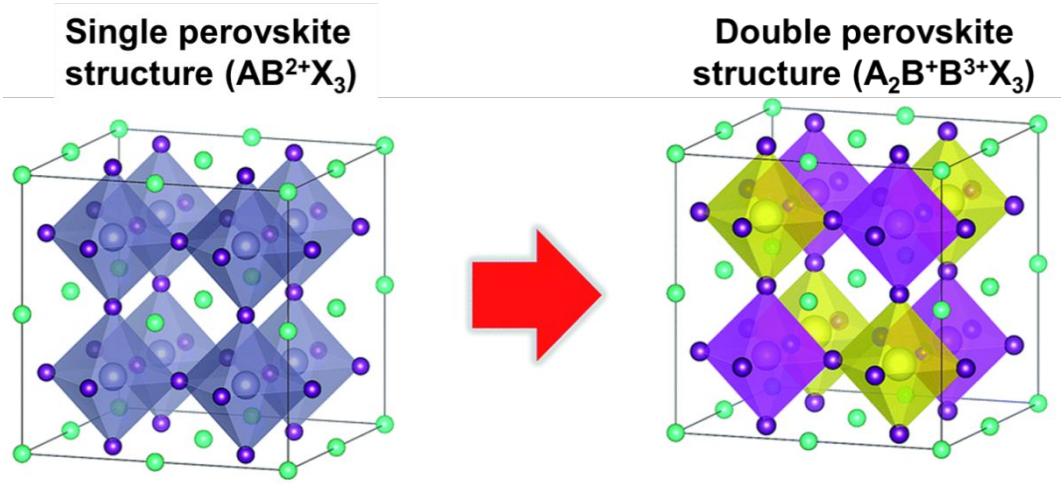

Figure 17: Schematic illustration of B^+/B^{3+} cation substitution from single halide perovskites ($AB^{2+}X_3$) to double halide perovskites ($A_2B^+B^{3+}X_6$). *Reprinted with permission*[196] *Copyright 2019, The Royal Society of Chemistry.*

In comparison to hybrid double perovskites, all-inorganic double perovskites have been investigated earnestly. Firstly, $Cs_2Au^+Au^{3+}Cl_6$ double perovskite was synthesized in 1922,[197] followed by additional studies mainly focusing on exploring the structural aspects of double perovskites. Mixed valency based double perovskites having a generic formula of $Cs_2BAu^{3+}Cl_6$ ($B = Ag^+, Cu^+$) were explored since 1950's.[198,199] More details on the history of double perovskite can be found elsewhere.[193] In light of the obsessive interest in lead halide perovskites[54] and following the vacancy ordered Cs_2SnI_6 double perovskite reports,[200] a

computational report proposed MA_2TlBiI_6 double perovskite as a potential lead-free absorber for photovoltaic application.[201] In 2016, three groups independently reported the synthesis and optoelectronic properties of Cs_2AgBiX_6 ($X = Br^-, Cl^-$) which crystallizes in cubic Fm3m symmetry and shows light absorption at the visible range of the spectrum.[202–204] Since then, many new double perovskite compositions have been synthesized, including $Cs_2AgInCl_6$, $MA_2TlBiBr_6$, $Cs_2AgSbCl_6$, Cs_2AgTlX_6 ($X = Br^-, Cl^-$) to name a few.[194,205–211] Although many double perovskite compositions have been synthesized, Cs_2AgBiX_6 ($X = Br^-, Cl^-$) have been explored earnestly. With the help of diffuse reflectance, Woodward et al.[203] reported band gaps of 2.77 eV and 2.19 eV for $Cs_2AgBiCl_6$ and $Cs_2AgBiBr_6$, respectively. Moreover, band structure calculations revealed that interactions between 3p/4p orbitals of halide ions and Ag 4d orbitals modifies valence band, leading to an indirect bandgap. They further observed that $Cs_2AgBiCl_6$ is stable for several weeks whereas $Cs_2AgBiBr_6$ is not stable. Subsequently, Karunadasa et al.[202] synthesized $Cs_2AgBiBr_6$ single crystal with an indirect bandgap of 1.95 eV and PL lifetime of 660 ns as shown in **Figure 18a**. On the other hand, Snaith and co-workers estimated electron diffusion length of $Cs_2AgBiBr_6$ to be 30 nm which is due to high density of electron traps within the bulk of the material.[212] It is reported that $Cs_2AgBiBr_6$ exists in cubic phase (space group Fm3m) and a low temperature tetragonal phase (space group *I*4/m).[193] Schade et al., with the help of heat capacity and diffraction measurements, determined the presence of structural phase transition at ~122 K.[213] This phase transition dramatically affects the optical properties: the exciton binding energy and the corresponding band gap energy, strongly suggesting that the direct bandgap energy is controlled by the BBr_6 octahedral rotation. In addition to this, the charge carrier lifetimes are also affected by the structural transition possibly associated with tetragonal twin boundaries. In comparison to lead halide perovskites in which the carriers are expected to strongly couple to lattice vibrations, the PL emission in $Cs_2AgBiBr_6$, as demonstrated by Zelewski et al., is strongly influenced by the strong electron-phonon coupling.[214] Further they report that the PL

emission is related to color center rather than band to band transition. Very recently, Herz and co-workers[215] observed rapid decay in terahertz photoconductivity transients that reveal barrier-free, ultrafast localization of free carriers on a time scale of 1.0 ps to an intrinsic small polaronic state. By combining absorption and temperature-dependent PL measurements, they observed that the localized state is intrinsically self-trapped in nature which subsequently diffuses to color center accounting for broad and strongly red-shifted emission. This intuitively suggests that $Cs_2AgBiBr_6$ is not an ideal candidate for optoelectronics that rely on high charge carrier mobilities. However, the self-trapping effects can be tuned by tuning electronic dimensionality and composition, further opening prospects of material design through computational simulations and optoelectronic characterizations. Karunadasa et al. tried to incorporate thallium (Tl) into $Cs_2AgBiBr_6$ which resulted in reduction of bandgap from 2 eV to 1.4 eV[202,210] as shown in **Figure 18b**. Moreover, Tl doped $Cs_2AgBiBr_6$ showed long lived carriers with microsecond lifetimes, suggesting that the photogenerated charge carriers can be effectively extracted in a photovoltaic device. To eliminate the toxicity of thallium and reduce the band gap, Yan et al. alloyed indium (In^{3+}) and antimony (Sb^{3+}) into $Cs_2AgBiBr_6$. It was interesting to observe that $Cs_2Ag(Bi_{1-x}B_x)Br_6$ (B = In^{3+}, Sb^{3+}) can accommodate up to 75% with In^{3+} with increased band gap and up to 37% with Sb^{3+} with reduced band gap.[209] For particular composition of $Cs_2Ag(Bi_{0.625}Sb_{0.375})Br_6$ reduction in band gap up to 1.86 eV was observed. Different atomic configuration of Sb^{3+} and In^{3+}, as revealed by band structure calculations, resulted in opposite band gap shift. Very recently, Schade et al.[216] performed investigation on $Cs_2AgBi_{1-x}In_xBr_6$ and determined that the indium cation shrinks the lattice and shifts the cubic-to-tetragonal phase transition point to lower temperature, thus a more stable cubic phase. With increase in the indium content, the absorption onset is shifted to shorter wavelength resulting in wider band gaps. Despite this, they observed significant enhancement in the steady-state PL intensity.

In fabrication of Cs_2AgBiX_6 double perovskites with large band gap, Br^- and Cl^- halides were used, however, the synthesis of Cs_2AgBiI_6 with a band gap of 1.75 eV has been reported to be feasible in the form of nanocrystals and the details can be found elsewhere. [217] Recently, Ma et al.[218] alloyed sodium (Na^+) with Bi^{3+} to synthesize Cs_2NaBiI_6 double perovskite. Spectroscopic investigations revealed that Cs_2NaBiI_6 possesses a direct band gap of 1.66 eV which is slightly higher than $CH_3NH_3PbI_3$ perovskite and exhibits prolong stability against moisture. Zhang et al. performed a series of investigations to computationally design inorganic double perovskites and identified eleven Bi-based double perovskites with intrinsic thermodynamic stability, suitable band gaps, low exciton binding energies and carrier effective masses.[219–222] Among all the materials explored, Tl^+ and In^+ based double perovskite materials showed direct bandgap of 1.0 eV. However, the high toxicity of Tl^+ and instability of In(I) makes it not suitable for photovoltaic device.

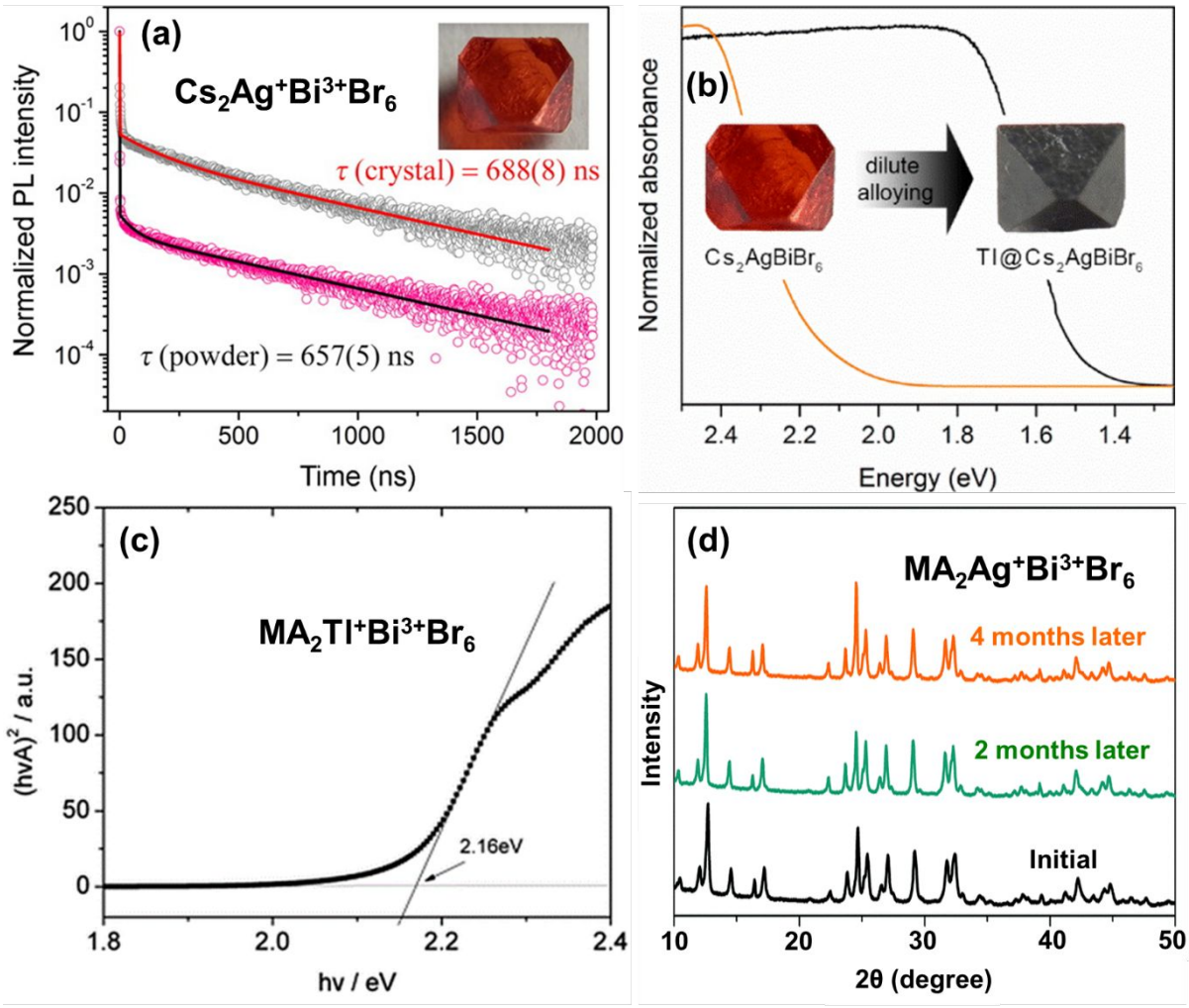

Figure 18: (a) Photoluminescence spectra of $Cs_2AgBiBr_6$ single crystal. *Reprinted with permission.*[202] *Copyright 2016, ACS*, (b) normalized absorbance of $Cs_2AgBiBr_6$ and Tl incorporated $Cs_2AgBiBr_6$. *Reprinted with permission.*[210] *Copyright 2017, ACS*, (c) Tauc plot of $MA_2TlBiBr_6$ showing direct band gap of 2.16 eV. *Reprinted with permission.*[194] *Copyright 2016, The Royal Society of Chemistry;* and (d) XRD pattern of $MA_2AgBiBr_6$ showing stability in ambient atmosphere for 4 months. *Reprinted with permission.*[195] *Copyright 2017, Wiley-VCH.*

In comparison to inorganic double perovskites, only a few reports have shown the synthesis of bismuth-based hybrid double perovskite materials which includes $MA_2TlBiBr_6$, $MA_2AgBiBr_6$, MA_2AgBiI_6, and MA_2KBiCl_6.[194,195,223,224] Among these materials only MA_2KBiCl_6 exhibits indirect and direct band gap of 3.02 and 3.15 eV respectively and the remaining perovskites show band gaps in a range of 1.9 to 2.1 eV.[194] Deng et al. performed DFT screening of MA_2BBiX_6 (B = K^+, Ag^+, Cu^+ and X = Cl^-, Br^-, I^-) and observed that the

band gap is similar to that of $CH_3NH_3PbX_3$ perovskites. Further, they reported that $MA_2TlBiBr_6$, which is isoelectric with $CH_3NH_3PbBr_3$, possess a direct band gap of 2.16 eV as shown in **Figure 18c**.[194] Although $MA_2TlBiBr_6$ showed interesting electronic properties, the toxicity of thallium precludes its application as non-toxic alternative to lead perovskites. Concurrently, the same group synthesized $MA_2AgBiBr_6$ and reported band gap of 1.9 eV. It is noted that the difference in the band gap of $MA_2AgBiBr_6$ varies and is highly dependent on the thin film fabrication method.[224] Previously Woodward et al. observed that $Cs_2AgBiBr_6$ is not stable and degrades when exposed to ambient atmosphere and light.[203] Interestingly, by replacing Cs^+ with MA^+ to form $MA_2AgBiBr_6$, as shown in the XRD pattern in **Figure 18d**, enhances the stability against moisture.[195]

3.4.2. Solar cell application

In comparison to material synthesis and investigating the optoelectronic properties, less attention has been devoted towards employing double perovskite in photovoltaic cell. Firstly, Bein et al. incorporated $Cs_2AgBiBr_6$ into mesoporous device architecture for the first time and the resultant device demonstrated PCE of 2.3% with prolong stability of non-encapsulated device in ambient atmosphere.[225] Subsequently, Wang et al. sandwiched $Cs_2AgBiBr_6$ in planar device architecture with Poly(3-hexylthiophen-2,5-diyl) (P3HT) HTM.[226] To deposit $Cs_2AgBiBr_6$, they employed low-pressure-assisted solution processing technique which resulted in uniform pinhole-free layer and the optimized device showed PCE of 1.44%. By employing anti-solvent dripping step[227] (**Figure 19a**), Wu et al. obtained high-quality $Cs_2AgBiBr_6$ thin film with micron sized grains and when sandwiched in inverted planar heterojunction architecture, the device delivered hysteresis-less PCE of 2.32%. Subsequently, Nazeeruddin and co-workers obtained hysteresis-less performance in n-i-p device architecture by fine-tuning the material deposition parameters and by employing different molecular and polymeric hole transport layers.[228] $Cs_2AgBiBr_6$ thin films were also

obtained by sequential vapor deposition method (**Figure 19b**) which induced crystalline film with high uniformity and the photovoltaic device with planar device architecture showed PCE of 1.37% with prolong stability.[229] Although these reports have shown the double perovskite can be a promising replacement for lead perovskites, Savory et al., reported its limitations owing to large carrier effective masses.[230]

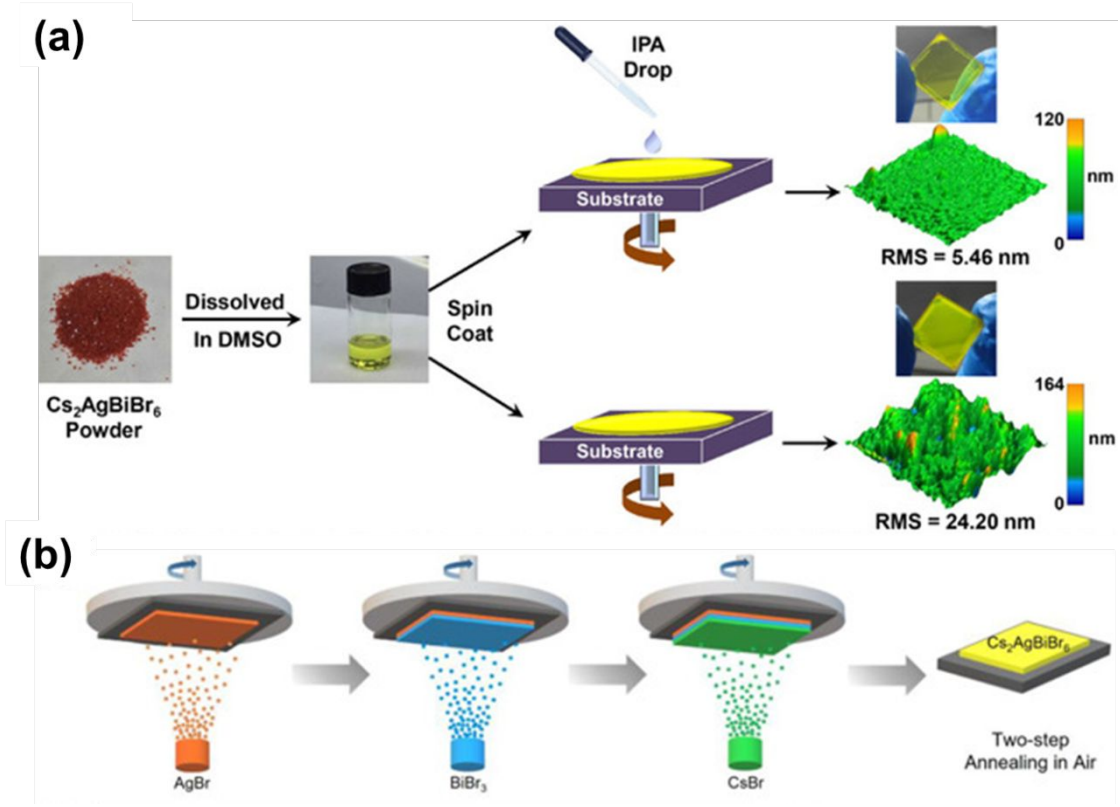

Figure 19: Schematic illustration of $Cs_2AgBiBr_6$ thin film deposition (a) without and with 2-propanol anti-solvent dripping. *Reprinted with permission*[227] *Copyright 2018, Wiley-VCH.* and (b) via sequential vapor deposition. *Reprinted with permission*[229] *Copyright 2018, Wiley-VCH.*

3.5.Silver and copper bismuth iodides

3.5.1. Structure

Silver bismuth iodides were initially attracted interest due to their possible high ionic conductivity being interesting for solid-state electrolytes or battery applications. First investigations on the Ag-Bi-I system were made by Fourcroy et al.[231] and Dzeranova et al.[232] discovering the related phase diagrams, where two new phases Ag_2BiI_5 and $AgBi_2I_7$ were found by the first group and Ag_3BiI_6 and $AgBiI_4$ were found by the latter. Oldag et al. reported on the synthesis of $AgBiI_4$ and Ag_3BiI_6 via solvothermal reaction from AgI and BiI_3 in HI solutions at mild temperatures of 160 °C. $AgBiI_4$ was described to crystallize in a cubic phase in the space group Fd-3$\bar{3}$m with edge-sharing octahedra occupied by Ag or Bi with a 3D network (**Figure 20a,** left). Similarly, $CuBiI_4$ was also reported in the same cubic crystal structure with similar space group.[233] The Ag_3BiI_6 was shown in the space group Rm with partial occupancy of Ag (2/3) and Bi (1/3). Both compounds showed mobility of Ag^+ ions for which an activation energy of 0.44 eV was determined.[234] Later, Sansom et al. revealed further possible crystal structure for the $AgBiI_4$ compound being a cubic-layered structure of $CdCl_2$-type (**Figure 20a**, right). In contrast to these findings, Mashadieva et al. elaborated the phase equilibria in the Ag-Bi-I system, in which they claimed the non-existence of the $AgBiI_4$ and Ag_3BiI_6 phases, which were shown rather as mixtures of Ag_2BiI_5 + $AgBi_2I_7$ and AgI + Ag_2BiI_5, respectively.[235] Similar observations were made by Jung et al. and Hosseini et al. who showed the non-existence of $AgBiI_4$, rather Ag_2BiI_5 was formed preferably when various compositions were used.[236,237] Sargent and coworkers, firstly demonstrated the synthesis of $AgBi_2I_7$ thin films from hot n-butylamine solution crystallizing in a cubic $ThZr_2H_7$-type structure with the space group Fd-$\bar{3}$m (**Figure 20b**), which was highly sensitive to temperature and AgI/BiI_3 ratio. For instance, they observed appearance of a doublet peak (at $2\theta = 42°$) in the XRD pattern when a ratio of 1:1 or 2:1 was used, belonging to the Ag_2BiI_5

phase or BiI_3 and AgI peaks if the annealing temperature was below 150 °C.[238] In contrast, with the help of density functional theory (DFT) calculations and molecular dynamics simulations, Yan and co-workers observed a Ag-deficient $AgBiI_4$ structure with an octahedral iodide coordination of Bi is formed instead of previously reported hexahedral coordination with untypically short Bi–I bonds (265 pm).[239]

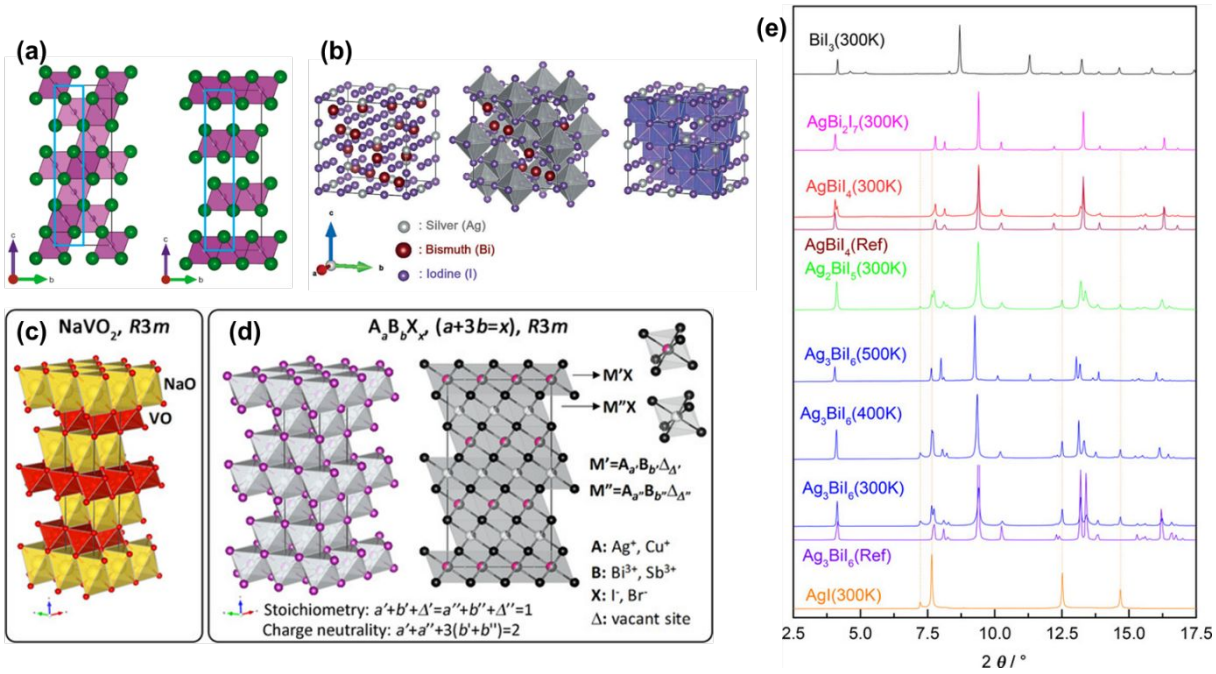

Figure 20: Structures of the Ag-Bi-I ternary system; (a) Possible crystal structures of $AgBiI_4$ described as cubic defect-spinel structure (left) or $CdCl_2$ structure (right). *Reprinted with permission* [240] *Copyright 2017, American Chemical Society;* (b) Reported $AgBi_2I_7$ cubic crystal structure ($ThZr_2H_7$-type with the space group Fd-3m) showing AgI_6 octahedra and BiI_8 hexagons which are corner-connected. *Reprinted with permission* [238] *Copyright 2016, Wiley-VCH;* (c) $NaVO_2$ discovered by Walter Rüdorff, (d) General structure of the Ag-Bi-I ternary compounds with $A_aB_bX_x$ (a + 3b = x) structure similar to $NaVO_2$, introduced as rudorffites by Turkevych et al; (e) Synchroton XRD pattern of all rudorffite crystals grown from melt. *Reprinted with permission* [241] *Copyright 2017, Wiley-VCH.*

Turkevych et al. introduced the name rudorffite for the Ag-Bi-I ternary system due to the general similarity to the $NaVO_2$ structure discovered by Walter Rüdorff. Here the ternary system is represented with the chemical formula $A_aB_bX_x$ (x = a + 3b), where A = Ag^+ or Cu^+, B = Sb^{3+} or Bi^{3+} and X = I^- or Br^-. The rudorffites form a 3D network with the R3m space group consisting of altering AgI and BiI edge-sharing octahedral layers. The cation sites can be differently occupied by Ag, Bi and vacancies maintaining the stoichiometry and charge neutrality rules as shown in **Figure 20d**. Furthermore, Ag_3BiI_6, $AgBiI_4$, Ag_2BiI_5 and $AgBi_2I_7$ was synthesized by melt solidification and investigated by synchrotron XRD (**Figure 20e**), revealing that phase pure $AgBiI_4$ and $AgBi_2I_7$ exists at room temperature, whereas Ag_3BiI_6 and Ag_2BiI_5 co-exist with AgI. High temperature XRD revealed that Ag_3BiI_6 exist in a single phase at 500 K.[241] The AgI phase impurity in the Ag_3BiI_6 thin films fabricated through co-sputtering of Ag and Bi and iodization, was also confirmed by Crovetto et al.[242] It is noticeable that, the structure determination of the rudorffite family is not yet well defined as there are discrepancies among the mentioned reports. The discrepancies also continue in the elaboration of the optoelectronic properties as described below.

3.5.2. Optoelectronic properties

The rudorffite compounds show band gap energies below 2.0 eV, precisely, 1.73 – 1.80 eV for $AgBiI_4$[240,243], 1.85 eV for Ag_2BiI_5[243], 1.87 eV for $AgBi_2I_7$[238], 1.83 eV for Ag_3BiI_6.[241] Kim et al. employed ultraviolet photoelectron spectroscopy (UPS) to determine the valence band of $AgBi_2I_7$ which is at 6.2 eV below E_{vac} and is deeper than the VB in $MA_3Bi_2I_9$ (-5.9 eV).[244] **Figure 21** depicts the energy band levels of each composition compared to $MA_3Bi_2I_9$. Sansom et al. reported absorption coefficients for $AgBiI_4$ to be in the range of 10^5–10^6 cm^{-1} comparable to lead perovskites and the VB mainly consist of I 5p and Ag 4d while CB consists of Bi 6p and I 5p orbitals, which was similarly presented for $AgBi_2I_7$.[240,245] A broad PL emission at 720 nm was observed in Ag_3BiI_6 thin films with

lifetimes between 1 to 200 ns.[241,242] In contrast to this, Seo et al. reported a PL emission at 649 nm, where the intensity was dependent on the annealing temperatures with highest intensity for a thin-film annealing process at 180 °C.[246] Ghosh et al. investigated $AgBiI_4$ and Ag_2BiI_5 and reported direct band gaps of 2.37 eV and 2.2 eV along with exciton binding energies of 260 meV and 150 meV, respectively. Excited state carrier lifetimes were found to be 75 ns and 133 ns for $AgBiI_4$ and Ag_2BiI_5 thin films processed via dynamic hot casting method.[247] In case of $CuBiI_4$ two different band gaps were reported, namely 1.8 eV for thin films prepared via direct metal surface elemental reaction, in which first a Cu-Bi bilayer is sputtered and exposed to I_2 vapor, as demonstrated by Yu et al.[248] and 2.67 eV for solution processed thin film by Hu et al.[249] The VB and CB reported by Yu et al. lies deeper and is depicted in **Figure 21**.

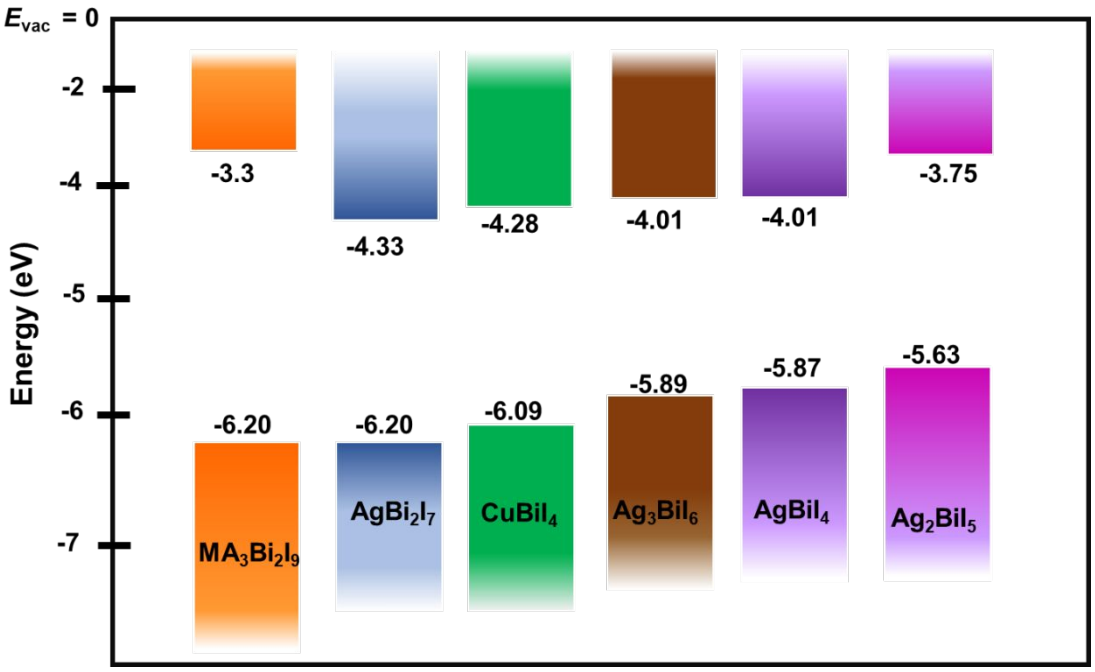

Figure 215: Energy band level diagram for the rudorffites $AgBi_2I_7$[238], $CuBiI_4$[248], Ag_3BiI_6[246], $AgBiI_4$[250], Ag_2BiI_5[236] and $MA_3Bi_2I_9$[126] for comparison. The VB levels are determined from UV photoelectron spectroscopy (UPS) measurements, and the CB levels were determined by the addition of band gaps to the VB level. Band gaps were determined from UV-vis absorption measurements.

Band gap tunability was shown for $AgBi_2I_7$ by mixing I^-/Br^- showing increment in the band gaps for higher bromide substitution and color change from dark brown to yellow as shown in **Figure 22a**. It was shown that Br 4p states contribute to the VB and CB edges and thus influence the band gap energy, while not changing the crystal structure for amounts lower than 20%. Higher amounts lead to AgI and $BiBr_3$ impurities because of the instability of the pure bromide based compound.[245] In order to reduce the band gap and raise the valence band level, Pai et al. used sulfur doping into the rudorffite materials to obtain $A_aB_bI_{a+3b-2x}S_x$ employing bismuth tris(4-metyhlbenzodithitoate) along with BiI_3 and AgI precursors. Generally, band gap narrowing was observed for all compositions and an uplift of the VBs was shown, leading to better alignment with hole transport materials' HOMO levels (**Figure 22b**).[251] Moreover, Bi/Sb alloying also showed significant changes in the band gap and band structures, where it was found that I 5p and Sb 5d interaction is slightly stronger compared to Bi 6d states leading to a splitting of I 5p peaks in DOS as shown in **Figure 22c**.[252] Copper (Cu)-doping in Ag_2BiI_5 was shown to enhance the light absorption in the range of 400-700 nm due to additional Cu 3d states at the top of the VB and better overlap with CB.[253] Band level upshifting was also achieved by cesium incorporation to the $AgBiI_4$ compound yielding $Cs_xAg_{1-x}BiI_4$.[254] Very recently, Sansom et al.[255] synthesized Cu_2AgBiI_6 material which showed absorption coefficient of 1 x 10^5 cm^{-1} near the absorption onset, several times higher than that of $CH_3NH_3PbI_3$ perovskite (0.3 x 10^5 cm^{-1}). Moreover, this material possesses direct band gap with exciton binding energy of 25 meV, charge carrier mobility of 1.7 cm^2 $V^{-1}s^{-1}$, long PL lifetime of 33 ns and a relatively small Stokes shift between absorption and emission. Interestingly, the structure of Cu_2AgBiI_6 includes both tetrahedral and octahedral species. The octahedral sites are occupied by Bi^{3+} and Ag^+ while Cu^+ occupies all tetrahedral sites located in cubic closed-pack iodide sublattice. The presence

of octahedral and tetrahedral species further opens up the possibility largely for tuning compositional and chemical substitution.

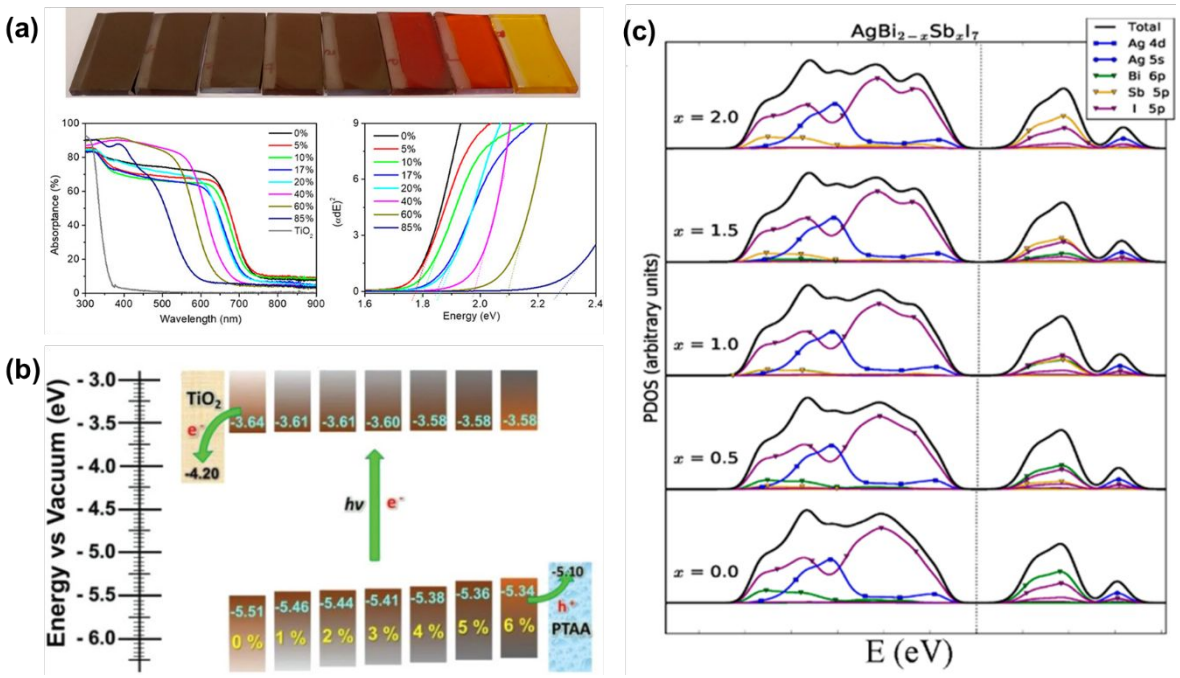

Figure 22: Tunability of optoelectronic properties of rudorffites; (a) Bromide substitution in $AgBi_2I_7$ leading to color change, band gap tuning while maintaining the cubic crystal structure (Fd3m group). *Reprinted with permission* [245] *Copyright 2019, American Chemical Society;* (b) Sulfur-doping of Ag_3BiI_6 showing band gap narrowing and VB up-shifting. *Reprinted with permission* [251] *Copyright 2018, Wiley-VCH;* (c) Sb/Bi alloying leading to changes in the band structure, I 5 p shows splitting for higher Sb amount. *Reprinted with permission* [252] *Copyright 2020, American Chemical Society.*

3.5.3. Solar cell applications

The first solar cell application with silver bismuth rudorffites was made by Sargent and co-workers, fabricating $AgBi_2I_7$ thin film based solar cells *via* solution processing.

Because AgI is poorly soluble in common organic solvents, n-butylamine was used as solvent. The obtained solution was spin-coated on mesoporous TiO_2 coated FTO substrates and annealed at different temperatures whereby 150 °C showed a smooth and pin-hole free morphology with grain sizes ranging from 200 to 800 nm. Solar cells yielded a PCE of 1.22% in a regular n-i-p stack with poly(3-hexylthiophen-2,5-diyl) (P3HT) as HTM.[238] However, this efficiency was not reported in subsequent studies. For instance, Zhu et al. investigated the photovoltaic properties of Ag_2BiI_5 and $AgBi_2I_7$ using similar fabrication technique with n-butylamine as a solvent and annealing temperature. They obtained a superior PV performance (2.1%) and EQE for Ag_2BiI_5 whereas only 0.4% PCE was achieved for $AgBi_2I_7$ in the regular mesoporous stack with P3HT as HTM. The champion solar cells maintained their PCE up to 40 days stored under N_2 in dark.[243] Although, the exact reason for such non-reproducible results has not been investigated, Mitzi and co-workers reported change in composition of $AgBi_2I_7$ to $Ag_{1.16}Bi_{1.04}I_{4.00}$ after annealing the thin-film at 150 °C.[256] To avoid such compositional changes due to annealing at high temperature, the same group employed dual-source evaporation method to obtain silver-bismuth halide materials. The planar configuration device employing silver bismuth iodide showed V_{OC} of 0.8V, however, the device showed efficiency of 0.89%.[257] In order to improve the efficiency, later, we investigated the formation of solvate intermediates in n-butylamine and DMSO solvents and studied their influence on the materials' structural and optoelectronic properties.[258] Using DMSO, we were able to fabricate $AgBi_2I_7$ thin films at relatively lower temperature (100 °C), as shown in **Figure 23a and b**, compared to n-butylamine (150 °C) due to weaker coordination strength of the former. We obtained a PCE of 2.1% (vs. 0.4%) in a regular solar cell structure with P3HT as HTM (**Figure 23c**) with prolonged stability for 75 days in ambient atmosphere with a relative humidity of 50% as shown in **Figure 23d**. Interestingly, it is found that remnant BiI_3, which appears due to weak solvent-intermediate complex and low concentration of the precursor materials, plays an important role in enhancing the efficiency and stability. This can

be due to the efficient charge transport, influenced by BiI_3, at the interface of $AgBi_2I_7$ and dopant free HTL.[258] Inclusion of lithium bis(trifluoromethylsulfonyl)-imide (Li-TFSI) additives in the $AgBiI_4$ precursor solution, as demonstrated by Zhang et al., leads to superior V_{OC} of 0.83 V owing to the coordination to the $TFSI^-$.[259] First solar cells based on the Ag-rich Ag_3BiI_6 composition was reported by Turkevych et al. with a decent PCE of 4.3% in the regular mesoporous solar cell structure with poly[bis(4-phenyl)(2,4,6-trimethylphenyl)amine (PTAA) as HTM.[241] In an extended study, Baranwal et al., showed the solar cell application of various Ag-rich bismuth-based materials including Ag_3BiI_6, $Ag_3BiI_3(SCN)_3$ and Cu_3BiI_6, where the crystal structure of the last two was not identified. The materials were implanted in regular FTO/TiO_2/absorber/spiro-OMeTAD/Au and in inverted FTO/NiO/absorber/PCBM/BCP/Ag solar cell structures via solution processing. Best PCEs were obtained from the regular solar cell architectures with 0.91% for Ag_3BiI_6, 0.14% for $Ag_3BiI_3(SCN)_3$ and 0.19% for Cu_3BiI_6.[260] The low PCE compared to previous report could be due to the use of spiro-OMeTAD as HTM. Hu et al. demonstrated $CuBiI_4$ in solar cell application manifesting a cubic crystal structure in the Fd-3m space group. The thin films were prepared from HI-assisted dimethylacetamide solution and deposited *via* solvent vapor annealing process. The solar cells achieved a PCE of 0.82% with a long-term stability up to 1008 h under ambient conditions.[249] A PCE enhancement for $CuBiI_4$ solar cells was achieved by employing the direct metal surface elemental reaction coupled with vapor treatment. Here a induced Bi gradient throughout the solar cell lead to efficient charge transport yielding a PCE of 1.1%.[248]

In order to boost the rudorffite solar cell performance several techniques were employed to improve the crystallinity and thin film morphology, for instance Mathews and co-worker introduced dynamic hot casting technique which led to large grains in both $AgBiI_4$ and Ag_2BiI_5 thin films and thus enhanced excited state carrier lifetimes and PCE (>2%).[247]

Furthermore, the solution concentration and composition was showed to be important for the thin film quality along with annealing temperature.[236,250] Several other preparation techniques were introduced to fabricate rudorffite based solar cells such as microwave-assisted annealing[237], dual-source evaporation[257] and dynamic spin-coating with ramped annealing.[246] Additionally, PTAA was found to be more suitable compared to P3HT in $AgBiI_4$ solar cells due to lower HOMO level (-5.14 eV for PTAA vs. -4.94 eV for P3HT) fitting better to the VB of the $AgBiI_4$ (-5.87 eV) (**Figure 23e**).[250] Band gap tuning approaches could lead to changes in the optoelectronic properties (**see section 3.5.2.**), among all reported techniques such as use of Br^-[245,261], Cu-[253], Sb-[252], Cs-[262] alloying, doping with reduced graphene oxide and multi-walled carbon nanotubes,[263] sulfur-doping was demonstrated as a most successful strategy to narrow the band gap and upshift the VB levels, which lead to the highest PCE of 5.44% reported so far for $Ag_3BiI_{5.92}S_{0.04}$ rudorffite based solar cells. The best performing $Ag_3BiI_{5.92}S_{0.04}$ solar cells were fabricated from solution using an HI additive and gas-quenching method, and maintained 90% of the initial PCE after 45 days under ambient conditions.[251] Recently, new compositions were discovered for the use in solar cells: $AgBi_3I_{10}$ having a trigonal structure with the space group R-$\bar{3}$m and a band gap of 1.8 eV. The carbon electrode based regular solar cell yielded a PCE of 2.73%.[264] Synthesis and investigation of photovoltaic performance of Cu_2AgBiI_6 material (an analogy to Ag_3BiI_6) in regular device architecture, as demonstrated by Sansom et al., showed PCE of 0.43%.[255]

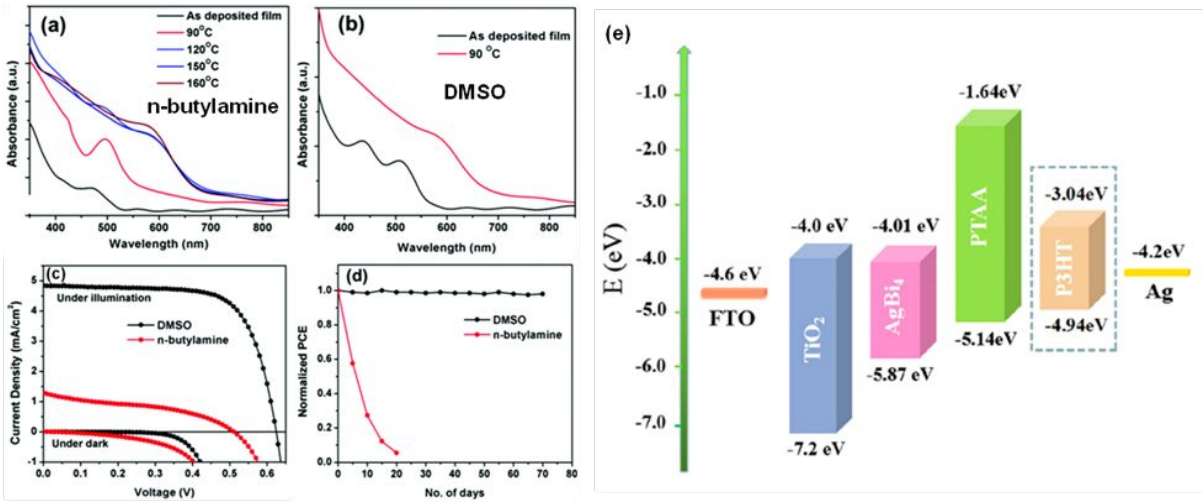

Figure 23: (a – b) UV-vis absorption spectra of $AgBi_2I_7$ thin film without and with annealing at various temperatures. (c – d) J-V characteristic curves of best performing devices processed with n-butylamine and DMSO and their stability in ambient atmosphere.[258] *Copyright 2018, RSC;* (e) Energy level diagram of the regular $AgBiI_4$ based solar cell with energy levels of PTAA and P3HT in comparison. *Reprinted with permission* [250] *Copyright 2018, American Chemical Society.*

Among various explored silver bismuth halide materials, Ag_3BiI_6 based solar cells showed high PCE of 4.3%.[241] Despite a decent initial efficiency and pure inorganic material, very recently, we showed that Ag_3BiI_6 device performance degrades when exposed to ambient humidity atmosphere. This degradation was influenced by unique triple-ion migration phenomenon where Ag^+, Bi^{3+} and I^- ions migrate and diffuse through hole transport material and decomposes the gold metal electrode (**Figure 24a**).[265] Interestingly this degradation was observed only in Ag-rich material, that is, Ag_3BiI_6 and other silver bismuth iodide materials such as $AgBi_2I_7$ and Ag_2BiI_5 showed stable performance under ambient atmosphere as shown in **Figure 24b**. Moreover, the performance degradation was more pronouncedly observed in the case of anti-solvent based Ag_3BiI_6 device compared to the case of without anti-solvent one attributing to presence of residual AgI (phase impurity) and voids at the interface with mesoporous TiO_2 ETL.[265] This further indicates that a better understanding of Ag_3BiI_6

material is necessary for better solar cell design and to stimulate the use of unique triple-ion migration phenomenon is other optoelectronic devices such as photodetectors and memory devices.

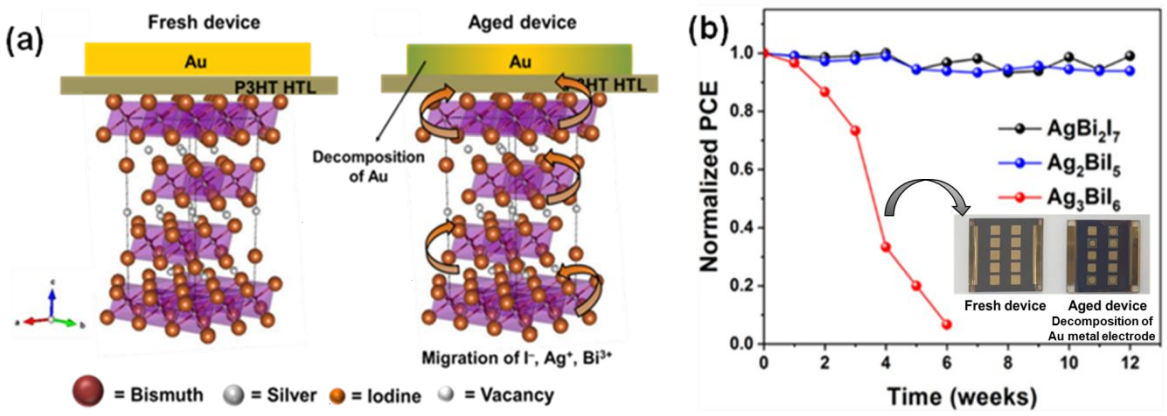

Figure 24: (a) Schematic illustration of migration of Ag^{+}, Bi^{3+} and I^{-} ions in Ag_3BiI_6 solar cells and (b) normalized PCE plot showing stable performance in $AgBi_2I_7$ and Ag_2BiI_5 solar cells contrasting Ag_3BiI_6 solar cells. *Reprint with permission*[265], *Copyright 2021, Wiley-VCH.*

3.6. Two-dimensional layered Bismuth iodide

3.6.1. Structure and optoelectronic properties

Bismuth iodide (BiI_3) crystallizes in the $R\bar{3}$ space group and adopts a layered 2D structure formed by BiI_6 octahedra (**Figure 25a**) with 2/3 of the octahedral voids occupied by the metal cation (**Figure 25b**). The s lone pairs are not active, whereas the 6p electrons are transferred to the I atoms, leading to ionic Bi-I bonds (**Figure 25c**).[266,267] These Bi-I layers are held together by Van der Waals forces, which makes the 2D material soft and easy to cleave along the [001] direction.[268]

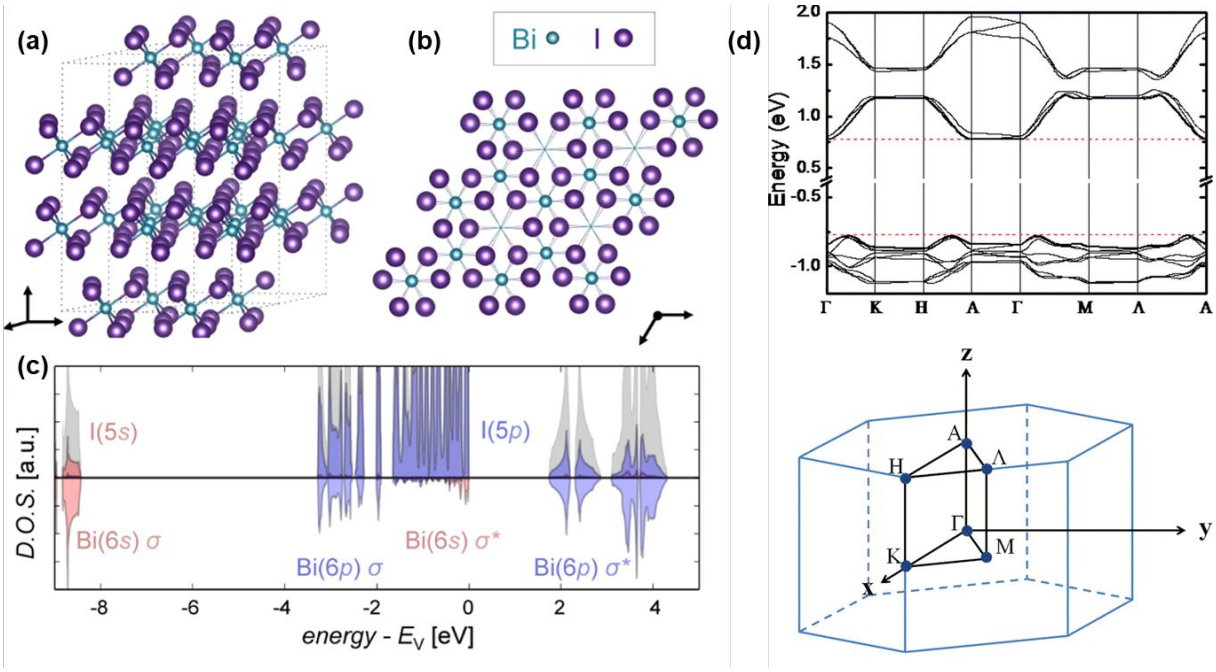

Figure 25: (a) Extended unit cell of BiI_3 showing the connected BiI_6 octahedra; (b) A single layer of the vacancy ordered crystal structure with 1/3 cation vacancies; (c) Partial DOS of BiI_3 showing the contribution of the atom orbitals. *Reprinted with permission* [267] *Copyright 2015, American Chemical Society;* (d) Electronic band structure of BiI_3 (top) and the related Brillouin zone (bottom). *Reprinted with permission* [269] *Copyright 2013, AIP Publishing.*

The electronic structure of BiI_3 was reported to resemble with that of $MAPbI_3$ due to the contribution of the Bi 6s electrons into the VB.[267] The CB is flat between A and Γ connecting along the z direction and corresponding along the Van der Waals interaction between the layers. The VB is more disperse and the maximum is found between A and M corresponding to the x-y plane and thus within the Bi-I layer (**Figure 25d**). Although band gap values from 1.67 – 2.029 eV have been reported, Pedroza et al. explained that these discrepancies are caused by the sensitivity of the employed techniques such as UV-Vis measurement or ellipsometry and the consideration of spin-orbit coupling in DFT calculations. The authors confirm an indirect band gap of 1.67 eV from experimental methods and 1.55 eV (incl. spin-orbit coupling) from DFT calculations.[269] The PL emission was observed at 1.76 and 1.83 eV (excitation at 532 nm) dependent on material's morphology. PL

lifetimes of 190-240 ps and 180-230 ps were observed for solution and physical vapor deposited thin films, respectively.[267] Ma et al. conducted DFT investigations of single layer BiI_3 nanosheets as possible 2D material. The monolayer was shown to have a band gap of 1.57 eV and comparable cleavage energy to graphite ($E_{cl,BiI3}$ = 0.43 J/m^2 vs. $E_{cl,graphite}$ = 0.37 J/m^2). Furthermore a coupling with graphene showed enhanced light absorption which might be interesting for optoelectronic and photovoltaic applications.[270] Moreover, interesting optoelectronic properties electron diffusion length of 4.9 μm, large static dielectric constant etc. endorse its promising application in optoelectronic devices.[271–273] Due to the outer-shell electronic configuration of 6s^2, which leads to disperse valence band, high dielectric constant, and shallow intrinsic point defects; all of which are serviceable properties of defect tolerant material,[271] BiI_3 can be one of the promising materials for photovoltaic device application.

3.6.2. Solar cells

First solar cell application of BiI_3 was found in the use as HTM in organic solar cells with P3HT:PCBM as absorber showing enhanced efficiency.[268] However, BiI_3 was also considered as a possible solar absorber owing to its suitable band gap. For example, Lehner et al. reported on solution processed BiI_3 thin films in a regular n-i-p FTO/TiO_2/absorber/HTL/Au stack. The thin films were produced from tetrahydrofuran (THF) solution with HI additive via spin-coating and showed a PCE of 0.32%. The quite low performance was attributed to the deep VB level (-6.1 eV) compared to $MAPbI_3$ (-5.4 eV) and therefore a more aligned HTL was suggested to improve the charge carrier transport.[266] Hamdeh et al. introduced the solvent vapor annealing process in the fabrication of BiI_3 solar cells leading to enlarged grain sizes and crystallinity with preferred growth orientation. The use of THF or DMF as solvent improved the solubility of BiI_3 due to the formation of solvate-adducts, and the solvent vapor annealed thin films in the FTO/TiO_2/BiI_3/V_2O_5/Au solar cell

structure yield a PCE of 1% (**Figure 26a**). The solar cells were stable under air and surface oxidation to BiOI showed improved PV performance due the hole extraction properties of BiOI (**Figure 26a**).[274] In further studies, the solvent vapor annealing was shown to be important for the grain morphology of BiI_3 and to retard the rapid crystallization in order to avoid kinetically constrained grain growth.[275] Temperature and humidity was shown to significantly influence the grain growth due to the direct impact on the formation of solvate-adduct (BiI_3-DMF complexes).[276] Tiwari et al. could achieve higher V_{OC} = 0.6 V and PCE of 1.2% by synthesizing BiI_3 thin films from iodination of Bi_2S_3 thin films.[277] Moreover, interface engineering studies show better PV performance owing to the reduced recombination losses at the interface for example by using a $NbSe_x$ interfacial layer allowing better exciton separation at the interfaces.[278] Best solar cell efficiency was achieved in BiI_3/PCBM quasi-bulk heterojunction solar cells yielding a PCE of 1.5% and record J_{SC} of 8.76 mA/cm^2 due to better exciton separation at the BiI_3/PCBM interface.[279]

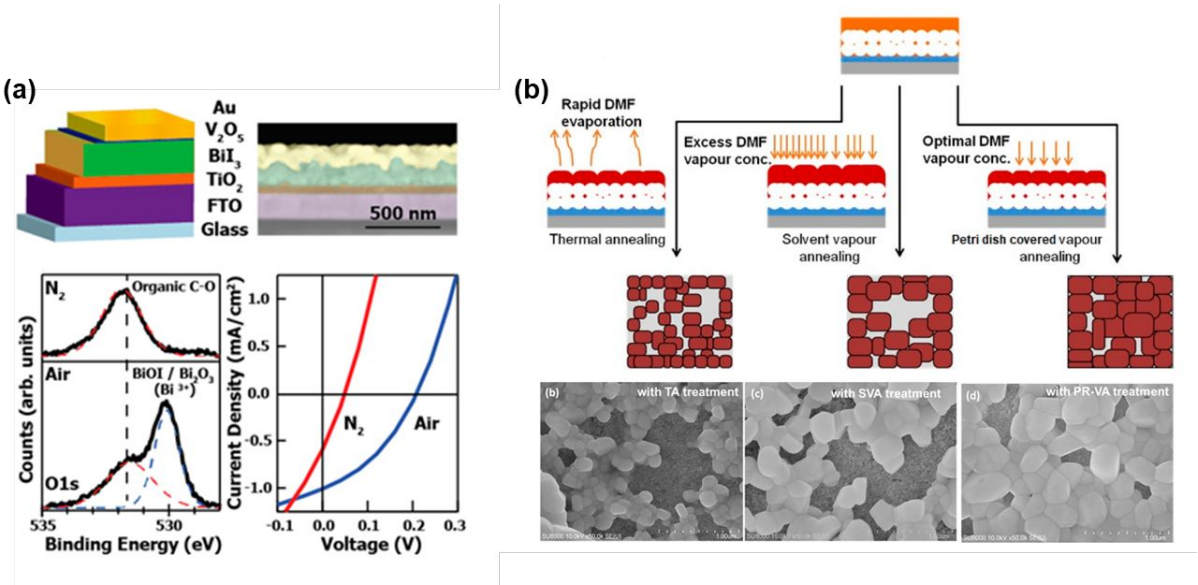

Figure 26: (a) BiI_3 solar cells with all-inorganic FTO/TiO_2/BiI_3/V_2O_5/structure (top), XPS spectra of the thin films fabricated in glovebox and under air showing surface oxidation under air leading to better current densities (bottom). *Reprinted with permission* [274] *Copyright 2016, American Chemical Society;* (b) The influence of solvent vapor annealing techniques on

the grain morphology. *Reprinted with permission* [275] *Copyright 2018, American Chemical Society*.

4. Conclusions and outlook

Although the power conversion efficiency (PCE) of lead halide perovskite solar cells showed rapid rise within a short span of time and is still increasing to approach Shockley-Queisser (S-Q) limit, the stability and lead toxicity are major hurdles in a way to commercialization. Ensuring enhanced material and device stability is important for commercialization than pushing the PCE to S-Q limit. Intrinsic structural instability of the perovskite material is one of the most critical factors that limits the long-term operation of perovskite solar cells. For instance, $MAPbI_3$ which is a widely studied perovskite material has a distorted cubic structure which causes weak interaction of organic A-site cation with the inorganic sublattice and is, in addition to hygroscopic and volatile nature of MA^+ cation, responsible for easy degradation of lead halide perovskite materials under moisture, thermal, oxygen and light.[24,48,280–282] This releases lead iodide as a degraded byproduct which is harmful to the human environment.[56]

Efforts has been carried out to replace lead with tin (Sn^{2+}), germanium (Ge^{2+}), copper (Cu^{2+}), titanium (Ti^{4+}), antimony (Sb^{3+}) and bismuth (Bi^{3+}). However, the uncontrolled crystallization and rapid oxidation of Sn-, Ge- and Cu-based perovskite and thermodynamic instability of TI^{4+} based perovskites appear to be daunting challenges restricting the utilization of actual potential of these materials. The $MAPbI_3$ has 3D structure owing to +2 oxidation state of central metal atom and replacing Pb (in $MAPbI_3$) with Bi, which has a stable oxidation state of +3, forms $MA_3Bi_2I_9$ lower dimensional structure.[24,39,132] By incorporating monovalent cation such as silver (Ag^+), copper (Cu^+) in combination with Bi^{3+} forms a halide double perovskite which yields overall charge balance as the conventional lead halide perovskite. Replacement of A-site cations (MA^+, Cs^+) with transition metals such as Ag^+ or

Cu^+ results in the formation interesting class of halide materials having a three-dimensional (3D) edge-sharing octahedral network. These bismuth-based perovskite and lower and higher-dimensional perovskite-inspired materials show promising stability against moisture, heat, light and oxygen, thus gaining wide attention. Moreover, comprehension of literature suggests that lead halide perovskite single crystal remains stable without showing any sign of degradation up to several years whereas the thin film degrades within a few weeks of exposure to ambient stability.[283,284][285] This indicates that in lead-halide perovskite the phases or crystal orientation determines the stability.[286] On the other hand, various bismuth-based perovskite and perovskite-inspired materials obtained from solid-state mixing of precursor materials or single crystals and solution process spin coating method show similar stability under ambient atmosphere.[135] This strongly suggests that bismuth-based materials are highly stable compared to lead halide perovskites. However, the resultant photovoltaic devices, as summarized in **Figure 3**, currently show lower PCE than their lead counterparts. The S-Q limit for single junction solar cells using an absorber layer with a band gap of 1.78 eV (for silver bismuth iodides and bismuth triiodide) and 2.2 eV (for lower-dimensional bismuth halide materials and double perovskite) can be calculated to 26.86% and 20.5% with J_{SC} = 19.65 mA/cm^2 and 12.48 mA/cm^2, V_{OC} = 1.5 V and 1.75 V, and FF = 91.4 and 92.5% respectively. [287] This, compared to **Figure 3** which is a present status, indicates a large room for enhancing the efficiency of bismuth-based perovskite and perovskite-inspired materials. If the progress is tracked form the beginning to the present time, it can be rationalized that the research track of bismuth based solar cells are in their infancy (first efficiency for bismuth based solar cells[129] was reported in 2015). Comprehension of literature suggests many challenges that need to be addressed to improve the performance of bismuth based a solar cell which includes:

1. PCE of bismuth-based materials with $A_3Bi_2X_9$ (A = MA^+, Cs^+; X = I^-, Cl^-, Br^-) and $A_2B'BiX_6$ (B' = Ag^+, Cu^+) structures has been limited due to wide band gap, high exciton binding energy, to name few. Theoretically many lower and higher band gap materials have been predicted,[219–222] however very limited number of materials have been synthesized and explored experimentally. Accordingly, we propose to make efforts by discovering viable routes to synthesize more novel materials having low band gaps and investigate their optoelectronic properties. Efforts to tune the band gap of already known materials by employing strategies beyond the existing one can help in tuning the optoelectronic properties.

2. Silver- and copper-bismuth halide materials have also gained significant attention because of their reduced band gap (~1.8 eV) and PCE up to 5.6% (for sulfur doped Ag_3BiI_6).[251] However, more fundamental investigations by combining experimental and theoretical studies on optoelectronic properties of these materials are necessary to understand the material's intrinsic properties such as optical, transport and recombination properties. Additionally, investigation on the effect of residual AgI (as observed in Ag-rich compositions such as Ag_3BiI_6)[265] and residual BiI_3 (observed in $AgBi_2I_7$)[258] on charge carrier dynamics, recombination lifetime, device performance and stability are necessary to underline the suitable composition for efficient photovoltaic devices. Silver-bismuth-halides materials are known to exist in impure phase at room temperature and Ag-rich phase tend to degrade under ambient humidity condition when interfaced with polymer transport layer and gold metal electrode.[265] Hence, more attempts are required emphasizing on long-term stability of the material, understanding the degradation mechanism as well as exploring suitable choice of transport layers.

3. The choice of charge transport layers is crucial to improve the device performance. Comprehension of literature suggests that widely used TiO_2 and spiro-OMeTAD (and/or

P3HT) as n-type and p-type contacts do not work well with these lead-free materials[238,241,258] and hence exploring suitable charge transport layers might play a crucial role. Better understanding of carrier dynamics at these interfaces can also help in understanding and improving the device performance and stability. Understanding the precursor material – solvent interaction within the solution of lead-halide perovskites is gaining significant attention as it helps in eliminating the defect sites at micro level and enhancing the device performance and stability with high reproducibility.[288–291][4] Similarly, studies on the solution composition and formed complex/species of bismuth-based lead-free materials may help in understanding the nucleation and crystallization processes and eliminating the defects such as bismuth interstitials (or iodide vacancies) which is vital for the development of efficient devices.

Comprehension of research efforts and our understanding suggests that overcoming the present challenges by focusing on investigating the fundamental intrinsic properties such as absorption, transport and recombination properties of materials followed by fabricating devices with exploring suitable choice of transport layers can help to improve the performance of lead-free perovskite and perovskite-inspired materials based solar cells. In addition to this, new approaches based on machine learning[292–296] might facilitate the screening of such properties in search for design of novel and stable bismuth-based lead-free materials and thereby efficient lead-free photovoltaic devices.

ACKNOWLEDGEMENTS

F.Ü. and S.M. gratefully acknowledge the German Research Foundation (Deutsche Forschungsgemeinschaft) for the financial support within the priority program SPP 2196.-

"Perovskite Semiconductors: From Fundamental Properties to Devices". A.K. and T.K. gratefully acknowledge funding from the Helmholtz Association via the project PEROSEED.

REFERENCES

[1] A. Kojima, K. Teshima, Y. Shirai, T. Miyasaka, *J. Am. Chem. Soc.* **2009**, *131*, 6050.

[2] M. M. Lee, J. Teuscher, T. Miyasaka, T. N. Murakami, H. J. Snaith, *Science (80-.).* **2012**, *338*, 643 LP.

[3] N.-G. Park, M. Grätzel, T. Miyasaka, K. Zhu, K. Emery, *Nat. Energy* **2016**, *1*, 16152.

[4] A. Kumar Jena, A. Kulkarni, T. Miyasaka, *Chem. Rev.* **2019**, *119*, 3036.

[5] J. Jeong, M. Kim, J. Seo, H. Lu, P. Ahlawat, A. Mishra, Y. Yang, M. A. Hope, F. T. Eickemeyer, M. Kim, Y. J. Yoon, I. W. Choi, B. P. Darwich, S. J. Choi, Y. Jo, J. H. Lee, B. Walker, S. M. Zakeeruddin, L. Emsley, U. Rothlisberger, A. Hagfeldt, D. S. Kim, M. Grätzel, J. Y. Kim, *Nature* **2021**, *592*, 381.

[6] M. Saliba, T. Matsui, J.-Y. Seo, K. Domanski, J.-P. Correa-Baena, M. K. Nazeeruddin, S. M. Zakeeruddin, W. Tress, A. Abate, A. Hagfeldt, M. Grätzel, *Energy Environ. Sci.* **2016**, *9*, 1989.

[7] J. H. Noh, S. H. Im, J. H. Heo, T. N. Mandal, S. Il Seok, *Nano Lett.* **2013**, *13*, 1764.

[8] S. D. Stranks, G. E. Eperon, G. Grancini, C. Menelaou, M. J. P. Alcocer, T. Leijtens, L. M. Herz, A. Petrozza, H. J. Snaith, *Science (80-.).* **2013**, *342*, 341 LP.

[9] Q. Dong, Y. Fang, Y. Shao, P. Mulligan, J. Qiu, L. Cao, J. Huang, *Science (80-.).* **2015**, *347*, 967 LP.

[10] E. Gutierrez-Partida, H. Hempel, S. Caicedo-Dávila, M. Raoufi, F. Peña-Camargo, M. Grischek, R. Gunder, J. Diekmann, P. Caprioglio, K. O. Brinkmann, H. Köbler, S. Albrecht, T. Riedl, A. Abate, D. Abou-Ras, T. Unold, D. Neher, M. Stolterfoht, *ACS Energy Lett.* **2021**, *6*, 1045.

[11] L. Krückemeier, B. Krogmeier, Z. Liu, U. Rau, T. Kirchartz, *Adv. Energy Mater.* **2021**,

11, 2003489.

[12] T. Kirchartz, J. A. Márquez, M. Stolterfoht, T. Unold, *Adv. Energy Mater.* **2020**, *10*, 1904134.

[13] G. Xing, N. Mathews, S. Sun, S. S. Lim, Y. M. Lam, M. Grätzel, S. Mhaisalkar, T. C. Sum, *Science (80-.).* **2013**, *342*, 344 LP.

[14] A. Miyata, A. Mitioglu, P. Plochocka, O. Portugall, J. T.-W. Wang, S. D. Stranks, H. J. Snaith, R. J. Nicholas, *Nat. Phys.* **2015**, *11*, 582.

[15] M. Hirasawa, T. Ishihara, T. Goto, K. Uchida, N. Miura, *Phys. B Condens. Matter* **1994**, *201*, 427.

[16] V. D'Innocenzo, G. Grancini, M. J. P. Alcocer, A. R. S. Kandada, S. D. Stranks, M. M. Lee, G. Lanzani, H. J. Snaith, A. Petrozza, *Nat. Commun.* **2014**, *5*, 3586.

[17] J. J. Yoo, G. Seo, M. R. Chua, T. G. Park, Y. Lu, F. Rotermund, Y.-K. Kim, C. S. Moon, N. J. Jeon, J.-P. Correa-Baena, V. Bulović, S. S. Shin, M. G. Bawendi, J. Seo, *Nature* **2021**, *590*, 587.

[18] K. Yoshikawa, W. Yoshida, T. Irie, H. Kawasaki, K. Konishi, H. Ishibashi, T. Asatani, D. Adachi, M. Kanematsu, H. Uzu, K. Yamamoto, *Sol. Energy Mater. Sol. Cells* **2017**, *173*, 37.

[19] K. Yoshikawa, H. Kawasaki, W. Yoshida, T. Irie, K. Konishi, K. Nakano, T. Uto, D. Adachi, M. Kanematsu, H. Uzu, K. Yamamoto, *Nat. Energy* **2017**, *2*, 17032.

[20] F. Ünlü, A. Kulkarni, K. Lê, C. Bohr, A. Bliesener, S. D. Öz, A. K. Jena, Y. Ando, T. Miyasaka, T. Kirchartz, S. Mathur, *J. Mater. Res.* **2021**.

[21] V. M. Goldschmidt, *Naturwissenschaften* **1926**, *14*, 477.

[22] C. Li, X. Lu, W. Ding, L. Feng, Y. Gao, Z. Guo, *Acta Crystallogr. Sect. B Struct. Sci.* **2008**, *64*, 702.

[23] K. Miyano, N. Tripathi, M. Yanagida, Y. Shirai, *Acc. Chem. Res.* **2016**, *49*, 303.

[24] K. Tanaka, T. Takahashi, T. Ban, T. Kondo, K. Uchida, N. Miura, *Solid State Commun.*

2003, *127*, 619.

[25] F. Brivio, K. T. Butler, A. Walsh, M. van Schilfgaarde, *Phys. Rev. B* **2014**, *89*, 155204.

[26] M. A. Green, A. Ho-Baillie, H. J. Snaith, *Nat. Photonics* **2014**, *8*, 506.

[27] W.-J. Yin, T. Shi, Y. Yan, *J. Phys. Chem. C* **2015**, *119*, 5253.

[28] C. Wehrenfennig, G. E. Eperon, M. B. Johnston, H. J. Snaith, L. M. Herz, *Adv. Mater.* **2014**, *26*, 1584.

[29] Z. Liu, L. Krückemeier, B. Krogmeier, B. Klingebiel, J. A. Márquez, S. Levcenko, S. Öz, S. Mathur, U. Rau, T. Unold, T. Kirchartz, *ACS Energy Lett.* **2019**, *4*, 110.

[30] Z. Liu, J. Siekmann, B. Klingebiel, U. Rau, T. Kirchartz, *Adv. Energy Mater.* **2021**, *11*, 2003386.

[31] S. Öz, A. K. Jena, A. Kulkarni, K. Mouri, T. Yokoyama, I. Takei, F. Ünlü, S. Mathur, T. Miyasaka, *ACS Energy Lett.* **2020**, *5*, 1292.

[32] N. Pant, A. Kulkarni, M. Yanagida, Y. Shirai, S. Yashiro, M. Sumiya, T. Miyasaka, K. Miyano, *ACS Appl. Energy Mater.* **2021**.

[33] L. Krückemeier, U. Rau, M. Stolterfoht, T. Kirchartz, *Adv. Energy Mater.* **2020**, *10*, 1902573.

[34] U. Rau, B. Blank, T. C. M. Müller, T. Kirchartz, *Phys. Rev. Appl.* **2017**, *7*, 44016.

[35] M. A. Green, A. W. Y. Ho-Baillie, *ACS Energy Lett.* **2019**, *4*, 1639.

[36] Y. Li, R. L. Z. Hoye, H.-H. Gao, L. Yan, X. Zhang, Y. Zhou, J. L. MacManus-Driscoll, J. Gan, *ACS Appl. Mater. Interfaces* **2020**, *12*, 7135.

[37] T. Singh, T. Miyasaka, *Adv. Energy Mater.* **2018**, *8*, 1700677.

[38] G. E. Eperon, S. D. Stranks, C. Menelaou, M. B. Johnston, L. M. Herz, H. J. Snaith, *Energy Environ. Sci.* **2014**, *7*, 982.

[39] R. E. Brandt, V. Stevanović, D. S. Ginley, T. Buonassisi, *MRS Commun.* **2015**, *5*, 265.

[40] A. Zakutayev, C. M. Caskey, A. N. Fioretti, D. S. Ginley, J. Vidal, V. Stevanovic, E. Tea, S. Lany, *J. Phys. Chem. Lett.* **2014**, *5*, 1117.

[41] M.-H. Du, *J. Phys. Chem. Lett.* **2015**, *6*, 1461.

[42] T. Kirchartz, L. Krückemeier, E. L. Unger, *APL Mater.* **2018**, *6*, 100702.

[43] R. Khan, K. O. Ighodalo, Z. Xiao, In *Soft-Matter Thin Film Solar Cells*, AIP Publishing LLC, **2020**, pp. 3–32.

[44] H. Lee, S. Gaiaschi, P. Chapon, D. Tondelier, J.-E. Bourée, Y. Bonnassieux, V. Derycke, B. Geffroy, *J. Phys. Chem. C* **2019**, *123*, 17728.

[45] D. Meggiolaro, E. Mosconi, F. De Angelis, *ACS Energy Lett.* **2019**, *4*, 779.

[46] N. Pant, A. Kulkarni, M. Yanagida, Y. Shirai, T. Miyasaka, K. Miyano, *Adv. Mater. Interfaces* **2020**, *7*, 1901748.

[47] N. Aristidou, C. Eames, I. Sanchez-Molina, X. Bu, J. Kosco, M. S. Islam, S. A. Haque, *Nat. Commun.* **2017**, *8*, 15218.

[48] Z. Song, A. Abate, S. C. Watthage, G. K. Liyanage, A. B. Phillips, U. Steiner, M. Graetzel, M. J. Heben, In *2016 IEEE 43rd Photovoltaic Specialists Conference (PVSC)*, **2016**, pp. 1202–1206.

[49] G. Divitini, S. Cacovich, F. Matteocci, L. Cinà, A. Di Carlo, C. Ducati, *Nat. Energy* **2016**, *1*, 15012.

[50] J. P. Bastos, U. W. Paetzold, R. Gehlhaar, W. Qiu, D. Cheyns, S. Surana, V. Spampinato, T. Aernouts, J. Poortmans, *Adv. Energy Mater.* **2018**, *8*, 1800554.

[51] J. Huang, S. Tan, P. D. Lund, H. Zhou, *Energy Environ. Sci.* **2017**, *10*, 2284.

[52] A. Kakekhani, R. N. Katti, A. M. Rappe, *APL Mater.* **2019**, *7*, 41112.

[53] S. Kundu, T. L. Kelly, *EcoMat* **2020**, *2*, e12025.

[54] T. Miyasaka, A. Kulkarni, G. M. Kim, S. Öz, A. K. Jena, *Adv. Energy Mater.* **2020**, *10*, 1902500.

[55] J. Li, H.-L. Cao, W.-B. Jiao, Q. Wang, M. Wei, I. Cantone, J. Lü, A. Abate, *Nat. Commun.* **2020**, *11*, 310.

[56] A. Babayigit, A. Ethirajan, M. Muller, B. Conings, *Nat. Mater.* **2016**, *15*, 247.

[57] B. Chaudhary, A. Kulkarni, A. K. Jena, M. Ikegami, Y. Udagawa, H. Kunugita, K. Ema, T. Miyasaka, *ChemSusChem* **2017**, *10*, 2473.

[58] A. L. Wani, A. Ara, J. A. Usmani, *Interdiscip. Toxicol.* **2016**, *8*, 55.

[59] A. Babayigit, H.-G. Boyen, B. Conings, *MRS Energy Sustain.* **2018**, *5*, 15.

[60] B. G. Wixson, B. E. Davies, *Environ. Sci. Technol.* **1994**, *28*, 26A.

[61] B. Hailegnaw, S. Kirmayer, E. Edri, G. Hodes, D. Cahen, *J. Phys. Chem. Lett.* **2015**, *6*, 1543.

[62] F. Ünlü, E. Jung, J. Haddad, A. Kulkarni, S. Öz, H. Choi, T. Fischer, S. Chakraborty, T. Kirchartz, S. Mathur, *APL Mater.* **2020**, *8*, 70901.

[63] J. Cao, F. Yan, *Energy Environ. Sci.* **2021**.

[64] A. W. Azhari, F. S. X. Then, D. S. C. Halin, S. Sepeai, N. A. Ludin, *IOP Conf. Ser. Mater. Sci. Eng.* **2020**, *957*.

[65] Q. Chen, N. De Marco, Y. Yang, T. Bin Song, C. C. Chen, H. Zhao, Z. Hong, H. Zhou, Y. Yang, *Nano Today* **2015**, *10*, 355.

[66] S. F. Hoefler, G. Trimmel, T. Rath, *Monatshefte fur Chemie* **2017**, *148*, 795.

[67] F. Hao, C. C. Stoumpos, D. H. Cao, R. P. H. Chang, M. G. Kanatzidis, *Nat. Photonics* **2014**, *8*, 489.

[68] Y. Takahashi, R. Obara, Z. Z. Lin, Y. Takahashi, T. Naito, T. Inabe, S. Ishibashi, K. Terakura, *Dalt. Trans.* **2011**, *40*, 5563.

[69] Y. Takahashi, H. Hasegawa, Y. Takahashi, T. Inabe, *J. Solid State Chem.* **2013**, *205*, 39.

[70] M. Konstantakou, T. Stergiopoulos, *J. Mater. Chem. A* **2017**, *5*, 11518.

[71] Z. Zhao, F. Gu, Y. Li, W. Sun, S. Ye, H. Rao, Z. Liu, *Adv. Sci.* **2017**, *1700204*.

[72] S. Shao, J. Liu, G. Portale, H. Fang, G. R. Blake, G. H. Brink, L. J. A. Koster, M. A. Loi, *Adv. Energy Mater.* **2017**, *1702019*.

[73] E. Jokar, C. Chien, C. Tsai, A. Fathi, E. W. Diau, *Adv. Mater.* **2018**, *1804835*.

[74] Q. Tai, X. Guo, G. Tang, P. You, T. W. Ng, D. Shen, J. Cao, C. K. Liu, N. Wang, Y. Zhu, C. S. Lee, F. Yan, *Angew. Chemie - Int. Ed.* **2019**, *58*, 806.

[75] K. P. Marshall, M. Walker, R. I. Walton, R. A. Hatton, *Nat. Energy* **2016**, *1*, 16178.

[76] J. Seo, S. Il Seok, S. J. Lee, S. S. Shin, Y. C. Kim, D. Kim, T. K. Ahn, J. H. Noh, *J. Am. Chem. Soc.* **2016**, *138*, 3974−3977.

[77] F. Gu, S. Ye, Z. Zhao, H. Rao, Z. Liu, Z. Bian, **2018**, *1800136*, 1.

[78] Z. Jin, B.-B. Yu, M. Liao, D. Liu, J. Xiu, Z. Zhang, E. Lifshitz, J. Tang, H. Song, Z. He, *J. Energy Chem.* **2021**, *54*, 414.

[79] Q. Fu, X. Tang, D. Li, L. Huang, S. Xiao, Y. Chen, T. Hu, *J. Mater. Chem. C* **2020**, *8*, 7786.

[80] T. Song, T. Yokoyama, C. C. Stoumpos, J. Logsdon, D. H. Cao, M. R. Wasielewski, S. Aramaki, M. G. Kanatzidis, *J. Am. Chem. Soc.* **2017**, *139*, 836−842.

[81] W. Li, J. Li, J. Li, J. Fan, L. Wang, *J. Mater. Chem. A* **2016**, *4*, 17104.

[82] T. Nakamura, S. Yakumaru, M. A. Truong, K. Kim, J. Liu, S. Hu, K. Otsuka, R. Hashimoto, R. Murdey, T. Sasamori, H. Do Kim, H. Ohkita, T. Handa, Y. Kanemitsu, A. Wakamiya, *Nat. Commun.* **2020**, *11*, 1.

[83] M. Chen, M.-G. Ju, M. Hu, Z. Dai, Y. Hu, Y. Rong, H. Han, X. C. Zeng, Y. Zhou, N. P. Padture, *ACS Energy Lett.* **2019**, *4*, 276.

[84] M. A. Kamarudin, D. Hirotani, Z. Wang, K. Hamada, K. Nishimura, Q. Shen, T. Toyoda, S. Iikubo, T. Minemoto, K. Yoshino, S. Hayase, *J. Phys. Chem. Lett.* **2019**, *10*, 5277.

[85] P. Li, H. Dong, J. Xu, J. Chen, B. Jiao, X. Hou, J. Li, Z. Wu, *ACS Energy Lett.* **2020**, *5*, 2327.

[86] S. A. A. Shah, M. H. Sayyad, K. Khan, K. Guo, F. Shen, J. Sun, A. K. Tareen, Y. Gong, Z. Guo, *Energies* **2020**, *13*, 5092.

[87] T.-B. Song, T. Yokoyama, S. Aramaki, M. G. Kanatzidis, *ACS Energy Lett.* **2017**, *2*,

897.

[88] L. J. Chen, C. R. Lee, Y. J. Chuang, Z. H. Wu, C. Chen, *J. Phys. Chem. Lett.* **2016**, *7*, 5028.

[89] B. Lee, C. C. Stoumpos, N. Zhou, F. Hao, C. Malliakas, C.-Y. Yeh, T. J. Marks, M. G. Kanatzidis, R. P. H. Chang, *J. Am. Chem. Soc.* **2014**, *136*, 15379.

[90] B. Saparov, J.-P. Sun, W. Meng, Z. Xiao, H.-S. Duan, O. Gunawan, D. Shin, I. G. Hill, Y. Yan, D. B. Mitzi, *Chem. Mater.* **2016**, *28*, 2315.

[91] B. Lee, A. Krenselewski, S. Il Baik, D. N. Seidman, R. P. H. Chang, *Sustain. Energy Fuels* **2017**, *1*, 710.

[92] T. Krishnamoorthy, H. Ding, C. Yan, W. L. Leong, T. Baikie, Z. Zhang, M. Sherburne, S. Li, M. Asta, N. Mathews, S. G. Mhaisalkar, *J. Mater. Chem. A* **2015**, *3*, 23829.

[93] C. Huang, X. C. Yan, G. Cui, Z. Liu, S. Pang, H. Xu, *Novel germanium-containing perovskite material and solar cell comprising same, CN Pat*, 201410173750, **2014**.

[94] N. Ito, M. A. Kamarudin, D. Hirotani, Y. Zhang, Q. Shen, Y. Ogomi, S. Iikubo, T. Minemoto, K. Yoshino, S. Hayase, *J. Phys. Chem. Lett.* **2018**, *9*, 1682−1688.

[95] M. Chen, M.-G. Ju, H. F. Garces, A. D. Carl, L. K. Ono, Z. Hawash, Y. Zhang, T. Shen, Y. Qi, R. L. Grimm, D. Pacifici, X. C. Zeng, Y. Zhou, N. P. Padture, *Nat. Commun.* **2019**, *10*, 16.

[96] K. Nishimura, M. A. Kamarudin, D. Hirotani, K. Hamada, Q. Shen, S. Iikubo, T. Minemoto, K. Yoshino, S. Hayase, *Nano Energy* **2020**, *74*, 104858.

[97] M. R. Filip, F. Giustino, *J. Phys. Chem. C* **2016**, *120*, 166.

[98] J. Grimm, J. F. Suyver, E. Beurer, G. Carver, H. U. Güdel, *J. Phys. Chem. B* **2006**, *110*, 2093.

[99] M. Suta, C. Wickleder, *J. Mater. Chem. C* **2015**, *3*, 5233.

[100] M. Suta, W. Urland, C. Daul, C. Wickleder, *Phys. Chem. Chem. Phys.* **2016**, *18*, 13196.

[101] K. Liang, D. B. Mitzi, *Luminescent organic-inorganic perovskites with a divalent rare*

earth methal halide framework, United States Patent, USA, **1999**.

[102] D. Cortecchia, H. A. Dewi, J. Yin, A. Bruno, S. Chen, T. Baikie, P. P. Boix, M. Grätzel, S. Mhaisalkar, C. Soci, N. Mathews, *Inorg. Chem.* **2016**, 1044.

[103] X.-P. Cui, K.-J. Jiang, J.-H. Huang, Q.-Q. Zhang, M.-J. Su, L.-M. Yang, Y.-L. Song, X.-Q. Zhou, *Synth. Met.* **2015**, *209*, 247.

[104] A. M. Elseman, A. E. Shalan, S. Sajid, M. M. Rashad, A. M. Hassan, M. Li, *ACS Appl. Mater. Interfaces* **2018**, *10*, 11699.

[105] M. Chen, M. G. Ju, A. D. Carl, Y. Zong, R. L. Grimm, J. Gu, X. C. Zeng, Y. Zhou, N. P. Padture, *Joule* **2018**, *2*, 558.

[106] M. G. Ju, M. Chen, Y. Zhou, H. F. Garces, J. Dai, L. Ma, N. P. Padture, X. C. Zeng, *ACS Energy Lett.* **2018**, *3*, 297.

[107] J. Euvrard, X. Wang, T. Li, Y. Yan, D. B. Mitzi, *J. Mater. Chem. A* **2020**, *8*, 4049.

[108] J. L. Mendes, W. Gao, J. L. Martin, A. D. Carl, N. A. Deskins, S. Granados-Focil, R. L. Grimm, *J. Phys. Chem. C* **2020**, *124*, 24289.

[109] Z. Jin, Z. Zhang, J. Xiu, H. Song, T. Gatti, Z. He, *J. Mater. Chem. A* **2020**, *8*, 16166.

[110] A. J. Lehner, D. H. Fabini, H. A. Evans, C. A. Hébert, S. R. Smock, J. Hu, H. Wang, J. W. Zwanziger, M. L. Chabinyc, R. Seshadri, *Chem. Mater.* **2015**, *27*, 7137.

[111] J. P. Correa-Baena, L. Nienhaus, R. C. Kurchin, S. S. Shin, S. Wieghold, N. T. Putri Hartono, M. Layurova, N. D. Klein, J. R. Poindexter, A. Polizzotti, S. Sun, M. G. Bawendi, T. Buonassisi, *Chem. Mater.* **2018**, *30*, 3734.

[112] J.-C. Hebig, I. Kühn, J. Flohre, T. Kirchartz, **2016**, *1*, 309.

[113] K. M. Boopathi, P. Karuppuswamy, A. Singh, C. Hanmandlu, L. Lin, S. A. Abbas, C. C. Chang, P. C. Wang, G. Li, C. W. Chu, *J. Mater. Chem. A* **2017**, *5*, 20843.

[114] S. Chatterjee, A. J. Pal, *ACS Appl. Mater. Interfaces* **2018**, *10*, 35194.

[115] Y. Yang, C. Liu, M. Cai, Y. Liao, Y. Ding, S. Ma, X. Liu, M. Guli, S. Dai, M. K. Nazeeruddin, *ACS Appl. Mater. Interfaces* **2020**, *12*, 17062.

[116] W. Ke, M. G. Kanatzidis, *Nat. Commun.* **2019**, *10*, 965.

[117] G. Schileo, G. Grancini, *J. Mater. Chem. C* **2021**, *9*, 67.

[118] J. Breternitz, S. Schorr, *Adv. Energy Mater.* **2018**, *8*, 1.

[119] M. I. Saidaminov, O. F. Mohammed, O. M. Bakr, *ACS Energy Lett.* **2017**, *2*, 889.

[120] M. E. Kamminga, A. Stroppa, S. Picozzi, M. Chislov, I. A. Zvereva, J. Baas, A. Meetsma, G. R. Blake, T. T. M. Palstra, *Inorg. Chem.* **2017**, *56*, 33.

[121] C. Wu, Q. Zhang, G. Liu, Z. Zhang, D. Wang, B. Qu, Z. Chen, L. Xiao, *Adv. Energy Mater.* **2020**, *10*, 1.

[122] Q. A. Akkerman, L. Manna, *ACS Energy Lett.* **2020**, 604.

[123] A. V. Arakcheeva, M. Bonin, G. Chapuis, A. I. Zaitsev, *Zeitschrift fur Krist. - New Cryst. Struct.* **1999**, *214*, 279.

[124] L. Zhang, C. Liu, Y. Lin, K. Wang, F. Ke, C. Liu, W. L. Mao, B. Zou, *J. Phys. Chem. Lett.* **2019**, *10*, 1676.

[125] T. Kawai, A. Ishii, T. Kitamuha, S. Shimanuki, M. Iwata, Y. Ishibashi, *J. Phys. Soc. Japan* **1996**, *65*, 1464.

[126] S. Öz, J. C. Hebig, E. Jung, T. Singh, A. Lepcha, S. Olthof, F. Jan, Y. Gao, R. German, P. H. M. van Loosdrecht, K. Meerholz, T. Kirchartz, S. Mathur, *Sol. Energy Mater. Sol. Cells* **2016**, 1.

[127] M. Abulikemu, S. Ould-Chikh, X. Miao, E. Alarousu, B. Murali, G. O. Ngongang Ndjawa, J. Barbé, A. El Labban, A. Amassian, S. Del Gobbo, *J. Mater. Chem. A* **2016**, *4*, 12504.

[128] K. Eckhardt, V. Bon, J. Getzschmann, J. Grothe, F. M. Wisser, S. Kaskel, *Chem. Commun.* **2016**, *52*, 3058.

[129] B. W. Park, B. Philippe, X. Zhang, H. Rensmo, G. Boschloo, E. M. J. Johansson, *Adv. Mater.* **2015**, *27*, 6806.

[130] X. Chen, Y. Myung, A. Thind, Z. Gao, B. Yin, M. Shen, S. B. Cho, P. Cheng, B.

Sadtler, R. Mishra, P. Banerjee, *J. Mater. Chem. A* **2017**, *5*, 24728.

[131] S. S. Mali, H. Kim, D. H. Kim, C. Kook Hong, *ChemistrySelect* **2017**, *2*, 1578.

[132] A. Kulkarni, T. Singh, M. Ikegami, T. Miyasaka, *RSC Adv.* **2017**, *7*, 9456.

[133] C. Momblona, H. Kanda, A. A. Sutanto, M. Mensi, C. Roldán-Carmona, M. K. Nazeeruddin, *Sci. Rep.* **2020**, *10*, 1.

[134] L. Zhang, C. Liu, L. Wang, C. Liu, K. Wang, B. Zou, *Angew. Chemie - Int. Ed.* **2018**, *57*, 11213.

[135] R. L. Z. Hoye, R. E. Brandt, A. Osherov, V. Stevanovic, S. D. Stranks, M. W. B. Wilson, H. Kim, A. J. Akey, J. D. Perkins, R. C. Kurchin, J. R. Poindexter, E. N. Wang, M. G. Bawendi, V. Bulovic, T. Buonassisi, *Chem. - A Eur. J.* **2016**, *22*, 2605.

[136] L. C. Lee, T. N. Huq, J. L. Macmanus-Driscoll, R. L. Z. Hoye, *APL Mater.* **2018**, *6*, 12.

[137] J. Pal, A. Bhunia, S. Chakraborty, S. Manna, S. Das, A. Dewan, S. Datta, A. Nag, *J. Phys. Chem. C* **2018**, *122*, 10643.

[138] A. Maiti, G. Paul, H. Bhunia, A. J. Pal, *Sol. Energy Mater. Sol. Cells* **2019**, *200*, 109941.

[139] M. B. Johansson, B. Philippe, A. Banerjee, D. Phuyal, S. Mukherjee, S. Chakraborty, M. Cameau, H. Zhu, R. Ahuja, G. Boschloo, H. Rensmo, E. M. J. Johansson, *Inorg. Chem.* **2019**, *58*, 12040.

[140] K. H. Hong, J. Kim, L. Debbichi, H. Kim, S. H. Im, *J. Phys. Chem. C* **2017**, *121*, 969.

[141] J. Gu, G. Yan, Y. Lian, Q. Mu, H. Jin, Z. Zhang, Z. Deng, Y. Peng, *RSC Adv.* **2018**, *8*, 25802.

[142] A. Rajagopal, R. J. Stoddard, H. W. Hillhouse, A. K. Y. Jen, *J. Mater. Chem. A* **2019**, *7*, 16285.

[143] S. Chatterjee, J. Payne, J. T. S. Irvine, A. J. Pal, *J. Mater. Chem. A* **2020**, *8*, 4416.

[144] K. M. McCall, C. C. Stoumpos, O. Y. Kontsevoi, G. C. B. Alexander, B. W. Wessels, M. G. Kanatzidis, *Chem. Mater.* **2019**, *31*, 2644.

[145] B.-B. Yu, M. Liao, J. Yang, W. Chen, Y. Zhu, X. Zhang, T. Duan, W. Yao, S.-H. Wei, Z. He, *J. Mater. Chem. A* **2019**, *7*, 8818.

[146] J. Li, X. Liu, J. Xu, J. Chen, C. Zhao, M. Salma Maneno, B. Zhang, J. Yao, *Sol. RRL* **2019**, *3*, 1.

[147] I. Benabdallah, M. Boujnah, A. El Kenz, A. Benyoussef, M. Abatal, A. Bassam, *J. Alloys Compd.* **2019**, *773*, 796.

[148] Y. Y. Sun, J. Shi, J. Lian, W. Gao, M. L. Agiorgousis, P. Zhang, S. Zhang, *Nanoscale* **2016**, *8*, 6284.

[149] M. Vigneshwaran, T. Ohta, S. Iikubo, G. Kapil, T. S. Ripolles, Y. Ogomi, T. Ma, S. S. Pandey, Q. Shen, T. Toyoda, K. Yoshino, T. Minemoto, S. Hayase, *Chem. Mater.* **2016**, *28*, 6436.

[150] J. Wong, S. T. Omelchenko, H. A. Atwater, *ACS Energy Lett.* **2021**, *6*, 52.

[151] M. Lyu, J. H. Yun, M. Cai, Y. Jiao, P. V. Bernhardt, M. Zhang, Q. Wang, A. Du, H. Wang, G. Liu, L. Wang, *Nano Res.* **2016**, *9*, 692.

[152] T. Singh, A. Kulkarni, M. Ikegami, T. Miyasaka, *ACS Appl. Mater. Interfaces* **2016**, *8*, 14542.

[153] S. Sanders, D. Stümmler, P. Pfeiffer, N. Ackermann, F. Schimkat, G. Simkus, M. Heuken, P. K. Baumann, A. Vescan, H. Kalisch, *Phys. Status Solidi Appl. Mater. Sci.* **2018**, *215*, 1.

[154] X. Zhang, G. Wu, Z. Gu, B. Guo, W. Liu, S. Yang, T. Ye, C. Chen, W. Tu, H. Chen, *Nano Res.* **2016**, *9*, 2921.

[155] M.-C. Tang, D. Barrit, R. Munir, R. Li, J. M. Barbé, D.-M. Smilgies, S. Del Gobbo, T. D. Anthopoulos, A. Amassian, *Sol. RRL* **2019**, *3*, 1800305.

[156] Q. Jia, C. Li, W. Tian, M. B. Johansson, E. M. J. Johansson, R. Yang, *ACS Appl. Mater. Interfaces* **2020**, *12*, 43876.

[157] S. S. Shin, J. P. Correa Baena, R. C. Kurchin, A. Polizzotti, J. J. Yoo, S. Wieghold, M.

G. Bawendi, T. Buonassisi, *Chem. Mater.* **2018**, *30*, 336.

[158] S. M. Jain, D. Phuyal, M. L. Davies, M. Li, B. Philippe, C. De Castro, Z. Qiu, J. Kim, T. Watson, W. C. Tsoi, O. Karis, H. Rensmo, G. Boschloo, T. Edvinsson, J. R. Durrant, *Nano Energy* **2018**, *49*, 614.

[159] S. M. Jain, T. Edvinsson, J. R. Durrant, *Commun. Chem.* **2019**, *2*, 1.

[160] B. Ghosh, S. Chakraborty, H. Wei, C. Guet, S. Li, S. Mhaisalkar, N. Mathews, *J. Phys. Chem. C* **2017**, *121*, 17062.

[161] B. Ghosh, B. Wu, H. K. Mulmudi, C. Guet, K. Weber, T. C. Sum, S. Mhaisalkar, N. Mathews, *ACS Appl. Mater. Interfaces* **2018**, *10*, 35000.

[162] F. Bai, Y. Hu, Y. Hu, T. Qiu, X. Miao, S. Zhang, *Sol. Energy Mater. Sol. Cells* **2018**, *184*, 15.

[163] W. Hu, X. He, Z. Fang, W. Lian, Y. Shang, X. Li, W. Zhou, M. Zhang, T. Chen, Y. Lu, L. Zhang, L. Ding, S. Yang, *Nano Energy* **2020**, *68*, 104362.

[164] U. H. Hamdeh, B. J. Ryan, R. D. Nelson, M. Zembrzuski, J. Slobidsky, K. J. Prince, I. Cleveland, A. Vela-Ramirez, A. C. Hillier, M. G. Panthani, *J. Phys. Chem. Lett.* **2019**, *10*, 3134.

[165] C. Lan, G. Liang, S. Zhao, H. Lan, H. Peng, D. Zhang, H. Sun, J. Luo, P. Fan, *Sol. Energy* **2019**, *177*, 501.

[166] T. Okano, Y. Suzuki, *Mater. Lett.* **2017**, *191*, 77.

[167] H. Wang, J. Tian, K. Jiang, Y. Zhang, H. Fan, J. Huang, L. M. Yang, B. Guan, Y. Song, *RSC Adv.* **2017**, *7*, 43826.

[168] C. Ran, Z. Wu, J. Xi, F. Yuan, H. Dong, T. Lei, X. He, X. Hou, *J. Phys. Chem. Lett.* **2017**, *8*, 394.

[169] Z. Zhang, X. Li, X. Xia, Z. Wang, Z. Huang, B. Lei, Y. Gao, *J. Phys. Chem. Lett.* **2017**, *8*, 4300.

[170] S. Sanders, D. Stümmler, P. Pfeiffer, N. Ackermann, G. Simkus, M. Heuken, P. K.

Baumann, A. Vescan, H. Kalisch, *Sci. Rep.* **2019**, *9*, 1.

[171] D. Stümmler, S. Sanders, F. Gerstenberger, P. Pfeiffer, G. Simkus, P. K. Baumann, M. Heuken, A. Vescan, H. Kalisch, *J. Mater. Res.* **2019**, *34*, 608.

[172] T. Mohammad, V. Kumar, V. Dutta, *Sol. Energy* **2019**, *182*, 72.

[173] Y. Wang, Y. Liu, Y. Xu, C. Zhang, H. Bao, J. Wang, Z. Guo, L. Wan, D. Eder, S. Wang, *Electrochim. Acta* **2020**, *329*.

[174] D. B. Mitzi, *Prog. Inorg. Chem.* **1999**, *48*, 1.

[175] D. B. Mitzi, *Inorg. Chem.* **2000**, *39*, 6107.

[176] D. B. Mitzi, P. Brock, *Inorg. Chem.* **2001**, *40*, 2096.

[177] T. Li, Y. Hu, C. A. Morrison, W. Wu, H. Han, N. Robertson, *Sustain. Energy Fuels* **2017**, *1*, 308.

[178] A. N. Usoltsev, M. Elshobaki, S. A. Adonin, L. A. Frolova, T. Derzhavskaya, P. A. Abramov, D. V. Anokhin, I. V. Korolkov, S. Y. Luchkin, N. N. Dremova, K. J. Stevenson, M. N. Sokolov, V. P. Fedin, P. A. Troshin, *J. Mater. Chem. A* **2019**, *7*, 5957.

[179] N. Dehnhardt, J. N. Luy, M. Szabo, M. Wende, R. Tonner, J. Heine, *Chem. Commun.* **2019**, *55*, 14725.

[180] K. Ahmad, S. N. Ansari, K. Natarajan, S. M. Mobin, *ACS Appl. Energy Mater.* **2018**, *1*, 2405.

[181] M. S. Ozório, W. X. C. Oliveira, J. F. R. V. Silveira, A. F. Nogueira, J. L. F. Da Silva, *Mater. Adv.* **2020**, *1*, 3439.

[182] G.-X. Liang, X.-Y. Chen, Z.-H. Chen, H.-B. Lan, Z.-H. Zheng, P. Fan, X.-Q. Tian, J.-Y. Duan, Y.-D. Wei, Z.-H. Su, *J. Phys. Chem. C* **2019**, *123*, 27423.

[183] J. K. Pious, A. Katre, C. Muthu, S. Chakraborty, S. Krishna, V. C. Nair, *Chem. Mater.* **2019**, *31*, 1941.

[184] G. A. Fisher, N. C. Norman, *Adv. Inorg. Chem.* **1994**, *41*, 233.

[185] D. M. Fabian, S. Ardo, *J. Mater. Chem. A* **2016**, *4*, 6837.

[186] A. J. Dennington, M. T. Weller, *Dalt. Trans.* **2018**, *47*, 3469.

[187] W. Zhang, K. Tao, C. Ji, Z. Sun, S. Han, J. Zhang, Z. Wu, J. Luo, *Inorg. Chem.* **2018**, *57*, 4239.

[188] M. B. Johansson, H. Zhu, E. M. J. Johansson, *J. Phys. Chem. Lett.* **2016**, *7*, 3467.

[189] D. B. Khadka, Y. Shirai, M. Yanagida, K. Miyano, *J. Mater. Chem. C* **2019**, *7*, 8335.

[190] H. Lan, X. Chen, P. Fan, G. Liang, *J. Mater. Sci. Mater. Electron.* **2021**, *32*, 11183.

[191] C. W. Cross, W. F. Hillebrand, *Am. J. Sci.* **1883**, *s3-26*, 271 LP.

[192] H. L. Wells, *Am. J. Sci.* **1893**, *s3-45*, 121 LP.

[193] N. R. Wolf, B. A. Connor, A. H. Slavney, H. I. Karunadasa, *Angew. Chemie Int. Ed.* **2021**, *n/a*.

[194] Z. Deng, F. Wei, S. Sun, G. Kieslich, A. K. Cheetham, P. D. Bristowe, *J. Mater. Chem. A* **2016**, *4*, 12025.

[195] P. Cheng, T. Wu, Y. Li, L. Jiang, W. Deng, K. Han, *New J. Chem.* **2017**, *41*, 9598.

[196] P. Zhang, J. Yang, S.-H. Wei, *J. Mater. Chem. A* **2018**, *6*, 1809.

[197] H. L. Wells, *Am. J. Sci.* **1922**, *s5-3*, 315 LP.

[198] S. Yamada, R. Tsuchida, *Bull. Chem. Soc. Jpn.* **1956**, *29*, 421.

[199] G. Brauer, G. Sleater, *J. Less Common Met.* **1970**, *21*, 283.

[200] A. E. Maughan, A. M. Ganose, M. M. Bordelon, E. M. Miller, D. O. Scanlon, J. R. Neilson, *J. Am. Chem. Soc.* **2016**, *138*, 8453.

[201] G. Giorgi, K. Yamashita, *Chem. Lett.* **2015**, *44*, 826.

[202] A. H. Slavney, T. Hu, A. M. Lindenberg, H. I. Karunadasa, *J. Am. Chem. Soc.* **2016**, *138*, 2138.

[203] E. T. McClure, M. R. Ball, W. Windl, P. M. Woodward, *Chem. Mater.* **2016**, *28*, 1348.

[204] G. Volonakis, M. R. Filip, A. A. Haghighirad, N. Sakai, B. Wenger, H. J. Snaith, F. Giustino, *J. Phys. Chem. Lett.* **2016**, *7*, 1254.

[205] G. Volonakis, A. A. Haghighirad, R. L. Milot, W. H. Sio, M. R. Filip, B. Wenger, M. B. Johnston, L. M. Herz, H. J. Snaith, F. Giustino, *J. Phys. Chem. Lett.* **2017**, *8*, 772.

[206] J. Zhou, Z. Xia, M. S. Molokeev, X. Zhang, D. Peng, Q. Liu, *J. Mater. Chem. A* **2017**, *5*, 15031.

[207] A. H. Slavney, L. Leppert, A. Saldivar Valdes, D. Bartesaghi, T. J. Savenije, J. B. Neaton, H. I. Karunadasa, *Angew. Chemie Int. Ed.* **2018**, *57*, 12765.

[208] T. T. Tran, J. R. Panella, J. R. Chamorro, J. R. Morey, T. M. McQueen, *Mater. Horizons* **2017**, *4*, 688.

[209] K. Du, W. Meng, X. Wang, Y. Yan, D. B. Mitzi, *Angew. Chemie Int. Ed.* **2017**, *56*, 8158.

[210] A. H. Slavney, L. Leppert, D. Bartesaghi, A. Gold-Parker, M. F. Toney, T. J. Savenije, J. B. Neaton, H. I. Karunadasa, *J. Am. Chem. Soc.* **2017**, *139*, 5015.

[211] K. P. Lindquist, S. A. Mack, A. H. Slavney, L. Leppert, A. Gold-Parker, J. F. Stebbins, A. Salleo, M. F. Toney, J. B. Neaton, H. I. Karunadasa, *Chem. Sci.* **2019**, *10*, 10620.

[212] G. Longo, S. Mahesh, L. R. V Buizza, A. D. Wright, A. J. Ramadan, M. Abdi-Jalebi, P. K. Nayak, L. M. Herz, H. J. Snaith, *ACS Energy Lett.* **2020**, *5*, 2200.

[213] L. Schade, A. D. Wright, R. D. Johnson, M. Dollmann, B. Wenger, P. K. Nayak, D. Prabhakaran, L. M. Herz, R. Nicholas, H. J. Snaith, P. G. Radaelli, *ACS Energy Lett.* **2019**, *4*, 299.

[214] S. J. Zelewski, J. M. Urban, A. Surrente, D. K. Maude, A. Kuc, L. Schade, R. D. Johnson, M. Dollmann, P. K. Nayak, H. J. Snaith, P. Radaelli, R. Kudrawiec, R. J. Nicholas, P. Plochocka, M. Baranowski, *J. Mater. Chem. C* **2019**, *7*, 8350.

[215] A. D. Wright, L. R. V Buizza, K. J. Savill, G. Longo, H. J. Snaith, M. B. Johnston, L. M. Herz, *J. Phys. Chem. Lett.* **2021**, *12*, 3352.

[216] L. Schade, S. Mahesh, G. Volonakis, M. Zacharias, B. Wenger, F. Schmidt, S. V. Kesava, D. Prabhakaran, M. Abdi-Jalebi, M. Lenz, F. Giustino, G. Longo, P. G.

Radaelli, H. J. Snaith, *ACS Energy Lett.* **2021**, *6*, 1073.

[217] S. E. Creutz, E. N. Crites, M. C. De Siena, D. R. Gamelin, *Nano Lett.* **2018**, *18*, 1118.

[218] C. Zhang, L. Gao, S. Teo, Z. Guo, Z. Xu, S. Zhao, T. Ma, *Sustain. Energy Fuels* **2018**, *2*, 2419.

[219] X.-G. Zhao, J.-H. Yang, Y. Fu, D. Yang, Q. Xu, L. Yu, S.-H. Wei, L. Zhang, *J. Am. Chem. Soc.* **2017**, *139*, 2630.

[220] T. Li, X. Zhao, D. Yang, M.-H. Du, L. Zhang, *Phys. Rev. Appl.* **2018**, *10*, 41001.

[221] Q. Xu, D. Yang, J. Lv, Y.-Y. Sun, L. Zhang, *Small Methods* **2018**, *2*, 1700316.

[222] X.-G. Zhao, D. Yang, Y. Sun, T. Li, L. Zhang, L. Yu, A. Zunger, *J. Am. Chem. Soc.* **2017**, *139*, 6718.

[223] F. Wei, Z. Deng, S. Sun, F. Xie, G. Kieslich, D. M. Evans, M. A. Carpenter, P. D. Bristowe, A. K. Cheetham, *Mater. Horizons* **2016**, *3*, 328.

[224] F. Wei, Z. Deng, S. Sun, F. Zhang, D. M. Evans, G. Kieslich, S. Tominaka, M. A. Carpenter, J. Zhang, P. D. Bristowe, A. K. Cheetham, *Chem. Mater.* **2017**, *29*, 1089.

[225] E. Greul, M. L. Petrus, A. Binek, P. Docampo, T. Bein, *J. Mater. Chem. A* **2017**, *5*, 19972.

[226] C. Wu, Q. Zhang, Y. Liu, W. Luo, X. Guo, Z. Huang, H. Ting, W. Sun, X. Zhong, S. Wei, S. Wang, Z. Chen, L. Xiao, *Adv. Sci.* **2018**, *5*, 1700759.

[227] W. Gao, C. Ran, J. Xi, B. Jiao, W. Zhang, M. Wu, X. Hou, Z. Wu, *ChemPhysChem* **2018**, *19*, 1696.

[228] M. Pantaler, K. T. Cho, V. I. E. Queloz, I. García Benito, C. Fettkenhauer, I. Anusca, M. K. Nazeeruddin, D. C. Lupascu, G. Grancini, *ACS Energy Lett.* **2018**, *3*, 1781.

[229] M. Wang, P. Zeng, S. Bai, J. Gu, F. Li, Z. Yang, M. Liu, *Sol. RRL* **2018**, *2*, 1800217.

[230] C. N. Savory, A. Walsh, D. O. Scanlon, *ACS Energy Lett.* **2016**, *1*, 949.

[231] P. H. Fourcroy, M. Palazzi, J. Rivet, J. Flahaut, R. Céolin, *Mater. Res. Bull.* **1979**, *14*, 325.

[232] K. B. Dzeranova, N. I. Kaloev, G. A. Bulakhova, *Zhurnal Neorg. Khimii* **1985**, *30*, 2983.

[233] P. H. Fourcroy, D. Carré, F. Thévet, J. Rivet, *Acta Crystallogr. Sect. C* **1991**, *47*, 2023.

[234] T. Oldag, T. Aussieker, H. L. Keller, C. Preitschaft, A. Pfitzner, *Zeitschrift fur Anorg. und Allg. Chemie* **2005**, *631*, 677.

[235] L. F. Mashadieva, Z. S. Aliev, A. V. Shevelkov, M. B. Babanly, *J. Alloys Compd.* **2013**, *551*, 512.

[236] K. W. Jung, M. R. Sohn, H. M. Lee, I. S. Yang, S. Do Sung, J. Kim, E. Wei-Guang Diau, W. I. Lee, *Sustain. Energy Fuels* **2018**, *2*, 294.

[237] S. S. Hosseini, M. Adelifard, M. Ataei, *J. Mater. Sci. Mater. Electron.* **2019**, *30*, 5021.

[238] Y. Kim, Z. Yang, A. Jain, O. Voznyy, G.-H. Kim, M. Liu, L. N. Quan, F. P. García de Arquer, R. Comin, J. Z. Fan, E. H. Sargent, *Angew. Chemie* **2016**, *128*, 9738.

[239] Z. Xiao, W. Meng, D. B. Mitzi, Y. Yan, *J. Phys. Chem. Lett.* **2016**, *7*, 3903.

[240] H. C. Sansom, G. F. S. Whitehead, M. S. Dyer, M. Zanella, T. D. Manning, M. J. Pitcher, T. J. Whittles, V. R. Dhanak, J. Alaria, J. B. Claridge, M. J. Rosseinsky, *Chem. Mater.* **2017**, *29*, 1538.

[241] I. Turkevych, S. Kazaoui, E. Ito, T. Urano, K. Yamada, H. Tomiyasu, H. Yamagishi, M. Kondo, S. Aramaki, *ChemSusChem* **2017**, *10*, 3754.

[242] A. Crovetto, A. Hajijafarassar, O. Hansen, B. Seger, I. Chorkendorff, P. C. K. Vesborg, *Chem. Mater.* **2020**, *32*, 3385.

[243] H. Zhu, M. Pan, M. B. Johansson, E. M. J. J. Johansson, *ChemSusChem* **2017**, *10*, 2592.

[244] M. Kong, H. Hu, L. Wan, M. Chen, Y. Gan, J. Wang, F. Chen, B. Dong, D. Eder, S. Wang, *RSC Adv.* **2017**, *7*, 35549.

[245] H. Wu, H. Zhu, A. Erbing, M. B. Johansson, S. Mukherjee, G. J. Man, H. Rensmo, M. Odelius, E. M. J. Johansson, *ACS Appl. Energy Mater.* **2019**, *2*, 5356.

[246] Y. Seo, S. R. Ha, S. Yoon, S. M. Jeong, H. Choi, D.-W. Kang, *J. Power Sources* **2020**, *453*, 227903.

[247] B. Ghosh, B. Wu, X. Guo, P. C. Harikesh, R. A. John, T. Baikie, Arramel, A. T. S. Wee, C. Guet, T. C. Sum, S. Mhaisalkar, N. Mathews, *Adv. Energy Mater.* **2018**, *8*, 1802051.

[248] H. Yu, B. Zhang, R. Qi, N. Qu, C. Zhao, Y. Lei, X. Yang, Z. Zheng, *Sustain. Energy Fuels* **2020**, *4*, 2800.

[249] Z. Hu, Z. Wang, G. Kapil, T. Ma, S. Iikubo, T. Minemoto, K. Yoshino, T. Toyoda, Q. Shen, S. Hayase, *ChemSusChem* **2018**, *11*, 2930.

[250] C. Lu, J. Zhang, H. Sun, D. Hou, X. Gan, M. Shang, Y. Li, Z. Hu, Y. Zhu, L. Han, *ACS Appl. Energy Mater.* **2018**, *1*, 4485.

[251] N. Pai, J. Lu, T. R. Gengenbach, A. Seeber, A. S. R. Chesman, L. Jiang, D. C. Senevirathna, P. C. Andrews, U. Bach, Y. Cheng, A. N. Simonov, *Adv. Energy Mater.* **2018**, *9*, 1803396.

[252] H. Zhu, A. Erbing, H. Wu, G. J. Man, S. Mukherjee, C. Kamal, M. B. Johansson, H. Rensmo, M. Odelius, E. M. J. Johansson, *ACS Appl. Energy Mater.* **2020**, *3*, 7372.

[253] J. W. Park, Y. Lim, K. Y. Doh, M. T. Jung, Y. I. Jeon, I. S. Yang, H. S. Choi, J. Kim, D. Lee, W. I. Lee, *Sustain. Energy Fuels* **2021**, *5*, 1439.

[254] F. Yu, L. Wang, K. Ren, S. Yang, Z. Xu, Q. Han, T. Ma, *ACS Sustain. Chem. Eng.* **2020**, *8*, 9980.

[255] H. C. Sansom, G. Longo, A. D. Wright, L. R. V Buizza, S. Mahesh, B. Wenger, M. Zanella, M. Abdi-Jalebi, M. J. Pitcher, M. S. Dyer, T. D. Manning, R. H. Friend, L. M. Herz, H. J. Snaith, J. B. Claridge, M. J. Rosseinsky, *J. Am. Chem. Soc.* **2021**, *143*, 3983.

[256] M. Khazaee, K. Sardashti, J.-P. Sun, H. Zhou, C. Clegg, I. G. Hill, J. L. Jones, D. C. Lupascu, D. B. Mitzi, *Chem. Mater.* **2018**, *30*, 3538.

[257] M. Khazaee, K. Sardashti, C. C. Chung, J. P. Sun, H. Zhou, E. Bergmann, W. A. Dunlap-Shohl, Q. Han, I. G. Hill, J. L. Jones, D. C. Lupascu, D. B. Mitzi, *J. Mater. Chem. A* **2019**, *7*, 2095.

[258] A. Kulkarni, A. K. Jena, M. Ikegami, T. Miyasaka, *Chem. Commun.* **2019**, *55*, 4031.

[259] Q. Zhang, C. Wu, X. Qi, F. Lv, Z. Zhang, Y. Liu, S. Wang, B. Qu, Z. Chen, L. Xiao, *ACS Appl. Energy Mater.* **2019**, *2*, 3651.

[260] A. K. Baranwal, H. Masutani, H. Sugita, H. Kanda, S. Kanaya, N. Shibayama, Y. Sanehira, M. Ikegami, Y. Numata, K. Yamada, T. Miyasaka, T. Umeyama, H. Imahori, S. Ito, *Nano Converg.* **2017**, *4*, 26.

[261] J. Tu, C. Kou, M. Liu, H. Lu, Y. Liu, H. Tan, W. Li, Z. Bo, *SN Appl. Sci.* **2019**, *1*, 1.

[262] S. Hosseini, M. Adelifard, *Phys. Status Solidi Appl. Mater. Sci.* **2021**, *218*, 1.

[263] S. S. Hosseini, M. Adelifard, *J. Electron. Mater.* **2020**, *49*, 5790.

[264] Z. Yi, T. Zhang, H. Ban, H. Shao, X. Gong, M. Wu, G. Liang, X. L. Zhang, Y. Shen, M. Wang, *Sol. Energy* **2020**, *206*, 436.

[265] A. Kulkarni, F. Ünlü, N. Pant, J. Kaur, C. Bohr, A. K. Jena, S. Öz, M. Yanagida, Y. Shirai, M. Ikegami, K. Miyano, Y. Tachibana, S. Chakraborty, S. Mathur, T. Miyasaka, *Sol. RRL* **2021**, *n/a*.

[266] A. J. Lehner, H. Wang, D. H. Fabini, C. D. Liman, C. A. Hébert, E. E. Perry, M. Wang, G. C. Bazan, M. L. Chabinyc, R. Seshadri, *Appl. Phys. Lett.* **2015**, *107*, 1.

[267] R. E. Brandt, R. C. Kurchin, R. L. Z. Hoye, J. R. Poindexter, M. W. B. Wilson, S. Sulekar, F. Lenahan, P. X. T. Yen, V. Stevanović, J. C. Nino, M. G. Bawendi, T. Buonassisi, *J. Phys. Chem. Lett.* **2015**, *6*, 4297.

[268] K. M. Boopathi, S. Raman, R. Mohanraman, F. C. Chou, Y. Y. Chen, C. H. Lee, F. C. Chang, C. W. Chu, *Sol. Energy Mater. Sol. Cells* **2014**, *121*, 35.

[269] N. J. Podraza, W. Qiu, B. B. Hinojosa, H. Xu, M. A. Motyka, S. R. Phillpot, J. E. Baciak, S. Trolier-Mckinstry, J. C. Nino, *J. Appl. Phys.* **2013**, *114*.

[270] F. Ma, M. Zhou, Y. Jiao, G. Gao, Y. Gu, A. Bilic, Z. Chen, A. Du, *Sci. Rep.* **2015**, *5*, 17558.

[271] R. E. Brandt, R. C. Kurchin, R. L. Z. Hoye, J. R. Poindexter, M. W. B. Wilson, S. Sulekar, F. Lenahan, P. X. T. Yen, V. Stevanović, J. C. Nino, M. G. Bawendi, T. Buonassisi, *J. Phys. Chem. Lett.* **2015**, *6*, 4297.

[272] M. A. Green, M. J. Keevers, *Prog. Photovoltaics Res. Appl.* **1995**, *3*, 189.

[273] J. S. Blakemore, *J. Appl. Phys.* **1982**, *53*, R123.

[274] U. H. Hamdeh, R. D. Nelson, B. J. Ryan, U. Bhattacharjee, J. W. Petrich, M. G. Panthani, *Chem. Mater.* **2016**, *28*, 6567.

[275] A. Kulkarni, T. Singh, A. K. Jena, P. Pinpithak, M. Ikegami, T. Miyasaka, *ACS Appl. Mater. Interfaces* **2018**, *10*, 9547.

[276] B. W. Williamson, F. T. Eickemeyer, H. W. Hillhouse, *ACS Omega* **2018**, *3*, 12713.

[277] D. Tiwari, D. Alibhai, D. J. Fermin, *ACS Energy Lett.* **2018**, *3*, 1882.

[278] L. Lin, K. M. Boopathi, J. Ding, C. W. Chu, C. C. Chang, *FlatChem* **2017**, *5*, 18.

[279] J. Kang, S. Chen, X. Zhao, H. Yin, W. Zhang, M. Al-Mamun, P. Liu, Y. Wang, H. Zhao, *Nano Energy* **2020**, *73*, 104799.

[280] D. Bryant, N. Aristidou, S. Pont, I. Sanchez-Molina, T. Chotchunangatchaval, S. Wheeler, J. R. Durrant, S. A. Haque, *Energy Environ. Sci.* **2016**, *9*, 1655.

[281] P. Toloueinia, H. Khassaf, A. Shirazi Amin, Z. M. Tobin, S. P. Alpay, S. L. Suib, *ACS Appl. Energy Mater.* **2020**, *3*, 8240.

[282] Q. Wang, B. Chen, Y. Liu, Y. Deng, Y. Bai, Q. Dong, J. Huang, *Energy Environ. Sci.* **2017**, *10*, 516.

[283] S. Trivedi, D. Prochowicz, N. Parikh, A. Mahapatra, M. K. Pandey, A. Kalam, M. M. Tavakoli, P. Yadav, *ACS Omega* **2021**, *6*, 1030.

[284] A. Y. Alsalloum, B. Turedi, K. Almasabi, X. Zheng, R. Naphade, S. D. Stranks, O. F. Mohammed, O. M. Bakr, *Energy Environ. Sci.* **2021**, *14*, 2263.

[285] Y. Song, W. Bi, A. Wang, X. Liu, Y. Kang, Q. Dong, *Nat. Commun.* **2020**, *11*, 274.

[286] Q. Lv, W. He, Z. Lian, J. Ding, Q. Li, Q. Yan, *CrystEngComm* **2017**, *19*, 901.

[287] S. Rühle, *Sol. Energy* **2016**, *130*, 139.

[288] J. Pascual, G. Nasti, M. H. Aldamasy, J. A. Smith, M. Flatken, N. Phung, D. Di Girolamo, S.-H. Turren-Cruz, M. Li, A. Dallmann, R. Avolio, A. Abate, *Mater. Adv.* **2020**, *1*, 1066.

[289] M. I. Saidaminov, I. Spanopoulos, J. Abed, W. Ke, J. Wicks, M. G. Kanatzidis, E. H. Sargent, *ACS Energy Lett.* **2020**, *5*, 1153.

[290] M. T. Hoang, F. Ünlü, W. N. Martens, J. M. Bell, S. Mathur, H. Wang, *Green Chem.* **2021**.

[291] B. Wilk, S. Öz, E. Radicchi, F. Ünlü, T. Ahmad, A. P. Herman, F. Nunzi, S. Mathur, R. Kudrawiec, K. Wojciechowski, *ACS Sustain. Chem. Eng.* **2021**, *9*, 3920.

[292] Q. Tao, P. Xu, M. Li, W. Lu, *npj Comput. Mater.* **2021**, *7*, 23.

[293] J. Im, S. Lee, T.-W. Ko, H. W. Kim, Y. Hyon, H. Chang, *npj Comput. Mater.* **2019**, *5*, 37.

[294] N. T. P. Hartono, J. Thapa, A. Tiihonen, F. Oviedo, C. Batali, J. J. Yoo, Z. Liu, R. Li, D. F. Marrón, M. G. Bawendi, T. Buonassisi, S. Sun, *Nat. Commun.* **2020**, *11*, 4172.

[295] L. Zhang, M. He, S. Shao, *Nano Energy* **2020**, *78*, 105380.

[296] B. Yılmaz, R. Yıldırım, *Nano Energy* **2021**, *80*, 105546.